DECEMBER 1957 VOLUME 1 (1957) No. 6

GREGG M. SINCLAIR LIBRARY
UNIVERSITY OF HAWAII
8-6-63

NUCLEAR INSTRUMENTS

A JOURNAL ON ACCELERATORS, INSTRUMENTATION AND TECHNIQUES IN NUCLEAR PHYSICS

EDITOR K. SIEGBAHN – UPPSALA

CONTENTS

K. O. NIELSEN, The development of magnetic ion sources for an electromagnetic isotope separator . . . 289
O. ALMÉN and K. O. NIELSEN, Systematic investigation of a magnetic ion source for an electromagnetic isotope separator . . . 302
B. S. JENSEN, Note on the preparation of anhydrous rare-earth chlorides for the electromagnetic isotope separator . . . 323
D. JAMNIK, Energy control of a 31 MeV betatron . . . 324
K. V. VLADIMIRSKY, Radiation instability in nuclear magnetic resonance experiments . . . 329
D. H. WHITE and G. W. HUTCHINSON, A fast coincidence circuit . . . 331
R. L. MACKLIN, Graphite sphere neutron detector . . . 335
G. HORLITZ und W. PAUL, Die Blasendichte in einer Blasenkammer unter verschiedenen Betriebsbedingungen . . . 340
K. J. LE COUTEUR, The vertical motion of particles through the regenerative beam extractor of a synchrocyclotron . . . 343
N. E. BOOTH and B. LEDLEY, Efficient detector for high energy neutrons . . . 345
H. B. VAN DER RAAY, Focussing of the synchroton scattered-out beam . . . 351
P. R. ORMAN, A printed distributed amplifier . . . 354
Author Index . . . 359
Subject Index . . . 361

NORTH-HOLLAND PUBLISHING COMPANY – AMSTERDAM

NUCLEAR INSTRUMENTS

A journal on accelerators, instrumentation and techniques in nuclear physics

EDITOR: K. SIEGBAHN, UPPSALA

EDITORIAL BOARD:

J. B. ADAMS (CERN)
E. AMALDI (Rome)
H. L. ANDERSON (Chicago)
K. T. BAINBRIDGE (Cambridge, Mass.)
C. J. BAKKER (CERN)
P. R. BELL (Oak Ridge)
R. E. BELL (Montreal)
A. BERTHELOT (Saclay)
H. BRINKMAN (Groningen)
S. DE BENEDETTI (Pittsburgh)
M. DE HEMPTINNE (Louvain)
A. DE-SHALIT (Rehovoth)
M. DEUTSCH (Cambridge, Mass.)
S. DU TOIT (Pretoria)
B. S. DŽELEPOV (Leningrad)
W. GENTNER (CERN)
P. C. GUGELOT (Amsterdam)
H. HALBAN (Paris)
O. HAXEL (Heidelberg)
P. HUBER (Basel)
D. J. HUGHES (Brookhaven)
S. KIKUCHI (Tokyo)
J. KOCH (Copenhagen)
M. S. KOZODAEV (Moscow)
S. LIVINGSTON (Cambridge, Mass.)
E. M. MCMILLAN (Berkeley)
M. G. MEŠČERJAKOV (Moscow)
P. B. MOON (Birmingham)
M. L. OLIPHANT (Canberra)
W. PAUL (Bonn)
A. S. RAO (Bombay)
G. SALVINI (Rome)
P. SAVIĆ (Belgrade)
P. SCHERRER (Zürich)
CH. SCHMELZER (CERN)
H. W. B. SKINNER (Liverpool)
R. TANGEN (Blindern)
V. I. VEKSLER (Moscow)
O. WERNHOLM (Stockholm)
D. TAYLOR (Harwell)
G. VON DARDEL (CERN)
R. R. WILSON (Cornell)
S. D. WINTER (Saclay)

Contributions may be sent to the Editor, Professor K. Siegbahn, Institute of Physics, the University of Uppsala, either directly or through the intermediary of one of the members of the Editorial Board of the country or region in which the author is working. Contributions may be written in English, French or German, with an abstract in English.

Books for review should be sent to Professor Siegbahn.

Nuclear Instruments is published in bi-monthly issues. The subscription price of a volume of 360 pages is $ 17.00 (130 s), postage free.

Subscriptions should be sent to the publishers, North-Holland Publishing Company, P.O.Box 103, Amsterdam or to any subscription-agent. Subscriptions for U.S.A. are to be sent exclusively to Interscience Publishers, Inc., 250 Fifth Avenue, New York, 1 N.Y.

No part of this issue may be reproduced in any form, by print, photoprint, microfilm or any other means without written permission from the publisher. Reprints, photoprints or microfilms are obtainable at cost from the publisher.

PHILIPS *equipment for*
Nuclear Physics and Atomic Energy

Shown here is a 4-stage cascade accelerator, which supplies a heavy particle beam of 1 mA at a voltage of over 700 kV. Similar units can be supplied for other energy ranges. Accessory equipment such as electronic stabilizers keeping the accelerating voltage constant within 1:1000, beam deflecting magnets, etc. are available if required.

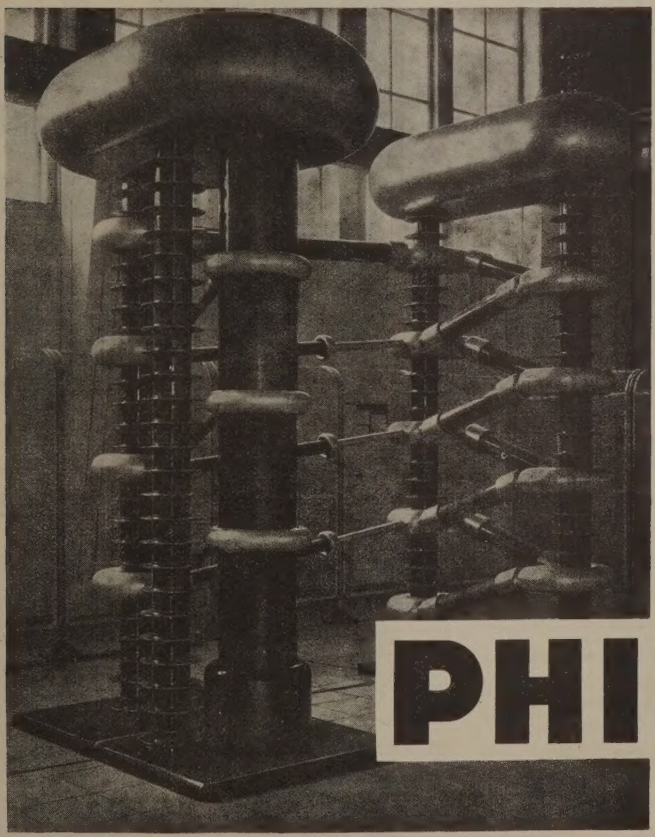

4-stage compact cascade accelerator installed at the Physikalisch Technische Bundesanstalt in Brunswick, Germany.
(Photo by courtesy of P.T.B., Brunswick).

- Synchro-cyclotrons for various final energies.
- Linear electron accelerators.
- Cockcroft-Walton accelerators.
- Radiation measuring equipment.
- Area monitoring instrumentation.
- Civil defence instruments.
- Reactor control instrumentation.
- Geiger counter tubes.
- Radio-active isotopes.
- Air liquefiers.
- Generators for very high d.c. voltages.

PHILIPS

Nuclear Equipment

For further information please apply to one of the following addresses:

N.V. PHILIPS' GLOEILAMPENFABRIEKEN,
Scientific Equipment Department, Eindhoven - Holland

PHILIPS ELECTRICAL LTD.,
Research and Control Instruments Division, Shaftesbury Avenue, London W. C. 2

PHILIPS ELECTRONICS INC.,
Instruments Division, 750, South Fulton Avenue, Mount Vernon N.Y. U.S.A.

PHILIPS

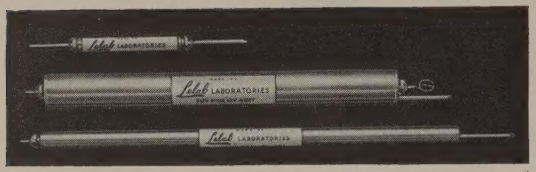

LELAB METAL-WALLED G-M TUBES

for anti-coincidence applications where uniformity counts !

Lelab Counter Tubes are individually constructed, filled, and tested. Each is fabricated almost entirely of metal. All components are confined within the diameter of the tube shell to permit close stacking.

Compare our low prices on these superior tubes!

(Makers of Lelab [Robinson-Selverstone Type] Probe Counters for neurosurgery and where a fine needle-like probe for highly localized measurements is useful.)

Write for complete information

H. W. Leighton Laboratories

York & Sunset Lane-Hatboro, Pa. U.S.A.

RADIATION INSTRUMENT CO.

MODEL 412 MERCURY RELAY

Precision Sliding Pulser

for Precise Calibration of Single & Multi-Channel Pulse Height Analyzers

Determines Window Widths Using Principle of *Constant Angular Velocity* } **AUTOMATICALLY 10 × more accurately 40 × faster than conventional pulsers**

Incorporates Both Manual Control and Precision Motor Drive

Simulates Pulses from Scintillation, Proportional, or Geiger Counters

RISE TIME—Less than .003 microsec.

DECAY TIME CONSTANT—1, 10, 100, 350, microsec. (selector switch).

PULSE AMPLITUDE—Continuously variable from 0 to maximum. Ranges 2, 3, 10, 30, 100, 1000 mV. Provision for direct connection of external battery for larger pulses.

POLARITY—Polarity switch permits selection of positive or negative pulses.

CALIBRATION—Self contained standard cell and null indicating balance circuit for precision adjustment.

LINEARITY—0.1% 10 turn Helical potentiometer with 5" dial.

SCAN SPEED—2 RPM standard (1, 3, 5, 6 and 10 rpm also available.)

PRICE $ 450.00 f.o.b. SILVER SPRING, Md., U.S.A.

RADIATION INSTRUMENT CO.

P. O. BOX 733 SILVER SPRING, MARYLAND, U.S.A.

NCA

WORLDWIDE

Film Badge Service

for Beta Gamma X-rays and Neutrons

Available in clip-on, wrist, or ring style, for isotope and X-ray laboratories, medical and dental offices, and industrial plants. Write or 'phone for Bulletin N20, containing complete information and prices.

- **Low Cost**
- **Prompt, Reliable Reports**
- **Provides Permanent Records**
- **Covers Wide Range of Energies and Exposures**
- **5 Filters for Highest Accuracy**

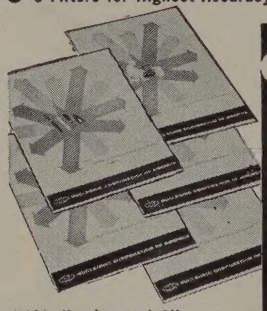

#101. Uranium and Oil Exploration Equipment
#102. Atomic Education Equip't.
#103. Nuclear Laboratory Equip't.
#104. Medical Radioisotope Equipment
#105. Geiger, Proportional, and Scintillation Detectors

NCA

Your One Source of Nucleonic Equipment for Every Field

Send now for above new catalogs

Dept. N17

NUCLEONIC

Corporation of America

196 Degraw St B'klyn 31, N. Y.
MAin 4-7370

NCA

NUCLEAR INSTRUMENTS 1 (1957) 289–301; NORTH-HOLLAND PUBLISHING CO. – AMSTERDAM

THE DEVELOPMENT OF MAGNETIC ION SOURCES FOR AN ELECTROMAGNETIC ISOTOPE SEPARATOR

K. O. NIELSEN

Institute for Theoretical Physics, University of Copenhagen, Denmark

Received 10 July 1957

The present paper gives a survey of several ion sources of the magnetic type, which have been used in connection with the electromagnetic isotope separator in Copenhagen. The first types constructed for handling gases are described briefly, while ion sources for solids are discussed in greater detail. The temperature of the discharge chamber can be raised to about 1100° C. The evaporation rate is controlled by the temperature of the sublimation furnace. Problems in connection with the maintenance of optimal pressure in the discharge chamber by adjusting the furnace temperature are discussed.

1. Introduction

The electromagnetic isotope separator at the Institute for Theoretical Physics, Copenhagen, was originally provided with a low voltage capillary arc source[1,2]). During recent years, several ion sources of the magnetic type have been used with satisfactory result both for gases and solids. The isotope separator is a 90° sector type, which provides the possibility of choosing an ion source with either end or side extraction†. In Copenhagen, work has been concentrated on ion sources with end extraction. It is important that separated samples in the mass region 150 to 190 can be obtained because of the great interest in the nuclear properties of this region. The problem of building ion sources suitable for handling the rare earths was our main task, in view of the fact that they lie in this mass region.

2. Ion Source I

The first magnetic ion source built in Copenhagen was constructed for the separation of gases or volatile liquids having vapour pressures above 0.1 mm Hg at room temperature. Fig. 1 shows this magnetic ion source which is of the same type as that used by the isotope separator group in Stockholm[3,4]). It consists of a brass anode block (1) with a magnet coil (3) wound on a copper water cooling tube (2). The filament (4) is attached to two copper rods (5) which are mounted on water cooled brass tubes (6). The needle valve for controlling the gas inlet is connected to the tube (9). The ion source is provided with a vacuum lock (8) so that the filament can be replaced without breaking the main vacuum. The filament is made of a 0.4 mm tungsten wire and has a lifetime of 50 to 100 hours. The bottom plate (10) of the discharge chamber is made of stainless steel and can easily be replaced in order to change the outlet opening. The filament has a negative potential relative to the anode.

† End extraction means extraction in the direction of the ion source magnetic field; side extraction means extraction perpendicular to the magnetic field.

[1]) J. Koch and B. Bendt-Nielsen, Mat. Fys. Medd. Dan. Vid. Selsk., **21** (1944) no. 8.

[2]) J. Koch, Circ.US.Nat. Bur. Stand. no. 522 (Washington, 1953) p. 165.

[3]) I. Bergström, S. Thulin, N. Svartholm, and K. Siegbahn, Ark. Fys. **1** (1950) no. 11.

[4]) P. C. Veenstra and I. M. W. Milatz, Physica **16** (1950) 528.

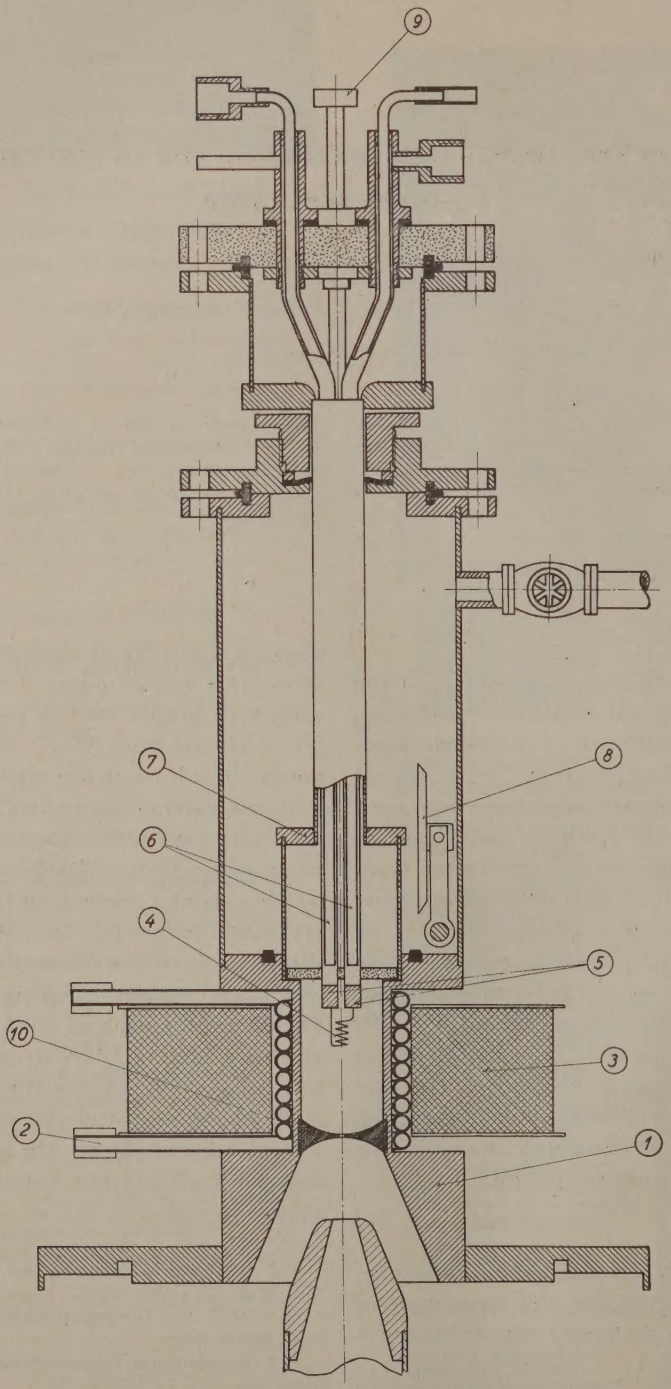

Fig. 1. Magnetic ion source I for gases.

Typical operating data are:

Anode voltage:	100–200 V.
Arc current:	1–2 A.
Magnetic field:	0–400 gauss.
Diameter of outlet opening:	2–5 mm.
Beam current for krypton:	50–150 μA.

The ion source was found to be useful for inert gases[5]). An efficiency of the order of 5 % is obtained for krypton. Besides inert gases the ion source I has also been used for preparing P^{33} sources for beta ray investigations[6]). The gaseous compound PH_3 was used as charge material.

3. Ion Source II†

This ion source is of the Finkelstein type[7]) similar to that investigated by the group in Amsterdam[8,9]). Here the electrons oscillate in the magnetic field until they reach the anode, which results in a much lower anode current than for ion source I. This gives a considerable increase in the filament lifetime. Therefore ion source II was not provided with a vacuum lock for replacing the filament.

4. Ion Source III

In principle ion sources I and II can be used for solids[3]), but because of condensation on the watercooled walls and filament supports, the efficiency will be very low (of the order of 0.01 % to 0.1 %).

To get a reasonable efficiency for solids it is necessary that all parts of the discharge chamber have a temperature so high that loss due to condensation is avoided.

A preliminary magnetic ion source with oscillating electrons and with end extraction was constructed. The discharge chamber was built as a closed container and placed, thermally insulated, in the magnetic field. Efforts have been made to keep the discharge chamber vapour-tight so that the escape of neutral molecules or atoms is confined to the outlet. The electron supplying filament was mounted inside the chamber so that the filament heating power is also utilized for heating of the whole discharge chamber. The solid charge material is evaporated from a furnace into the discharge chamber.

The preliminary ion source was used for a systematic investigation of the extracted ion beam of the plasma discharge[10]).††

Using the results of this systematic investigation a final ion source has been constructed, see fig. 2. It consists of five main parts, viz. a stainless steel casing, an upper part with six kovar-glass seals, each capable of carrying a current of 100 amperes, a vacuum lock, a discharge chamber, and a sublimation furnace. The discharge chamber and furnace are constructed as separate units and may easily be replaced by other types. The dimensions of the casing are so that a chamber of maximum 120 mm length can be inserted. It is important that the chamber be as long as possible in order to obtain high efficiency (cf. AN section 6). The magnet coil is wound on a water cooled copper lining surrounding the narrow cylindrical part of the casing. The magnetic filed can be varied from zero to 1000 gauss.

For charging, the furnace can be removed through a valve without breaking the main vacuum (see fig. 2). This arrangement allows us to start separation a few minutes after loading the furnace, which is very important when separating short lived radioactive materials.

4.1. DISCHARGE CHAMBER IIIA, FOR MEDIUM HIGH TEMPERATURE

The discharge chamber is shown in fig. 3 and consists of one plate at the bottom (1) and one at the top (2), both of stainless steel, acting as cathodes, and a cylindrical anode (3) which is a lining of molybdenum fitted into a tube (9) of

† This ion source was constructed by Mr. B. Elbek.

†† O. Almén and K. O. Nielsen (1957). In the following to be referred to as AN, its sections and equations as (AN, section 3,2), (AN, eq (16)).

[5]) O. Kofoed-Hansen and K. O. Nielsen, Mat. Fys. Medd. Dan. Vid. Selsk. **26** (1951) no. 7.

[6]) B. Elbek, K. O. Nielsen and O. B. Nielsen, Phys. Rev. **95** (1954) 96.

[7]) A. T. Finkelstein, Rev. Sc. Instr. **11** (1940) 94.

[8]) I. Kistemaker and H. L. Douwes Dekker, Physica **16** (1950) 198.

[9]) I. Kistemaker and H. L. Douwes Dekker, Physica **16** (1950) 209.

[10]) O. Almén and K. O. Nielsen, Nuclear Instruments **1** (1957) 302.

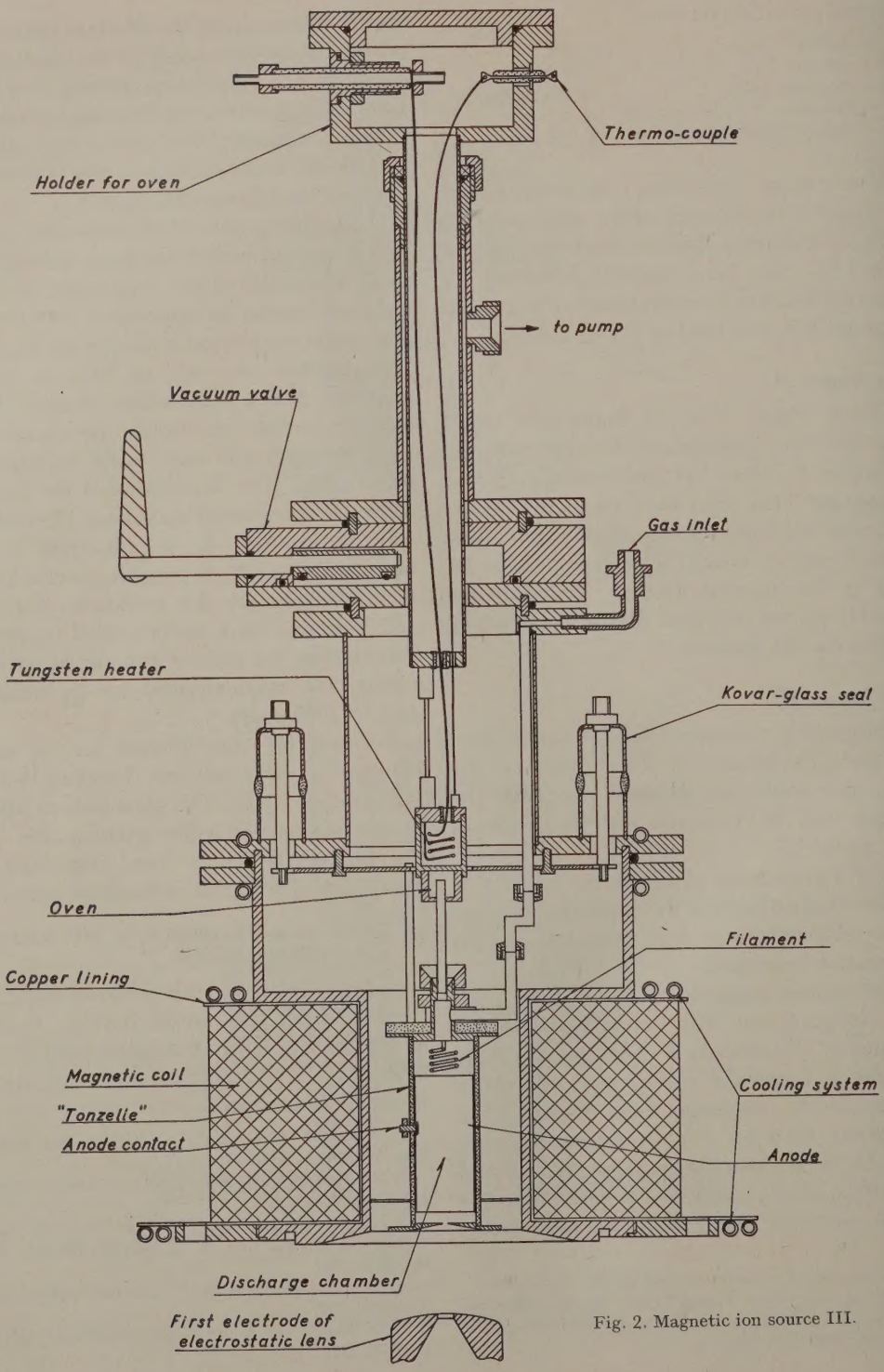

Fig. 2. Magnetic ion source III.

ceramic material placed between the two plates. The discharge chamber itself is held together by two rods of stainless steel (4), and the whole unit is fastened by screws to a thin plate of the same material (see fig. 2). On the two rods just above the bottom plate is mounted a ring of stainless steel (11) which, for centering, is provided with three points at the periphery.

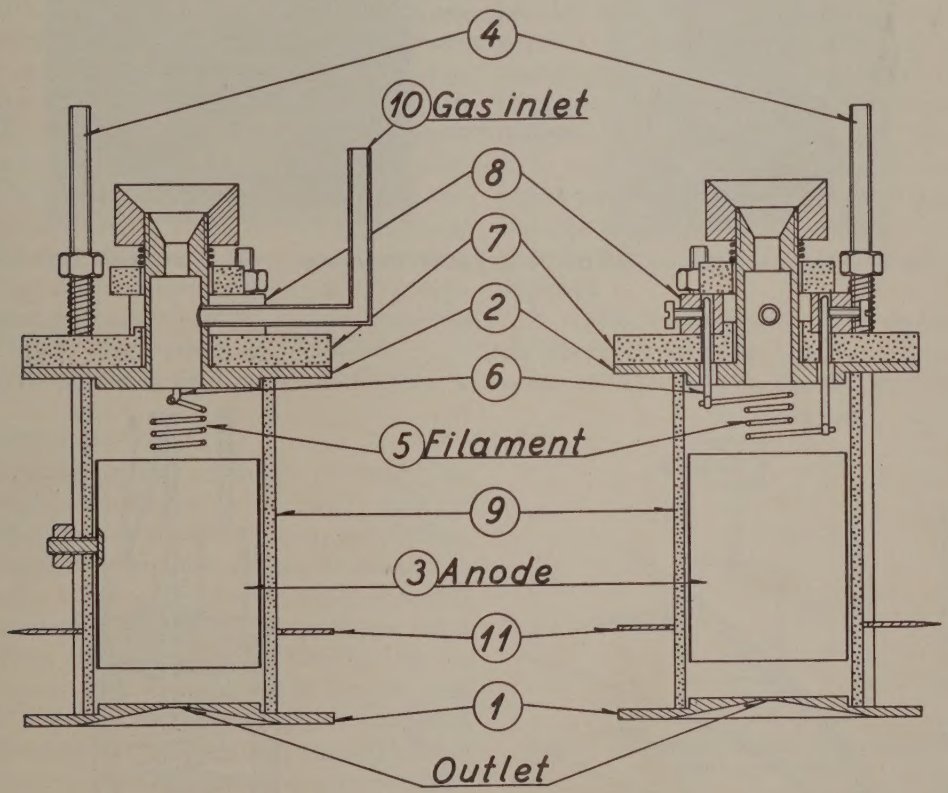

Fig. 3. Discharge chamber IIIa for medium high temperature.

Radiation shields can be inserted between the discharge chamber and the surrounding wall. The tungsten filament is clamped to two short pins (6) of 1.2 mm melybdenum, leading through an insulator of pyrophyllite (7) and joined to two blocks of stainless steel (8). By using molybdenum pins as an interlink, difficulties arising from heating a filament screwed directly to stainless steel are avoided.

To avoid modulations of the intensity of the ion beam the filament is fed by DC-current with a ripple less than 0.2%. The negative pole of the filament is connected to the bottom and top plates (1) and (2), so that the centre of the filament is at a potential of about 5 volts higher than (1) and (2). Thus, only a small fraction of the emitted electrons has sufficient energy to reach these plates.

Even a small ripple in the magnetic field causes intensity modulation in the ion beam, and therefore the current to the coil must be smoothed very carefully. The resulting ripple is less than 0.2%. The ion source supplies will be described later[11]).

Gases are let in through a long and thin-walled tube of stainless steel (10) which is connected to the hottest part of the discharge chamber,

[11]) K. O. Nielsen and O. Skilbreid, to be published (1957).

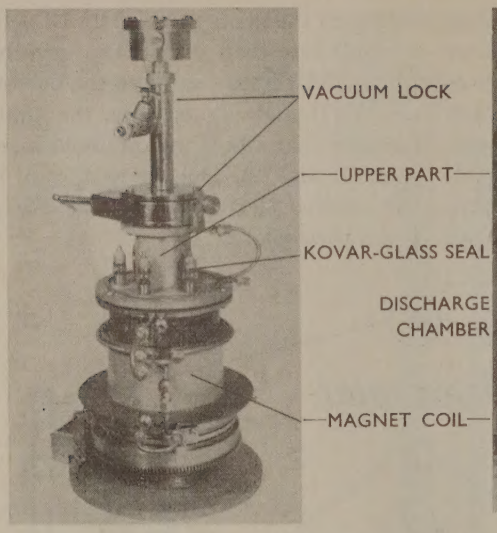

Fig. 4a. Photograph of the ion source III.

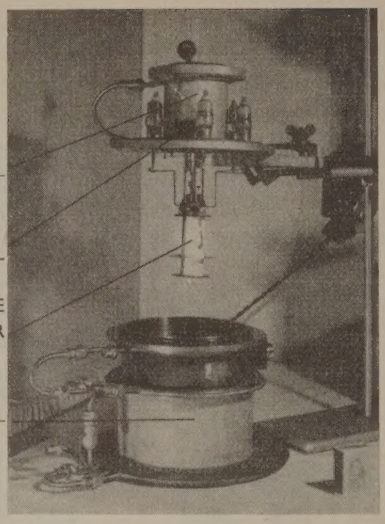

Fig. 4b. Photograph of the ion source III disassembled.

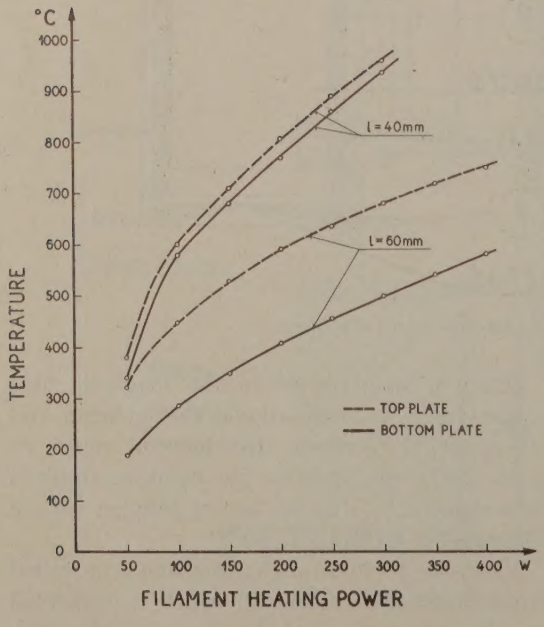

Fig. 5. Temperature of the top and bottom plate as a function of the filament heating power.

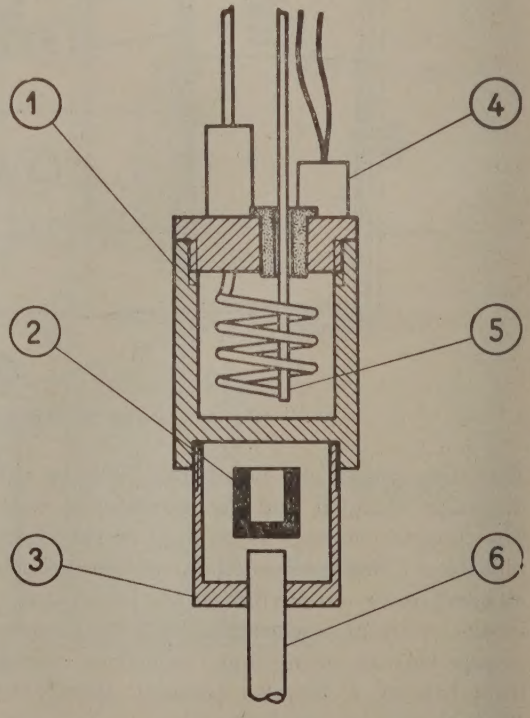

Fig. 6. Sublimation furnace with heater inside. Parts (1), (3), and (6) are made of stainless steel.

i.e. close to the filament. In this way the loss of heat through the tube will not result in any cold regions.

The maximum power available for heating the filament is 600 W. Fig. 5 gives the temperatures at the top and bottom plate as functions of the filament heating power. The temperature measurements are shown for two discharge chambers, one with a length $l = 40$ mm and one with $l = 60$ mm. No radiation shields are placed around the discharge chambers.

As already mentioned, a long discharge chamber is necessary in order to obtain high efficiency, cf. AN, fig. 19. On the other hand, fig. 5 shows that the maximum obtainable temperature decreases very quickly with the length and therefore we try to choose an optimal length for the chamber in any actual separation. As it appears from the curves in fig. 5 this type of discharge chamber can be used for materials that require temperatures up to 700° C.

Typical operating data are given in ref. [10]).

Sublimation Furnace

In connection with discharge chamber IIIa a stainless steel furnace is normally used. A typical furnace is shown in fig. 6; size, shape, and length of the tube (6) can be varied to cover the actual need. The furnace is mounted by means of two 1.25 mm molybdenum wires to a brass cylinder which fits into the seal in the vacuum lock (see fig. 2). The furnace consists of two parts; in the upper part (1) is placed a tungsten heater (5), and the lower part (3) can be unscrewed for filling with charge material. This material can either be placed directly in (3) or in a small crucible (2). By using the small crucible, the charge material can be transferred into the furnace in a quick and easy way; this method is therefore normally used with radioactive charge material produced in a reactor, and the crucible is also used as container during irradiation in the reactor. Because of neutron capture, the crucible (2) is made either of aluminum, boronfree glass, or graphite.

Heat radiation shields can be placed around the sublimation furnace, but are usually not used because sufficient heat loss must be present to obtain a time constant short enough to secure good temperature regulation.

A thermocouple (4) is clamped to the lid of the upper part (1). As a rule, the temperature is here a little higher than that of the charge material.

In order to secure stable operating conditions the pressure p_d in the discharge chamber must be slightly higher than the threshold pressure p_{min}, (cf. AN, section 6). The threshold pressure p_{min} depends on the ionization cross section, the operating conditions, and the geometry of the chambers; for a chamber of this type it lies between 10^{-4} and 10^{-3} mm Hg. Since, for $p_d > p_{min}$ (cf. AN, fig. 8), the beam current I_i is independent of the pressure, it is imperative that the vapour pressure p_d be kept constant as near above p_{min} as possible if highest efficiency is required.

A schematic drawing of the furnace and chamber is shown in fig. 7. p_f, p_d, and p are the pressures in the furnace, the discharge chamber,

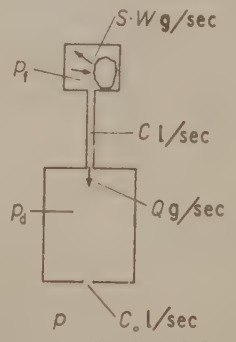

Fig. 7. A schematic drawing of the furnace and discharge chamber.

and the acceleration chamber, respectively. C is the conductance of the tube between furnace and chamber, and C_0 is the conductance of the outlet opening. Making the approximations that $p_f \gg p_d$ and $p_d \gg p$, we get for the rate of flow Q:

$$Q = p_f \cdot C = p_d \cdot C_o \, \mu \cdot \text{l/sec} \qquad \text{(1a)}$$

or

$$Q = 5{\cdot}87 \times 10^{-8} \cdot M \cdot p_f \cdot C \text{ g/sec} + , \qquad \text{(1b)}$$

where p is in microns, C in liters per sec, and M is the molecular mass in grams. From eq. (1) we see that the requirement that p_d = constant during a separation is equivalent to the requirement Q = constant.

The tube (6) in fig. 6 can easily be replaced and from eq. (1) it follows that the required p_f is inversely proportional to the conductance C of this tube.

The rate of evaporation W g·cm^{-2}·sec^{-1} is given by the expression[12])

$$W = D - 0.5 \log T - \frac{A}{T} \text{ g·cm}^{-2}\text{·sec}^{-1}, \qquad (2)$$

where A and D are constants (see ref. [12]), chapter 11, tables 1 and 2).

For a discussion of the operating conditions of the furnace we consider the two cases, $Q \ll S \cdot W$ and $Q \approx S \cdot W$, where S is the surface area of the charge material.

1) $Q \ll S \cdot W$ g·sec^{-1}

In this case we can calculate the furnace pressure p_f as the equilibrium pressure given by the Clausius-Clapeyron equation

$$\log p_f = -\frac{A}{T} + B ,$$

where A and B are constant[12,13]). The dotted curve in fig. 8 shows schematically the general dependence of p_f on T. The three solid curves give the corresponding rate of flow $Q = C\, p_f$ for different values of C; $C_1 > C_2 > C_3$.

From eq. (3) we find

$$\frac{dQ}{Q} - \frac{dp_f}{p_f} = \text{constant} \cdot \frac{1}{T^2} dT , \qquad (4)$$

A tube with a small conductance C requires a relatively higher temperature in order to keep Q unaltered (see fig. 7). On the other hand, we see from eq. (4) that the demand for constant temperature is smaller at the higher T. In addition, the time constant for temperature variations is smaller at higher temperatures, which also makes the temperature regulation easier.

2) $Q \approx S \cdot W$ g·sec^{-1}

Here the evaporation rate $S \cdot W$ g·sec^{-1} through the surface of the charge limits the rate of flow Q, and this limit varies markedly with the quantity and the physical state of the charge as well as with the temperature. This means that variation in temperature is needed in order to maintain optimum flow, while the temperature in the previous case should be kept constant. The dot and dash curves in fig. 8 give

[12]) S. Dushman, Scientific Foundations of Vacuum Technique (1949).

[13]) R. L. Loftness, Vapor Pressure Chart for Metals, U.S.A.E.C., N.A.A. SR. 132 (1952).

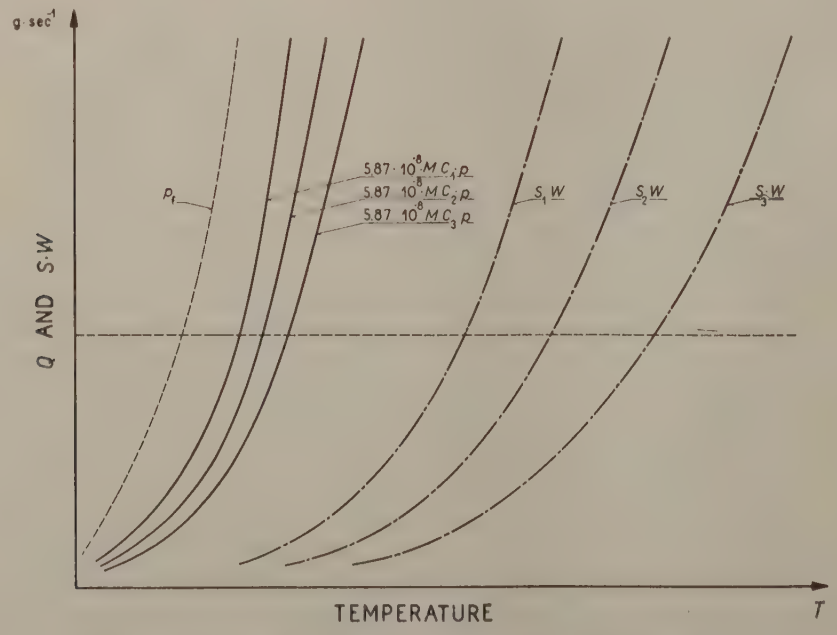

Fig. 8. The rate of flow and the rate of evaporation as functions of the temperature.

$S \cdot W$ g·sec^{-1} as functions of the temperature for three values of S; $S_1 > S_2 > S_3$ (see eq. (2)).

The following experiences confirm the above relationships:

(1) The most stable operation conditions are always obtained with a long and narrow tube between furnace and chamber. However, too small a value of the conductance C can cause difficulties because of the high furnace temperature required.

(2) The required furnace temperature is constant when large amounts of charge material are used and repeated runs with the same C give reproducible values for the temperature. When the separation is almost finished, the amount of charge material is small and the condition $Q \ll S \cdot W$ is no more valid. Since S decrease it is necessary to increase the temperature in order to keep Q constant (see fig. 8).

(3) It is always difficult to find stable operating conditions when the amount of charge material is small. Here Q depends on S, and the needed temperatures vary from one separation to the other. Thus antimony always gave bad results for an amount of charge material smaller than 5 mg but good and reproducible conditions when the amount exceeded 10 mg[14]).

When the furnace temperature necessary for a certain material is lower than about 200° C it can be difficult to regulate the temperature well enough, see eq. (4). In this case, it can be of advantage to use a furnace of the type shown in fig. 9. Here the tungsten heater is mounted fixed around the furnace, which enables us to make the furnace much smaller than that shown in fig. 6. This gives a much smaller time constant for temperature variations, which again makes the temperature regulation faster and easier. No radiation shields should be placed around the tungsten heater when the smallest possible time constant is wanted.

Charge Material

The discharge chamber IIIa with stainless steel furnace of the type shown in figs. 6 and 9 is suitable for substances for which the vapour pressure is of the order 10^{-3} mm Hg at a temperature below 700° C. Table 1 gives, for a series of substances, the charging material and the approximate furnace temperature. Similar lists are given by Keim[15]) and by Dawton and Smith[16]).

TABLE 1.

CHARGE MATERIAL AND FURNACE TEMPERATURE FOR DISCHARGE CHAMBER IIIA

Collected Isotopes	Charge Material	Furnace Temperature	Ref.
Be^9	$BeCl_2$	ca. 200°	
Mg^{24}, Mg^{25}, Mg^{26}	Mg	450°	[17])
Sb^{115}–Sb^{120}	Sb	550°	[14])
Sn	Sn	600°†	
Re^{186}, Re^{187}, Re^{188}	Re_2O_7	170°	[18])
W	WCl_6††	70°	
Os	OsO_4	External	
Hg^{203}†††	HgO		
Pb	Pb	600°	[19])
Bi	Bi	450°	[19])

† At this temperature the vapour pressure of Sn is so low that a supporting inert gas must be added.

†† The charge material WCl_6 was kindly supplied by A. E. R. E. Harwell.

††† The separation of Hg was carried out by O. Almén, on leave from Chalmers University of Technology.

TABLE 2.

OBSERVED MASS LINES. DISCHARGE CHAMBER IIIA WITH CHLORIDES AS CHARGE MATERIAL AT A TEMPERATURE ABOUT 800° C.

Mass Number	"Ionic Form"	Mass Number	"Ionic Form"
52	$(Cr^{52})^+$	91	$(Fe^{56}\,Cl^{35})^+$
53	$(Cr^{53})^+$	92	$(Mn^{55}\,Cl^{37})^+$
55	$(Mn^{55})^+$	93	$(Fe^{56}\,Cl^{37})^+$
56	$(Fe^{56})^+$	125	$(Mn^{55}\,Cl_2{}^{35})^+$
87	$(Cr^{52}\,Cl^{35})^+$	126	$(Fe^{56}\,Cl_2{}^{35})^+$
88	$(Cr^{53}\,Cl^{35})^+$	127	$(Mn^{55}\,Cl^{35}\,Cl^{37})^+$
89	$(Cr^{52}\,Cl^{37})^+$	128	$(Fe^{56}\,Cl^{35}\,Cl^{37})^+$
90	$(Mn^{55}\,Cl^{35})^+$	129	$(Mn^{55}\,Cl_2{}^{23})^+$
		130	$(Fe^{56}\,Cl_2{}^{37})^+$

[14]) B. Skytte Jensen, K. O. Nielsen, O. B. Nielsen, and R. Sheline, to be published.

[15]) C. P. Keim, I. Appl. Phys. **24** (1953) 1255.

[16]) R. H. V. M. Dawton and M. L. Smith, Quarterly Reviews, Vol. IX, (1955) no. 1.

[17]) B. Elbek, B. S. Madsen, and O. Nathan, Phil. Mag. **46** (1955) 663.

[18]) K. O. Nielsen and O. B. Nielsen, to be published (1957) in Nuclear Phys. in press.

[19]) K. O. Nielsen, O. B. Nielsen, and M. A. Waggoner, Nuclear Physics **2** (1956) 476.

Because of the excessive chemical corrosion of stainless steel it was impossible to use discharge chamber IIIa for chloride compounds for which the needed temperature is higher than 300° C,

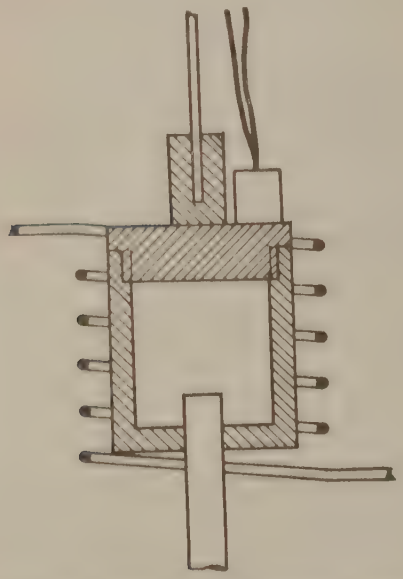

Fig. 9. Sublimation furnace with heater outside.

see table 2. The ions listed in this table are consistent with the observed mass numbers and presumably represent the main ionic term present in the beam.

External Furnace

The discharge chamber IIIa has also been used for a single preliminary run with Os. Here a small amount (a fraction of a gram) of OsO_4 was placed in an external furnace† made of glass and heated to a temperature about 50° C. The rate of vapour flow was controlled by a needle valve.

An external sublimation furnace can be used for liquids and solids having vapour pressures of approximately 10^{-1} mm Hg or more at 100° C, compare A. H. Barnes *et al* [20]).

Inert Gases

Also for handling gases, discharge chamber IIIa is superior to ion sources I and II in some respects. Thus the isotope separator has been used for preparing Kr^{85} samples for optical hyperfine structure investigations[21,22]). Krypton extracted from fission products was used, and as the beam current of Kr^{85} is relatively weak, it is important to reduce the formation of $(Kr^{84}H)^+$. Before sufficient degasing, all ion sources gave a beam current $(Kr^{84}H)^+$ of the order of 10% of $(Kr^{84})^+$ current. After about 15 min. this ratio dropped to less than 0.5% for discharge chamber IIIa, while the same reduction took much longer time for ion sources I and II. The reason is presumably that all parts in chamber IIIa reach a high temperature while I and II have watercooled walls.

4.2. DISCHARGE CHAMBER IIIb

For the handling of chlorides which require a temperature above 300°C, discharge chamber IIIb was built, see fig. 10. Only graphite and pyrophyllite are used on the inside of this chamber. The chamber is placed into an ion source housing as shown in fig. 2. The sublimation furnace is of a similar construction as that shown in fig. 6. The lower part, in which the charge material is placed, is made of graphite with a tight-fitting lid, see fig. 10.

Two radiation shields are mounted around the discharge chamber and an extra tungsten heater can be mounted between the anode and the inner radiation shield.

The curves in fig. 11 give the temperature of the bottom plate as a function of the heating power. From a comparison with the curves shown in fig. 5 it appears that already one radiation shield increases the temperature considerably (cf. ref. [23]), fig. 2.5). Using two radiation shields, the filament heating power alone can raise the temperature to about 1000° C. In order to obtain a further increase in temperature, it is

† The vapour of OsO_4 is very poisonous and necessary precautions had to be taken.

[20]) A. H. Barnes, S. M. MacNeille, and C. Starr, U.S.A.E.C. TID-5219 (1951).

[21]) E. Rasmussen and V. Middelboe, Z. für Phys., Bd. 141 1955) 160.

[22]) E. Rasmussen and V. Middelboe, Mat. Fys. Medd. Dan. Vid. Selsk. **30** (1955) no. 13.

[23]) R. K. Wakerling and A. Guthrie, U.S.A.E.C. TID-5218.

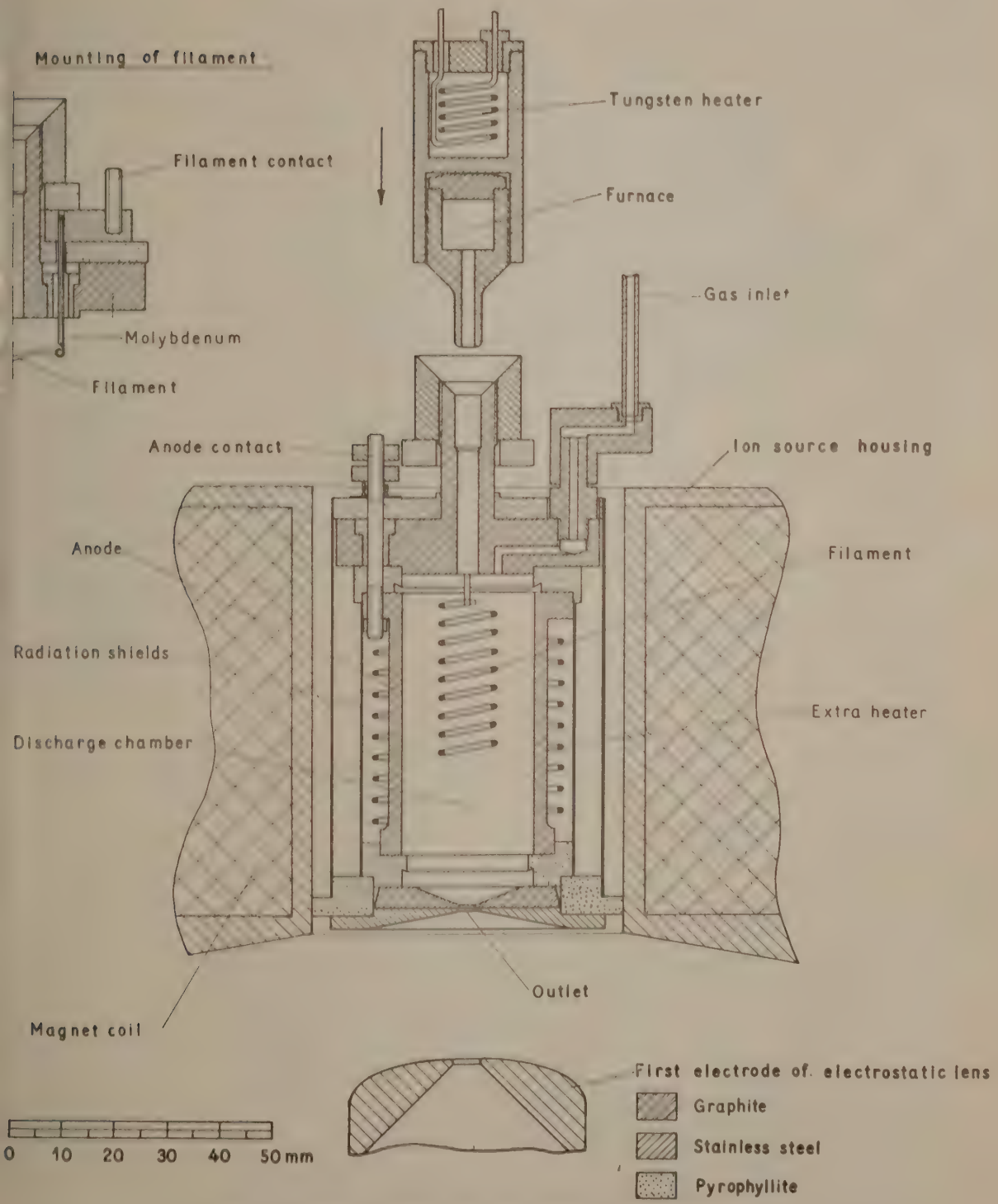

Fig. 10. Discharge chamber IIIb and furnace for high temperature.

necessary to use the extra heater around the anode (see fig. 10).

Since the separation of rare earth isotopes is of special importance, the discharge chamber IIIb was built for handling these elements†. The small amounts of rare earths needed for our isotope separator are now prepared by dissolving the rare earth oxide in hydrochloric acid, evaporating to dryness in an excess of ammonium chloride, and fuming at 600° C††. For the work with short-lived radioactive material it is important that the conversion of oxide to waterfree halides only takes a few minutes by this method.

The vapour pressure for rare earth chlorides as well as for the metals is shown in fig. 12. The full-drawn curve gives the temperature corresponding to a vapour pressure equal to 5×10^{-3} mm Hg; this value is of the same order as the required pressure in the sublimation furnace. The curve is calculated from the Clausius-Clapeyron equation, using tabulated values for the boiling point and the heat of evaporation[24]).

† During the development of this ion source we have used rare earth chlorides as charge material which were kindly supplied by A. E. R. E. Harwell.

†† We are indebted to Mr. B. Skytte Jensen for making these preparations. A detailed description of the procedure is presented by him. (Nuclear Instruments **1** (1957) 323.)

Similar curves for the metals are shown by a dotted line. The curve for $p = 1.5$ mm Hg is due

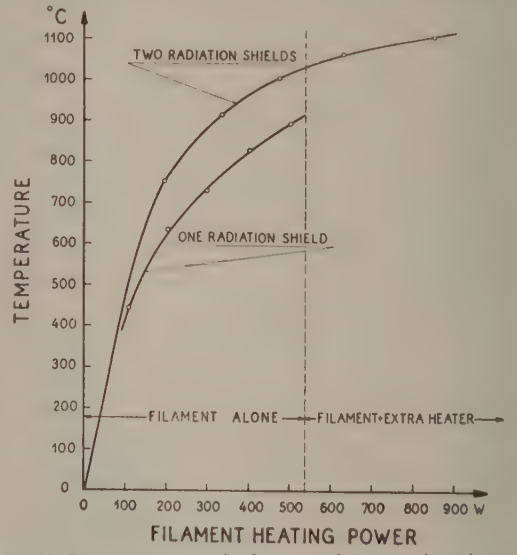

Fig. 11. Temperature at the bottom plate as a function of the heating power.

to privat communication from F. H. Spedding and from his curve we calculate the others by means of Clausius-Clapeyron's equation.

[24]) M. C. Sneed and R. C. Brasted, Comprehensive Inorganic Chemistry IV (1955).

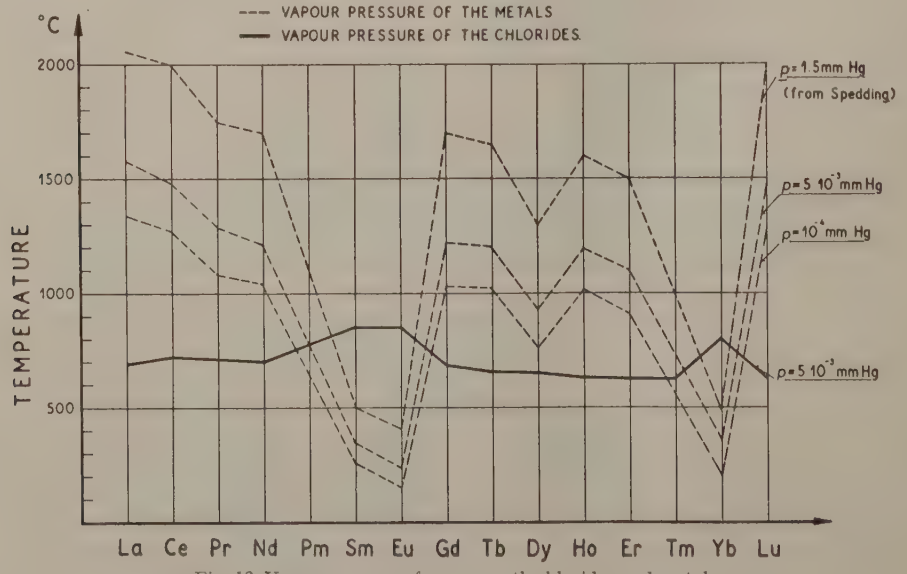

Fig. 12. Vapour pressure for rare earth chlorides and metals.

In the plasma, atomic ions are formed by decomposition and ionization, and many of these are drawn to the top and bottom plates. If the temperature is too low, these ions are lost from the discharge chamber due to condensation and in this way cause a considerable reduction in efficiency. For rhenium such a condensation would be expected and it was indeed found that the efficiency is low (AN par. 6.4). However, in the experiments with cerium and dysprosium we found that, by adjusting the ion source parameters to yield a high anode current (cf. AN fig. 17), normal efficiency could be obtained. A probable explanation may be that the high anode current causes the condensed material to escape again because of sputtering.

At a temperature around 1000° C the beam from chamber IIIb always contains ionic masses 23 and 39, probably Na and K originating from the pyrophyllite insulator.

The discharge chamber IIIb worked satisfactorily with $CeCl_3$, $SmCl_2$, $GdCl_3$[25]), $DyCl_3$[26]), $YbCl_2$[26]), and $LuCl_3$. In all cases the furnace temperature was 750°–900° C (see fig. 12).

4.3. DISCHARGE CHAMBER IIIc

Fig. 13 shows the discharge chamber IIIc, made of graphite and pyrophyllite. The top plate (5) with the filament (6) is similar to the top plate of chamber IIIb, but the bottom plate (2) has the same potential as the anode (1) and therefore the electrons from the filament (6) are not oscillating.

Chamber IIIc gave the same beam current I_i and resolving power RP as chambers IIIa and IIIb, in accordance with the fact that I_i and RP only depend on the plasma boundary at the outlet and on the geometry of the accelerating gap (cf. AN, section 4.2). A systematic investigation of the threshold pressure p_{min}, and with this the efficiency, has not been carried out so far.

The discharge current in chamber IIIc is about 10 times higher than that in chambers IIIa and IIIb and is of the order of 0.5–1 ampères. The filament heating current is correspondingly higher. This results in a shorter filament lifetime; on the other hand, a higher temperature in the discharge chamber is obtained. Furthermore, we can expect a more uniform temperature distribution because the primary electrons strike the bottom plate, which, in the case of oscillating electrons, is the coldest part of the discharge chamber.

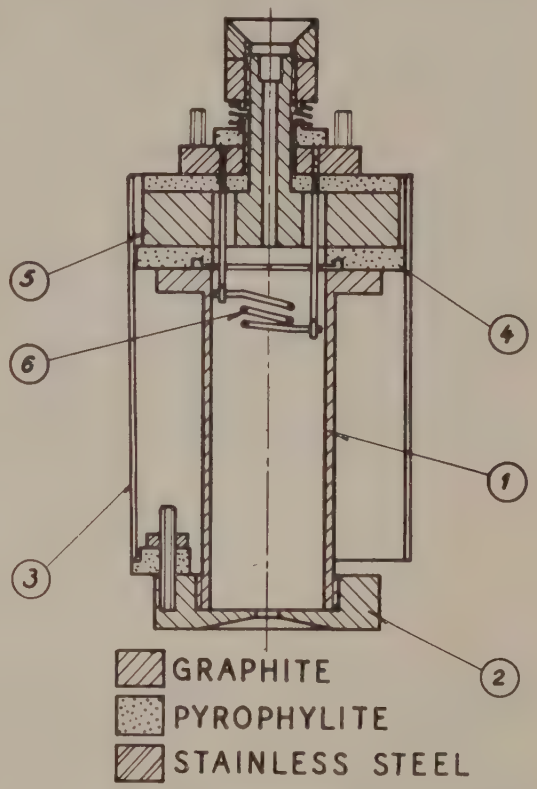

Fig. 13. Discharge chamber IIIc.

Acknowledgements

The author wishes to express his gratitude to the Director of the Institute, Professor Niels Bohr, for his great interest in the experiments and for the excellent working conditions offered at his Institute.

I want to thank Professor J. Koch for discussions and for placing the isotope separator at my disposal. Thanks are also due Mr. O. Skilbreid for very valuable help during the construction of the ion sources in their later stages.

[25]) K. O. Nielsen and O. B. Nielsen, to be published.
[26]) B. Elbek, K. O. Nielsen, and M. Olesen, to be published.

NUCLEAR INSTRUMENTS 1 (1957) 302–322; NORTH-HOLLAND PUBLISHING CO. – AMSTERDAM

SYSTEMATIC INVESTIGATION OF A MAGNETIC ION SOURCE FOR AN ELECTROMAGNETIC ISOTOPE SEPARATOR

O. ALMÉN† and K. O. NIELSEN

Institute for Theoretical Physics, University of Copenhagen

Received 11 June 1957

The properties of a magnetic ion source with oscillating electrons are studied. The ion source is operated in connection with an electromagnetic isotope separator. Special interest is devoted to the obtainable ion currents, the resolving power of the instrument, and the efficiency of the ion source.

The ion current and the resolving power can be varied within wide limits. However, if the ion source is operated at conditions corresponding to maximum resolving power, it is found that the ion current is limited by space charge in the ion extracting device.

By measurements of the parameters of the ion source, performed at maximum resolving power, an investigation of the plasma discharge was possible. It was found that, for maximum resolving power, a constant ion production rate was required, determined only by the extracted ion current.

Applying this result the influence of different factors on the efficiency of the ion source was calculated. The efficiency appeared to be proportional to the length of the discharge chamber and to the ionization cross section. This was also verified experimentally.

CONTENTS

1. Introduction

2. Technical Description of Experimental Arrangements

2.1. ION SOURCE
2.2. LENS SYSTEM
2.3. MAGNET
2.4. COLLECTOR SYSTEM
2.5. VACUUM GAUGES

3. Systematic Investigation of Ion Current and Resolving Power

3.1. I_i AND RP AS FUNCTIONS OF THE ION SOURCE PARAMETERS
3.2. I_i^m AND RP AS FUNCTIONS OF THE ACCELERATION GAP PARAMETERS

4. Plasma Description

4.1. TRANSITION TO THE TOP AND BOTTOM PLATES
4.2. TRANSITION TO THE ION BEAM
4.3. TRANSITION TO THE FILAMENT
4.4. TRANSITION TO THE ANODE

5. Ion Production Rate

5.1. PRELIMINARY DISCUSSION OF THE ION PRODUCTION
5.2. MEASUREMENTS OF THE ION PRODUCTION
5.3. MINIMUM PRESSURE

6. Efficiency

6.1. INFLUENCE OF GEOMETRY ON THE EFFICIENCY
6.2. INFLUENCE OF WORKING CONDITIONS ON THE EFFICIENCY
6.3. EFFICIENCY FOR DIFFERENT GASES
6.4. EFFICIENCY FOR SOLID CHARGING MATERIAL
6.5. EFFICIENCY AT OPERATING CONDITIONS

7. Abnormal Ion Currents

8. Further Experiments

† Department of Physics, Chalmers University of Technology, Gothenburg.

LIST OF SYMBOLS

$A_b A_t$ area of bottom and top plate, respectively.
A_f area of filament.
A_o area of outlet of the ion source.
A_p area of plasma boundary at the outlet.
A_s area equal to $A_b + A_f + A_t$.
B magnetic field in the ion source.
C conductance of atoms through the outlet.
$D_\perp$ diffusion coefficient.
d distance between ion source and acceleration electrode.
e charge of an electron.
E_a anode potential in the ion source.
E_h acceleration voltage.
E_l lens potential.
E_p plasma potential.
f ion pairs produced by a primary electron.
I_a current to anode in the discharge chamber.
$I_b I_t$ current to bottom and top plate, respectively.
$\bar{i}_b \bar{i}_t$ mean current density to bottom and top plate.
$\bar{i}_e$ mean current density of electrons.
I_f total current to the filament.
I_f^+ ion current to the filament.
I_f^- electron current to the filament.
I_i ion current to the collector.
$i^+ \bar{i}^+$ density of ion current.
I_s saturation current of electrons emitted from the filament.
K rate of ion production.
k Boltzmann's constant.
l length of discharge chamber.
$\bar{l}$ mean free path.
m mass of a neutral atom.
m' mass of an ion.
m_e mass of an electron.
$n^+ \bar{n}^+$ ion density.
n^- electron density.
p pressure in the discharge chamber.
p_{min} minimum pressure in the discharge chamber.
Q flow of neutral atoms through the outlet.
$\bar{r}$ mean rate of ion production per unit volume.
r_0 Larmor radius.
RP resolving power.
T temperature of discharge chamber.
T_e electron temperature.
x thickness of plasma sheath.
η efficiency.
η_{max} maximum efficiency of the ion source.
θ outlet angle.
ν, ν' number of oscillations carried out by a primary electron.
σ_{ie}, σ_i cross section of ionization.
φ diameter of outlet.

1. Introduction

Several types of magnetic ion sources have been used during the work with the electromagnetic isotope separator (ref. [1])) at the Institute for Theoretical Physics in Copenhagen.

An ion source with electrons oscillating in a magnetic field and with ion extraction in the direction of this field (end extraction) proved to be very useful for the handling of gases.

A preliminary ion source of the same type for solid substances was constructed. The filament supplying electrons to the discharge was mounted inside a closed chamber so that the power fed to the filament also could be used for heating up this chamber (ref. [2])). Satisfactory results were obtained with various substances, such as magnesium, tin, antimony, lead, and bismuth.

The preliminary ion source was used for a systematic investigation of the extracted ion beam and of the plasma discharge. The fact that probe techniques were not applied made it impossible to study the plasma in detail. However, the ion production rate and the threshold pressure for the plasma could be determined by means of measurements of the current to the different electrodes. Furthermore it was studied how the efficiency depends on the geometry and the working conditions of the discharge chamber.

It is important to stress, that in all measurements, the isotope separator has been used for an analysis of the extracted beam. Thus, investigations were carried out only under ion source conditions giving a beam divergence sufficiently small to be accepted by the lens system and the analyzing magnet.

2. Technical Description of Experimental Arrangements

The isotope separator is shown schematically in fig. 1.

[1]) J. Koch, Circ. US. Nat. Bur. Stand. No. 522 (Washington, 1953) p. 165.
[2]) K. O. Nielsen, Nuclear Instruments 1 (1957) 289.

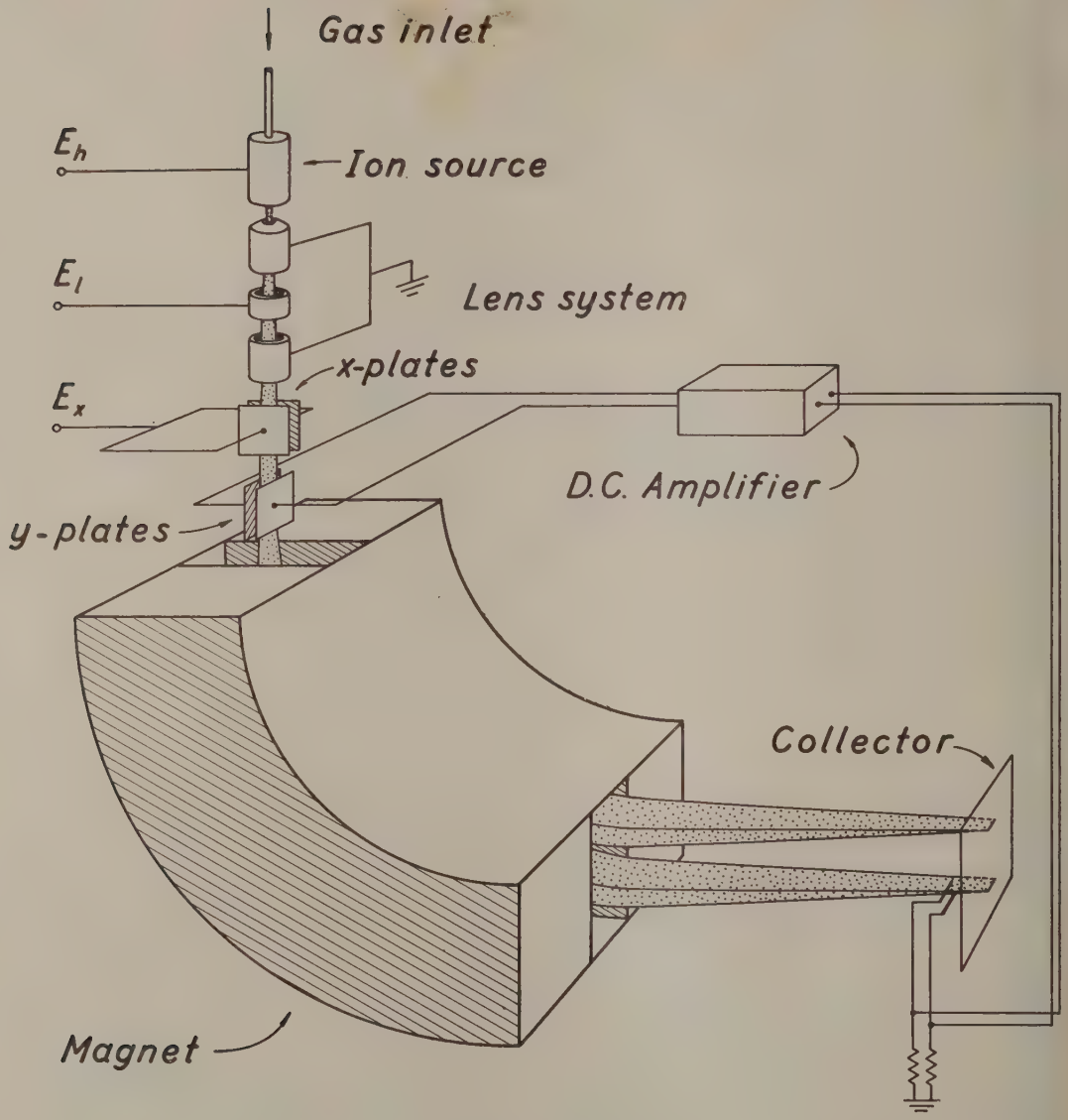

Fig. 1. The electromagnetic isotope separator. Ion source, lens system, x-plates, electromagnet, and collector device are discussed in the text.

2.1. ION SOURCE

The preliminary ion source used for these investigations was similar to the ion source of type III with a discharge chamber of type IIIa (see ref. [2]), section 4, figs. 2 and 3).

2.2. LENS SYSTEM

The lens system consists of three cylindrical electrodes. The ion source is at high potential, E_h, and the first electrode (the acceleration electrode) is at ground potential (see fig. 1). The second cylinder, the focusing electrode, has a potential $E_l = \alpha E_h$ which can be varied so that it yields optimum focusing conditions. E_l is called the lens potential. Also the third electrode is at ground.

Between the lens system and the deflecting magnet two parallel plates are inserted (x-plates in fig. 1); they are fed with an adjustable positive potential of 0–5 kV. When the beam passes between the plates, it is compressed in a direction parallel to the magnetic field. The combined action of the electric field and the magnetic field results in a two-directional focusing of the beam. Spot-focusing of weak ion beams can be achieved with only a small reduction of the resolving power. With stronger ion currents it is possible to compress the focal lines to half the original height.

2.3. MAGNET

The magnet analyzing the beam is a 90° electromagnet with a radius of 80 cm (ref. [3])).

2.4. COLLECTOR SYSTEM

For ion source investigations we are interested only in a collector system allowing the total beam current and the resolving power to be measured conveniently. For accurate measurements of the ion current a small electromagnetic device is used (see fig. 2), where the magnetic

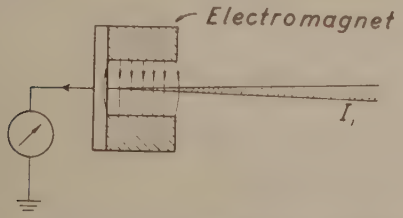

Fig. 2. Arrangement for measuring the ion current at the collector.

field prevents the secondary electrons from leaving the collector. This method has been checked both calorimetrically (ref. [4])) and with a Faraday cage. The same results were obtained with different methods. The magnetic arrangement was preferred.

When only relative values are required, instead the total current to a metal plate is measured. Reproducible conditions can be secured by keeping the plate at —100 volts. Thus, all the secondary electrons are included in the measured current. This simple arrangement can be calibrated by means of the methods mentioned above. However, it should be remembered that the number of secondary electrons depends on the material of the collector plate, the mass of the ions in the beam, the current density, and the acceleration voltage.

The resolving power of the instrument is determined by modulating the acceleration voltage at 50 cycles/sec (ref. [5])), thus sweeping the ion beam over a narrow slit, about 0.1 mm wide, at the collector. The modulating voltage is also connected to the horizontal deflecting system of an oscillograph, while the current passing through the slit is amplified and fed to the vertical deflecting system. From the picture on the oscillograph screen the resolving power is determined by the equation

$$\mathrm{RP} = \frac{B_1}{b_{1/2}} \cdot M \qquad (1)$$

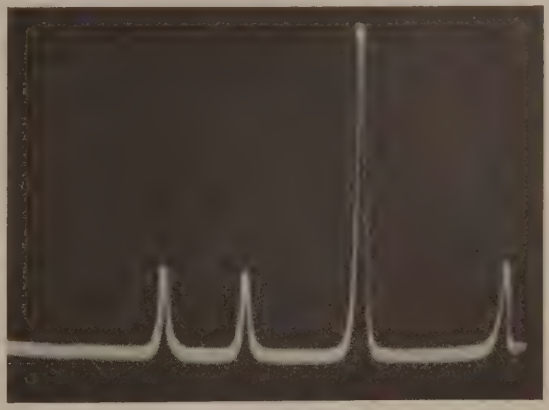

Fig. 3. Krypton mass spectrum. Photo of the oscillograph screen.

where M is the mass number, B_1 the distance on the screen between M and $M + 1$, and $b_{1/2}$ is the half width. A krypton mass spectrum is shown in fig. 5.

[3]) J. Koch and B. Bendt-Nielsen, Mat. Fys. Medd. Dan. Vid. Selsk. **21** (1944) No. 8.

[4]) P. C. Thonemann, Progr. Nuclear Physics **3** (1953) 219.

[5]) C. J. Zilverschoon, Thesis (Amsterdam, 1954).

2.5. VACUUM GAUGES

For ion source investigations we are interested to know the amount of gas, Q μ·l/sec†, that flows through the needle valve into the discharge chamber. To this purpose a Penning gauge and a Pirani gauge are used, both connected to the main vacuum system. The Pirani gauge is calibrated for the inert gas and for air. Inert gases were used for the main part of these experiments. Q is measured in two different ways:

a. At a suitable adjustment of the needle valve the pressure is measured with the Penning gauge. Then, the valves to the diffusion pumps are closed and by means of the calibrated Pirani gauge the rise of pressure per unit time is determined. This procedure is repeated with another adjustment of the needle valve. Provided that the oil diffusion pumps have constant pumping speed, Q μ·l/sec can be plotted as a function of the reading of the Penning gauge.

b. Q has also been determined by measuring the velocity of a drop of mercury in a calibrated glass tube connected to the needle valve. The values of Q obtained by means of these two methods are found to agree satisfactorily.

The pressure p in the discharge chamber can be estimated in the following way. We assume that the entire amount of gas admitted to the ion source passes through the outlet, which has the conductance C l/sec at the temperature t °C. Since the pressure in the discharge chamber is much higher than the pressure in the acceleration chamber, p is determined by

$$p = \frac{Q}{C} \text{ microns.}$$

When calculating C, we assume that the temperature of the discharge chamber is 500 °C.

To avoid effects due to the formation of polyatomic or negative ions, we used noble gases, mainly krypton Prior to the measurements, the ion source is degassed very carefully to ensure that the concentration of undesired ions in the beam is negligible.

† 1 μ·l is the quantity of gas having a volume of one liter at the pressure of one micron, 1×10^{-3} mm Hg.

3. Systematic Investigation of Ion Current and Resolving Power

Using the technique described in the previous section the ion current I_i and the resolving power RP were measured under different conditions. I_i and RP depend on many parameters and it is natural to divide these parameters into various groups.

(*a*) *The ion source parameters*, i.e. the filament heating current I_h, the anode potential E_a, the ion source magnetic field B, the discharge chamber pressure p, and length l. These parameters, except l, can be changed during operation. l can only be changed by changing the ceramic tube (see ref. [3]), fig. 3).

(*b*) *Parameters associated with the acceleration gap* (cf. fig. 4). Here we can change the distance d, the outlet opening area A_0, the outlet angle θ, and the acceleration voltage E_h.

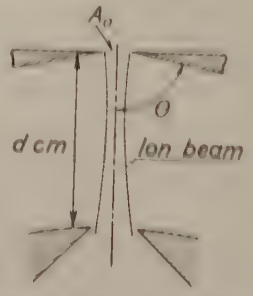

Fig. 4. The acceleration gap. $d = 10$–50 mm, $A_0 = 3.5$–20 mm², $E_h = 20$–65 kV, and $\theta = 55°$–$90°$.

(*c*) Furthermore, I_i and RP depend on the mass number M of the ions and on the lens potential E_l.

3.1. I_i AND RP AS FUNCTIONS OF THE ION SOURCE PARAMETERS

A series of measurements of I_i and RP were carried out for different values of the ion source parameters. (The lens potential was adjusted so as to give the best RP). Fig. 5 shows I_i and RP as functions of I_h — all other parameters except E_l were kept constant. While RP has a pronounced maximum, RP_{max}, I_i increases with I_h over the entire range studied. The value of the ion current corresponding to RP_{max} is I_i^m.

For other values of the parameters B, E_a, l, and p curves similar to those shown in fig. 5

were obtained. They are characterized by the same values of RP_{max} and I_i^m. The fact that I_i^m

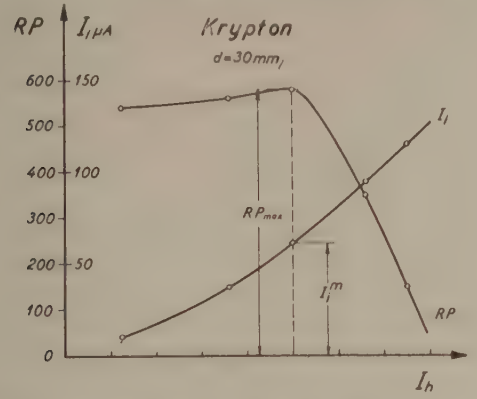

Fig. 5. Ion current and resolving power for krypton vs. filament heating current.

is independent of p appears from fig. 6. Here the pressure in the discharge chamber was varied; for each value of the pressure, I_h was

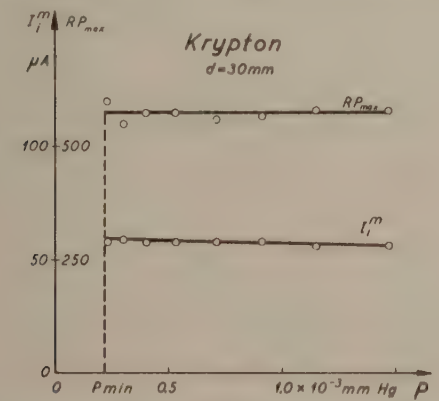

Fig. 6. Ion current and resolving power for krypton vs. pressure in the discharge chamber. (E_h = 50 kV, d = 30 mm, and A_o = 7.0 mm².)

adjusted to yield maximum RP, and the corresponding ion current for I_i^m was measured. For $p > p_{min}$, RP_{max} and I_i^m are independent of p. The discharge in the ion source can only exist for p higher than the minimum pressure p_{min}.

The pressure in the main vacuum system increases slightly with the pressure in the discharge chamber. This leads to increased scattering of the ion beam, and therefore to a slight decrease of I_i.

Many sets of values (B, E_a, l, p) for the ion source parameters yield maximum RP. However, it is important to point out that they all lead to the same values for RP_{max} and I_i^m.

Besides the ion current and the resolving power the efficiency is also of interest for any given separation. However, the efficiency corresponding to RP_{max} is strongly dependent on the ion source parameters (see section 6).

3.2. I_i^m AND RP AS FUNCTIONS OF THE ACCELERATION GAP PARAMETERS

For different values of d, A_o, E_h, and M the ion source parameters I_h, B, E_a, and p were adjusted until maximum resolving power was obtained and RP_{max} and I_i^m were measured. Krypton and argon were used

Figs. 7a, 7b, 8a, and 8b show the dependence of I_i^m on d, A_o, E_h, and M for $\theta = 78°$. An analysis of the curves shows that I_i^m can be represented by the expression

$$I_i^m = C \cdot \frac{A_o \cdot E_h^{3/2}}{d^2 \cdot M^{1/2}} \mu A, \qquad (2)$$

where $C = 0.5 \times 10^{-3}$, A_o is given in cm², d in cm, and E_h in volts.

The constant C depends on the geometry of the electrodes. As the bottom plate (see ref. [3], fig. 3) is interchangeable, it is possible to measure I_i^m and RP for different outlet angles θ. I_i^m as a function of E_h is shown in fig. 9a. The ion current, and thus the constant C, decreases with smaller outlet angles due to the fact that the electric field makes the beam narrower when the outlet angle is smaller. From the curves in fig. 9a the constant C for different values of θ can be calculated.

θ	90°	78°	70°	55°
C	0.5×10^{-3}	0.5×10^{-3}	0.4×10^{-3}	0.2×10^{-3}

A deviation from Eq. (2) occurs at high ion currents, e.g. at $d = 15$ mm and $A_o = 20$ mm² (cf. figs. 7 and 8). Here, the cross section of the beam is so large that it strikes the walls of the analyzing magnet and only a fraction of the ion current is transmitted to the collector.

Eq. (2) indicates that we are not working with a saturated ion current, but with a "space charge limited" current. For fixed electrodes of any ion source. But, from the fact that I_i^m obeys the 3/2-power law, we may conclude that, if the ion source is adjusted to yield maximum RP, the

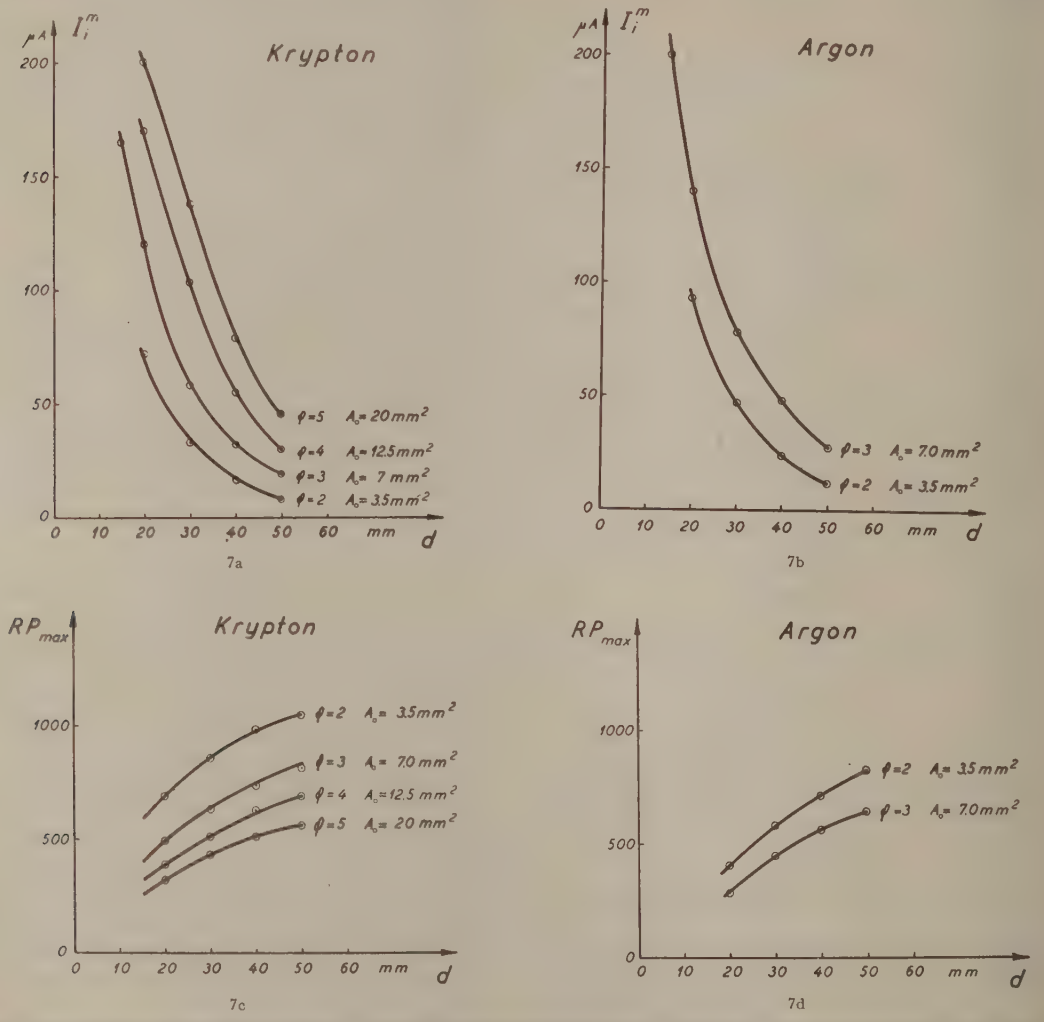

Fig. 7. Ion current and resolving power vs. distance between ion source and acceleration electrode for krypton and argon. Acceleration voltage $E_h = 50$ kV.

shape, the "space charge limited" current varies in proportion to $E_h^{3/2}$ (ref. [6])). We should not expect the 3/2-power law to be valid here because the emitter surface (the boundary between plasma and ion beam, cf. section 4) changes with varying discharge conditions in the shape and size of the plasma boundary at the outlet will always be the same.

The resolving power for different values of d, A_o, E_h, M, and θ is shown in figs. 7c, 7d, 8c, 8d, and 9b. From figs. 8c, 8d, and 9b it appears that the lens potential E_l can be written $E_l = \alpha \cdot E_h$, where α lies in the interval between 0.46 to 0.53. It should be noted that for small d

[6]) I. Langmuir and K. T. Compton, Revs. Mod. Phys. 3 (1931) 191.

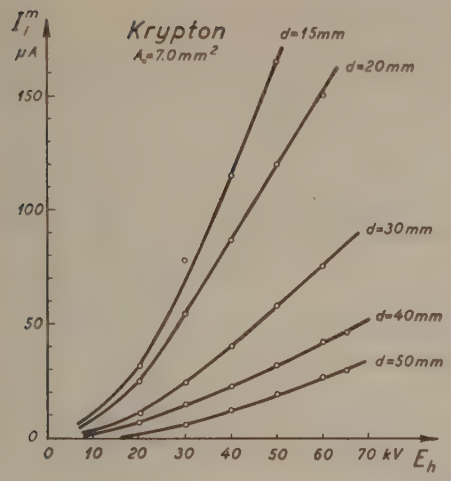

8a

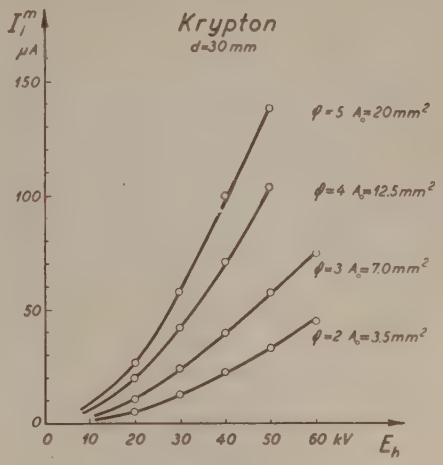

8b

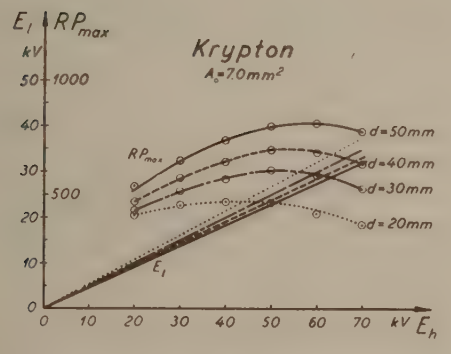

8c

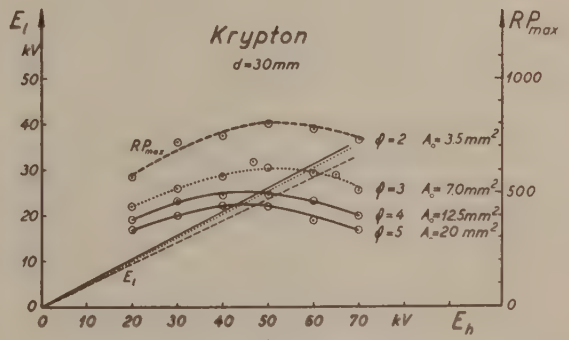

8d

Fig. 8. Ion current, resolving power and lens porential as functions of acceleration voltage for krypton. Similar curves are obtained for argon.

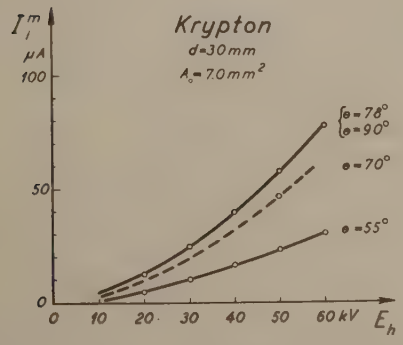

9a

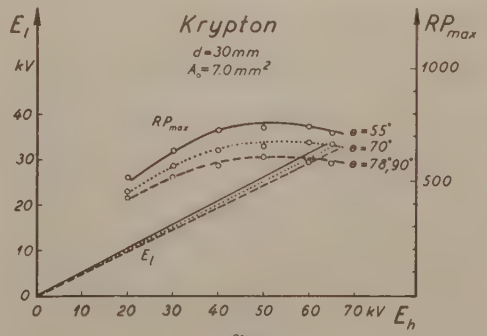

9b

Fig. 9. Ion current, resolving power, and lens potential vs. acceleration voltage. Angle at the outlet as parameter.

and large A_o we have the highest values of α, because a stronger ion current must be refracted more in the lens system to compensate for the higher space charge repulsion. The measurements of RP_{max} for different d and A_o, given in figs. 7c and 7d, can also be represented in another way. Fig. 10 shows that RP for $E_h = 50$ kV is a function of I_i^m only. (Here A_o varies between 3.5 and 20 mm².) Different curves for

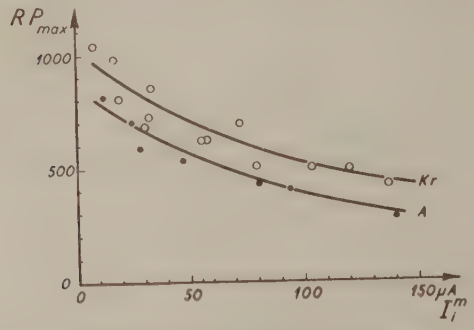

Fig. 10. Resolving power for krypton and argon vs. ion current.

krypton and argon are obtained presumably because there is not exact linearity between the modulation voltage and the horizontal deflecting voltage on the oscillograph.

RP plotted as a function of E_h (figs. 10c, 10d, and 11b) shows a maximum between 40 and 60 kV. This is the result of the combined effects that, at constant I_i^m, RP_{max} increases with E_h (an increase in velocity reduces the effect of space charge repulsion); and at constant A_o and d, the current I_i^m increases with E_h, giving a decrease in RP_{max}.

4. Plasma Description

The geometry of the discharge chamber is shown schematically in fig. 11. The electrons emitted from the filament are attracted by the anode cylinder. The combined action of the electric and magnetic fields causes the electrons to move in helical orbits, while they are oscillating between the top and bottom plates of the discharge chamber. When a gas is present in the chamber, these "primary" electrons cause ionization of the neutral atoms. If the gas pressure is sufficiently high, a plasma is formed which fills nearly the whole discharge chamber. The plasma contains about equal numbers of electrons and ions, and is approximately field-free, since the charges redistribute themselves

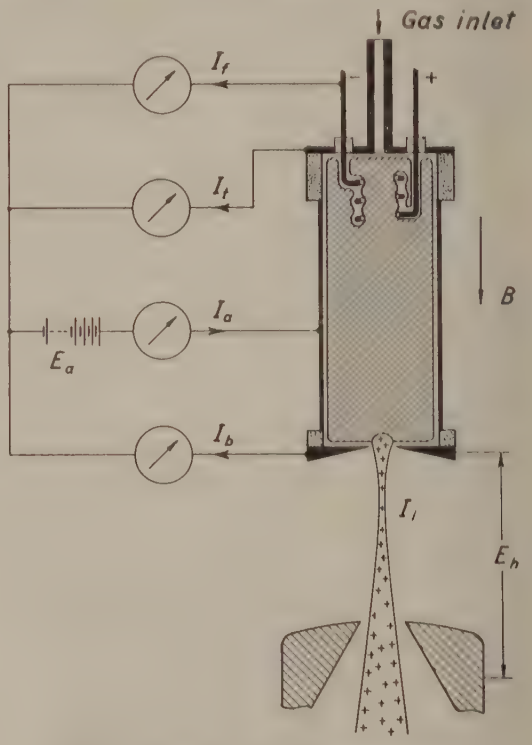

Fig. 11. Geometry of the discharge chamber.

very easily. Furthermore, it surrounds an electrode not at plasma potential with a sheath region, which shields the plasma from the electric field caused by the electrode. In a steady state, the current of ions leaving the plasma is equal to the ion production rate. A similar balance for electrons must be valid.

The potential of a plasma depends on the potentials of the surrounding walls. In a discharge chamber in which all walls have the same potential, the plasma is so much higher than that of the walls that the plasma balance is fulfilled (ref. [7], Ch. 3).

[7]) D. Bohm, E. H. S. Burhop, H. S. W. Massey, and R. M. Williams, in A. Guthrie, R. K. Wakerling, National Nuclear Energy Series I 5: The Characteristics of Electrical Discharges in Magnetic Fields (McGraw-Hill, New York, 1949) Chapters 2, 3, 4, and 9.

In a discharge chamber like that shown in fig. 11, where the top and bottom plates have a lower potential than the anode, the balance is fulfilled with a plasma potential E_p lower than in the previous case. In accordance with measurements made by Kistemaker and Snieder[8]) we assume E_p to be lower than the anode potential E_a. The following types of transitions between plasma and electrodes occur.

4.1. TRANSITION TO THE TOP AND BOTTOM PLATES

Both these electrodes are at a negative potential relative to the plasma. Only very few electrons have sufficient energy to penetrate the potential difference. Thus, a region of positive space charge (positive-ion sheath) is formed near each electrode. Just inside the plasma, between the sheath and the field-free part, a region with a weak electric field accelerates the ions towards the plasma boundary.

The current density through the plasma boundary is (ref. [9]))

$$i^+ \approx n^+ \sqrt{\frac{k \cdot T_e}{2\pi \cdot e \cdot m^+}} \text{ ions/cm}^2 \cdot \text{sec} \qquad (3a)$$

$$i^+ \approx 3.5 \times 10^{-10} \cdot n^+ \frac{T_e^{1/2}}{M^{1/2}} \mu\text{A/cm}^2, \qquad (3b)$$

where n^+ is the density in the plasma, m^+ the mass of an ion in grams, T_e the electron temperature, k Boltzmann's constant, and $e \approx 2.718$.

Thus, i^+ is determined only by n^+ and T_e, while it is independent of the potential difference between plasma and electrode. On the other hand, this potential difference determines the thickness x of the sheath. The current through the sheath is space-charge limited, and for plane electrodes x is given by the equation

$$x = 0.23 \cdot \frac{E_p^{3/4}}{M^{1/4} \cdot (i^+)^{1/2}} \text{ cm}, \qquad (4)$$

where E_p is given in volts and i^+ in μA/cm^2 is obtained from eq. (3b). For $E_p = 100$ volts, $M = 100$, and $i^+ \approx 1$ mA/cm^2, we obtain from eq. (4) $x \approx 0.7$ mm.

[8]) J. Kistemaker and J. Snieder, Physica **XIX** (1953) 950.
[9]) D. Kamke and H.-J. Rose, Z. Phys. **145** (1956) 83.

4.2. TRANSITION TO THE ION BEAM

The transition to the ion beam is very similar to the transition to the top and bottom plates. The current density i^+ out of the plasma is given by eq. (3) and depends only on n^+ and T_e inside the plasma. The size A_p and shape of the plasma boundary (fig. 12) are determined from the condition that I_i must be equal to the current passing A_p. The plasma boundary follows an equipotential surface whose shape causes a convergence of the ion beam at the outlet. Therefore, both the ion current I_i and the resolving power depend strongly on A_p.

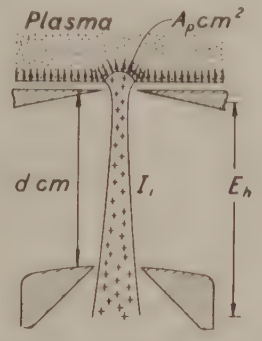

Fig. 12. Plasma boundary at the outlet of the ion source. A_p is the area of the ion omitting surface through which ions are extracted to the ion beam.

For an arbitrary set of values of the ion source parameters we get, instead of eq. (2),

$$I_i = C\,(A_p, \theta) \frac{A_o \cdot E_h^{3/2}}{d^2 \cdot M^{1/2}} \mu\text{A}. \qquad (5)$$

Using eqs. (3) and (5) the balance can be expressed by

$$i^+ \cdot A_p \cdot \varepsilon = n^+ \sqrt{\frac{k \cdot T_e}{2\pi \cdot e \cdot m^+}} \cdot A_p \cdot \varepsilon = C\,(A_p, \theta) \cdot \frac{A_o}{d^2} \cdot \frac{E_h^{3/2}}{M^{1/2}}, \qquad (6)$$

where ε is the charge of an electron in microcoulomb.

The current density i^+ can be changed by varying the ion source parameters. From eq. (6) it follows that A_p together with both I_i and RP depend on these parameters.

For $\theta = 78°$ and the ion source parameters adjusted to maximum RP, we have $C(A_p \cdot \theta) =$

0.5×10^{-2} (cf. 3.2). In this particular case we get from eq. (6)

$$n^+ \approx 0.65 \times 10^{-14} \sqrt{\frac{2\pi e}{k \cdot T_e}} \cdot \frac{A_o}{A_p} \cdot \frac{E_h^{3/2}}{d^2} \cdot \frac{1}{\varepsilon} \text{ ions/cm}^3 \quad (7a)$$

or

$$n^+ \approx 5 \times 10^4 \cdot \frac{E_h^{3/2}}{d^2} \text{ ions/cm}^3, \quad (7b)$$

where we insert $A_p/A_o \approx 1.3$ (cf. fig. 14), and $T_e \approx 50000°$ K (D. Bohm *et al.*, ref. [7]), Ch. 9).

In general, we have $E_h = 50000$ volts and d between 10 and 40 mm. This gives an ion density from 10^{10} to 5×10^{11} ions/cm^3.

4.3. TRANSITION TO THE FILAMENT

The filament is surrounded by a double layer consisting of positive ions, concentrated at the plasma boundary, and emitted electrons next to the filament. The maximum electron current which can pass through the double layer is space charge limited and given by the equation (ref. [10,11]) and ref. [7]), Ch. 4).

$$I_f^- = \gamma \cdot \sqrt{\frac{m^+}{m_e}} \cdot I_f^+, \quad (8)$$

where γ is a correction factor depending on the state of the filament and varying from 1/3 to 2/3. I_f^+ is the ion current reaching the boundary from the plasma and m_e the mass of an electron.

However, it is not always I_f^+ that limits I_f^-. The electron current leaving the filament can never exceed the saturation current I_s corresponding to the temperature of the filament. In the case of a saturation current, we have a non-zero field at the surface of the filament and instead of eq. (8) we obtain

$$I_f^- = I_s < \gamma \sqrt{\frac{m^+}{m_e}} \cdot I_f^+. \quad (9)$$

The presence of electrons in the double layer reduces the effective space charge density of positive ions, and therefore the double layer is thicker than a single sheath (cf. eq. (4)) with the same positive ion current (ref. [7]), Ch. 4).

4.4. TRANSITION TO THE ANODE

Since the plasma potential is lower than the anode potential, no ion current can pass to the anode. As mentioned above, only a few electrons can reach the top and bottom plates. Hence, in a stationary state, almost all electrons—the primary electrons from the filament and the electrons produced by ionization in the plasma—must flow to the anode in spite of the axial magnetic field. Several effects contribute to the transport of electrons to the anode.

(a) Collisions with neutral atoms and ions scatter the center of the Larmor orbits in random directions, and in this way a kind of diffusion of electrons perpendicular to the magnetic field occurs. As a result of the focusing of the primary electrons by the magnetic field the ion production takes place mainly in a cylindrical column just below the filament; the ion density is highest here and decreases towards the anode (compare ref. [7]), Ch. 4).

(b) Oscillations in the plasma cause a dynamical "drain diffusion" to the anode (D. Bohm *et al.*, ref. [7]) Ch. 2 and 9). Electrical waves in the plasma circulate around the center of the discharge, giving electrical forces transverse to the radius. Due to these forces electrons drain both inwards and outwards and, since the density of electrons is decreasing towards the wall, the average drain is outwards.

(c) At a pressure so low that there is no plasma, and even at the lowest obtainable pressure, the anode current is still about 1/5 of its value with a plasma present. Here the number of collisions with atoms and ions is insufficient to produce the measured anode current and, therefore, there must be other mechanisms which bring electrons out to the anode.

5. Ion Production Rate

5.1. PRELIMINARY DISCUSSION OF THE ION PRODUCTION

Let us assume that all electrons oscillate between the top and bottom plates of the discharge chamber until they hit the anode. The primary electrons ionize as long as their energy exceeds the value of the energy corresponding to the ionization potential of the gas in question. Secondary electrons can be liberated

[10]) I. Langmuir, Phys. Rev. **33** (1929) 954.
[11]) I. Langmuir, Phys. Rev. **34** (1929) 876.

with appreciable energies. Some of these electrons have sufficient energy to cause further ionization. Considering all processes of ionization, we assume that, in the mean, each primary electron produces f ion pairs. Thus, the current to the anode can be written

$$I_a = I_f^- + f \cdot I_f^- = (1 + f)\, I_f^- \,\dagger . \qquad (10)$$

For the rate of ion production we find

$$K = f \cdot \frac{I_f^-}{e} = \frac{1}{e}(I_a - I_f^-) \text{ ions/sec.} \qquad (11)$$

At high pressure, the dominant mechanism responsible for the motion of electrons to the anode is expected to be diffusion by collision with neutral atoms and ions. For a constant magnetic field it is reasonable to assume that the average number of collisions made by an electron on its way to the anode is independent of the pressure p in the discharge chamber. Since a certain fraction of these collisions results in ionization, f should also be independent of p.

At low pressures, in addition to collisions other factors are important for the transport of electrons towards the anode, and f therefore decreases with decreasing p.

In the pressure region where f is independent of p the total length of the electron path, and thus the number of oscillations, ν, is inversely proportional to p (ν is the number of oscillations an electron must carry out to hit the anode). At low pressures, however, ν can be expected

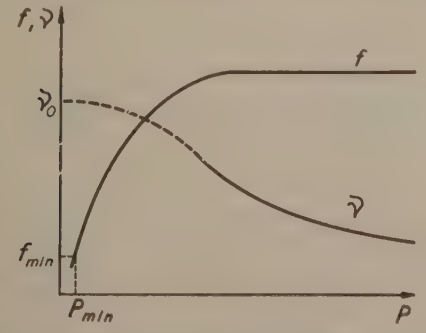

Fig. 13. Number of ion pairs produced by a primary electron and number of oscillations made by an electron vs. pressure.

† According to von Engel (ref. [12])) the recombination rate of electrons and ions is 10^4 times less than the ionization rate. The recombination can thus be neglected.

to be independent of p. We thus assume the variation of f and ν with p to be that indicated in fig. 13.

A measurement of f and K from eqs. (10) and (11) requires the determination of both I_a and I_f^-. However, I_f^- cannot be measured directly. Nevertheless, it is possible under certain conditions to determine f and K.

The total current to the filament is

$$I_f = I_f^+ + I_f^- . \qquad (12)$$

If the electron current I_f^- is space charge limited and given by eq. (8), we have for all mass numbers

$$I_f^- \gg I_f^+ \qquad (13)$$

which, together with eq. (12) gives $I_f \approx I_f^-$. But, if measurements show that I_f is appreciably higher than I_s, and thus also higher than I_f^-, we see from eq. (12) that I_f^+ is of the same order as, or higher than I_f^-. Hence, according to eq. (13), the electron current from the filament cannot be space charge limited and therefore we have $I_f^- = I_s$. Since I_s can always be measured (see below), f and K can be determined from eqs. (10) and (11), provided that $I_f > I_s$.

5.2. MEASUREMENTS OF THE ION PRODUCTION

The arrangement shown in fig. 11 was used for measurements of I_a, I_t, I_b, and I_f as functions of the pressure, p, in the discharge chamber (I_t and I_b being the currents to the top and bottom plates, respectively). For each value of the filament heating current I_h we also measured I_s, taking it to be the saturation current to the anode without magnetic field and without gas input. The measurements were carried out with krypton; E_h and d were kept constant. For each value of p, I_h was adjusted to give maximum RP.

In figs. 14a and 14b the measured currents are plotted as functions of the pressure in the discharge chamber. For $p > 1.5 \times 10^{-3}$ mm Hg, the currents are nearly independent of p. At $p = 0.1 \times 10^{-3}$ mm Hg, there is a well defined and reproducible threshold pressure, p_{min}, where the plasma disappears. We also find that, for $p > p_{min}$, the condition $I_f > I_s$ is fulfilled and

[12]) A. von Engel, Ionized Gases (Oxford, 1955).

therefore we have $I_f^- = I_s$. Thus it is possible to determine f from eq. (10).

As shown in fig. 14b, f depends on p, as indicated in fig. 13. For $p > 1.5 \times 10^{-3}$ mm Hg, f is a constant, while f decreases with decreasing pressure for $p < 1.5 \times 10^{-3}$ mm Hg.

Eq. (11), $I_f^- = I_s$, and f give the ion production rate

$$K = \frac{f \cdot I_f^-}{\varepsilon} = \frac{f \cdot I_s}{\varepsilon}. \qquad (14)$$

The curves for f and I_s shown in fig. 14b indicate that the product $f \cdot I_s$, and thereby K, is constant for all values of p down to p_{min}. When f decreases as a result of decreasing p, I_f^- has to be increased; this can be done by increasing I_h, as long as we have a saturation current $I_f^- = I_s$.

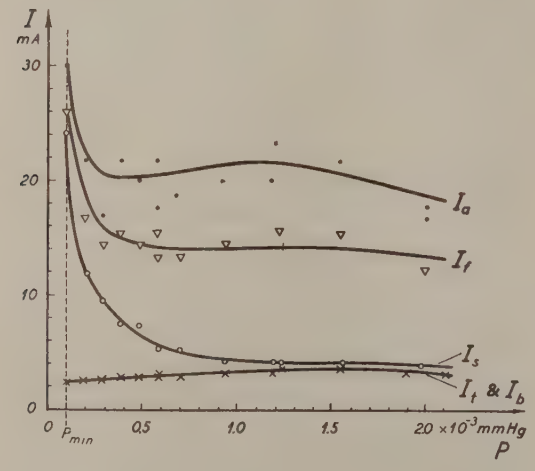

14 a

It has been shown that both K and i^+ are constant during measurements in which the ion source is operated at conditions giving maximum resolving power. It is reasonable to assume that, in general, i^+ is proportional to K. Therefore, the adjustment to maximum RP means that the ion source parameters are adjusted until K gives the correct size and shape of the plasma boundary at the outlet. The ion source parameters that can be changed during operation are I_a, E_h, B, and p. The dependence of K on these parameters will be discussed in the following.

(*a*) *The filament heating current* I_h

Since $I_f^- = I_s$ for $p > p_{min}$, K can be regulated by I_h.

Fig. 5 is an illustration of this result. For small values of I_h, K (and i^+) is also small and the plasma boundary is relatively larger and more curved. This gives a narrow beam and therefore

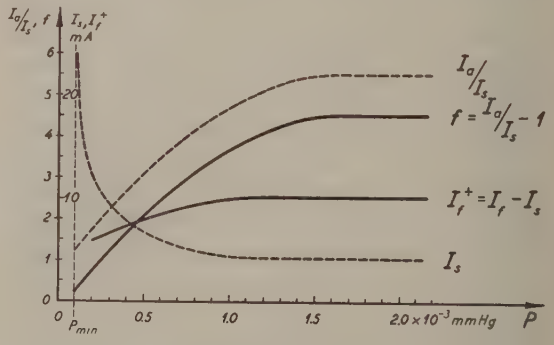

14 b

Fig. 14. Saturation current from the filament, currents to the anode, filament, top and bottom plates vs. pressure in the discharge chamber for krypton. Anode potential $E_a = 100$ volts, magnetic field $B = 350$ gauss, and length of the discharge chamber $l = 55$ mm. ($E_h = 50$ kV, $d = 30$ mm and $A_o = 7.0$ mm².)

In accordance with fig. 6, both RP_{max} and I_i^m were found to be constant for $p > p_{min}$. From the equation $i^+ \cdot A_p = I_i^m$ and $A_p = \text{constant} =$ the size and shape that give maximum RP (see 4.2), it follows that i^+, the current density to the ion beam, also is constant. Furthermore we find from fig. 14a that I_f^+, I_t and I_p are approximately constant almost down to P_{min}, which indicates that all positive current densities out of the plasma are kept constant.

also a smaller value of I_i. By increasing I_h K is increased; this results in a smaller and flatter plasma boundary, which again gives a less convergent beam and a higher I_i. A certain shape of the plasma boundary corresponds to optimum focusing conditions, and therefore a maximum for RP is obtained (cf. fig. 5).

(*b*) *The anode voltage* E_a

Since the ionization cross section σ_i, varies

with the electron energy, f and K can be changed by changing E_a.

(*c*) *The magnetic field B*

For $p > 1.5 \times 10^{-3}$ mm Hg, f is constant (cf. fig. 14); this confirms the assumption that the electrons reach the anode as a result of diffusion by collision with neutral atoms and ions. The equivalent diffusion coefficient, $D_\perp$, for the motion of electrons perpendicular to the magnetic field is (D. Bohm *et al.*, ref. [7]) Ch. 2)

$$D_\perp = \frac{\bar{v}}{4\bar{l}} \cdot r_0^2 \text{ cm}^2/\text{sec}, \qquad (15)$$

where $\bar{v}$ is the mean electron velocity, r_0 is the Larmor radius, and $\bar{l}$ is the mean free path. Inserting into eq. (15) the two cross sections σ^0 and σ^+ for collisions between electrons and neutral atoms and ions, respectively, we get

$$D_\perp = \frac{1}{4} \cdot \bar{v}^3 \cdot \frac{m_e^2 \cdot c^2}{\varepsilon^2 \cdot B^2} (\sigma^+ \cdot n^+ + \sigma^0 \cdot n_0). \qquad (16)$$

Since the number of collisions an electron must undergo in order to reach the anode, and with this f, is inversely proportional to $D_\perp$, f must be proportional to B^2. This relationship can be checked by experiments. For different values of B the filament heating current, I_h, is adjusted until maximum RP is obtained, and I_a is measured. Now K, and thereby the product, $f \cdot I_f^-$, is kept constant and, if f is proportional to B^2, then I_f^- must be inversely proportional to B^2. Using eqs. (10) and (11) we get

$$I_a = \text{const} \cdot \frac{1}{B^2} + K \cdot \varepsilon. \qquad (17)$$

I_a is plotted in fig. 15 as a function of B, and the agreement between the shape of the curves in dependence on $1/B^2$ and eq. (17) is satisfactory.

(*d*) *The pressure p*

For $p < 1.5 \times 10^{-3}$ mm Hg (cf. fig. 14) f depends on p. Thus, also K depends on p (eq. (14)).

Taking the values for f and I_s from fig. 14b we get for the ion production rate

$$K \approx 10^{17} \text{ ion/cm}^3.$$

With a filament of area $A_f = 5$ cm^2, we obtain the current density to the filament $i_f^+ \approx 2$ mA/cm^2. Because of the double layer around the filament, the area of the plasma boundary is larger than the area of the filament itself, and therefore the real current density is slightly lower than 2 mA/cm^2.

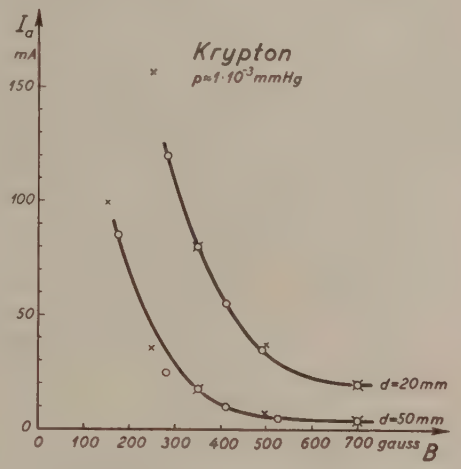

Fig. 15. Anode current as a function of the magnetic field. x from eq. (17), o experimental.

For the top and bottom plates we find the average current density $\bar{i}_t \approx \bar{i}_b \approx 0.8$ mA/cm^2. It is not surprising that i_f^+ is higher than $\bar{i}_t$ and $\bar{i}_b$, since the ion density is highest in a cylindrical column below the filament.

From i_f^+, $\bar{i}_t$, and $\bar{i}_b$ an average density of ion current $\bar{i}^+$ from the plasma can be calculated. $\bar{i}^+ \approx 1.2$ mA/cm^2 is found.

The current through the outlet is 60 μA, which means a current density at the outlet of about 0.6 mA/cm^2.

The filament has a mean potential of about 5 volts higher than that of the cathode (top and bottom plates). Electrons emitted with a sufficient energy will strike the cathode without oscillating in the discharge chamber. To avoid this effect some measurements were made with the filament at a potential of 7 volts. The results are shown in figs. 16a and 16b, measured otherwise under the same conditions as in figs. 14a and 14b. A comparison between figs. 14 and 16 shows that f reaches a constant value at a lower pressure in the second case.

5.3. MINIMUM PRESSURE

Assuming that the current density to the filament is proportional to the ion production rate

$$i_f^+ = g \cdot K \cdot \varepsilon \text{ mA/cm}^2, \tag{18}$$

where g is a constant. From eq. (11) we obtain

$$I_f^+ = A_f \cdot g \cdot f \cdot I_f^- \text{ mA}. \tag{19}$$

During the whole measurement, $I_f^- = I_s$ for $p > p_{min}$ (cf. fig. 16 and § 4.3). If, on the other hand, I_f^- is space charge limited, eqs. (8) and (19) show that a decrease in I_f^+ causes a decrease in I_f^-, which results in an additional decrease in I_f^+. Hence, the plasma is always unstable when I_f^- has the maximum value given by eq. (8). For a stable plasma, the ion current to the filament must be so high that it ensures $I_f^- = I_s$. This means that I_f^+ has to satisfy the condition

$$I_f^+ > \frac{1}{\gamma} \sqrt{\frac{m_e}{m^+}} \cdot I_s.$$

By substitution of this into eq. (19) we find

$$f > \frac{1}{A_f \cdot g \cdot \gamma} \sqrt{\frac{m_e}{m^+}} = f_{min}. \tag{20}$$

From fig. 13 it appears that $f > f_{min}$ corresponds to $p > p_{min}$. According to fig. 16, f decreases when p is decreased below 1.5×10^{-3} mm Hg. To keep K constant we must increase I_f^- (eq. (14)). As long as $I_f^- = I_s$, this can be achieved by increasing the filament heating current (see § 4.3). When I_f^- is limited according to eq. (8), a further increase in the filament heating current cannot increase I_f^-. Then the plasma becomes unstable and disappears.

The minimum pressure is determined in the following way.

The gas inlet to the ion source is reduced in small steps, while the resolving power of the instrument is kept at its maximum value (fig. 8). Just before the discharge disappears, there is a very small pressure interval in which the discharge shifts between two states. (Observed on the oscillograph during RP determination.) The pressure, used for p_{min}, is well defined and reproducible. One of these states corresponds to the normal running conditions of the ion source, while the other has a much lower ion production. If the pressure is reduced by one more fraction the discharge can exist only in the latter state. At a slightly lower pressure the discharge disappears completely. The phenomena described here have also been observed by Bohm (ref. [7]) Ch. 4).

The fact that the minimum pressure (determined in this way) is well defined and reproducible enables us to carry out a systematic

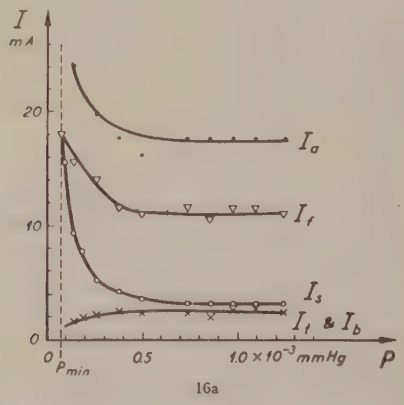

16a

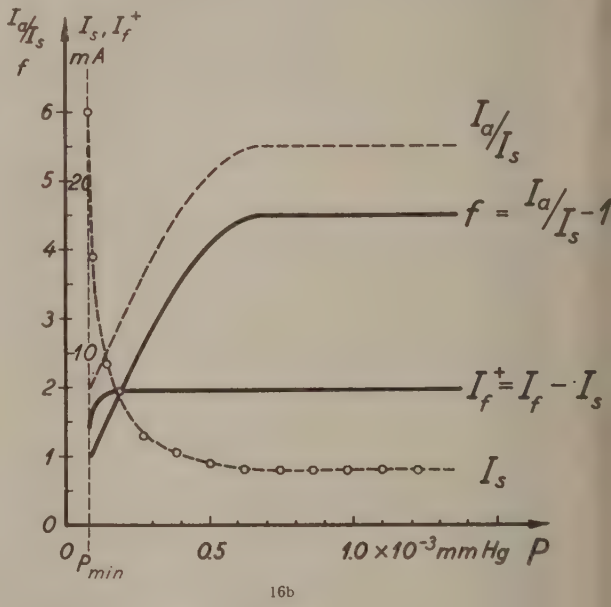

16b

Fig. 16. Potential of the filament 7 volts higher than that of the cathode. Otherwise the same conditions as in fig. 14.

investigation of p_{min} as a function of the geometry and the working conditions of the discharge chamber.

When the pressure approaches p_{min}, high frequency oscillations occur sometimes in the ion source, and are reproduced in the ion current. These oscillations are called "hash", and are gradually shifted over to relaxation oscillations. However, frequently the discharge is stable (no hash) until it disappears at $p = p_{min}$.

6. Efficiency

The efficiency can be expressed by

$$\eta = \frac{I_i}{q \cdot \varepsilon + I_i}, \tag{21}$$

where q is the gas consumption in atoms/sec (compare 2.5). For the ion source adjusted to maximum RP

$$\eta^m = \frac{I_i^m}{q \cdot \varepsilon + I_i^m}. \tag{22}$$

Since the ion current I_i^m is independent of the pressure in the discharge chamber (fig. 8) and the consumption of neutral atoms is proportional to p, the highest efficiency η_{max} is obtained for p just above p_{min}.

The flow of neutral atoms through the outlet of the discharge chamber is

$$q = n_0 \sqrt{\frac{k \cdot T}{2\pi \cdot m}} \cdot A_o \text{ atoms/sec.} \tag{23}$$

Here, n_0 is the density of neutral atoms in the chamber, T the temperature, and m the mass of an atom. Now, the efficiency can be written

$$\eta^m = \frac{I_i^m}{q \cdot \varepsilon + I_i^m} \approx \frac{I_i^m}{q \cdot \varepsilon} \approx 3 \times 10^5 \cdot \frac{1}{n_0} \cdot \frac{E_h^{3/2}}{d^2}, \tag{24}$$

where I_i^m is taken from eq. (2) and $T = (500 + 273)°$ K. Using eq. (3) instead of eq. (2) we get (ref. [13])

$$\eta = e^{-\frac{1}{2}} \cdot \frac{n^+}{n_0} \cdot \sqrt{\frac{T_e}{T}} \approx 4 \frac{A_p}{A_o} \cdot \frac{n^+}{n_0} \tag{25a}$$

or

$$\eta^m = 5 \cdot \frac{n^+}{n_0}, \tag{25b}$$

where $T_e = 50000°$ K and $A_p/A_o \approx 1.3$.

Here n^+ depends on the required RP and on the acceleration gap parameters, while n_0 is a function of the geometry and the working conditions of the discharge chamber.

From eq. (25b), which is only valid for small n, we see that $n_0 \gg n^+$. Under this condition the mean rate of ion production per unit volume can be written

$$\bar{\nu} = \sigma_{ie} \cdot \bar{i}_e \cdot n_0 \text{ ions/cm}^3 \text{ sec}, \tag{26}$$

where σ_{ie} is the "effective"† ionization cross section which must be a function of E_a. $\bar{i}_e$ is the average flux of ionizing electrons that goes through one cm² per sec and depends on I_f^- and on the number of oscillations ν' that an electron must carry out to be slowed down below the energy corresponding to the ionization potential. ν' is expected to be a function of l, E_a, and B. For i_e we have

$$\bar{i}_e \approx \frac{I_f^-}{\varepsilon \cdot A_t} \cdot 2\nu' \text{ electrons/cm}^2 \text{ sec},$$

where A_t is the cross sectional area of the discharge chamber, used as an approximation for the real area of the discharge. The total rate of ion production is

$$K = \bar{\nu} \cdot A_t \cdot l = \frac{2}{\varepsilon} \cdot I_f^- \cdot \sigma_{ie} \cdot \nu' \cdot l \cdot n_0. \tag{27a}$$

At threshold pressure, $I_f^- = I_s$ is given by eq. (8). K and n^+ are uniquely determined by the acceleration gap and acceleration voltage (cf. § 3.2). With d and E_h constant I_f^+ is also constant, since it is proportional to K (cf. § 4.3). Therefore $I_f^- = I_s = (I_s)_{max} = \text{constant}$. Introducing this into eq. (27a) we obtain

$$(n_0)_{min} \cdot l \cdot \nu' \cdot \sigma_{ie} = \text{constant}, \tag{27b}$$

where $(n_0)_{min}$ is the density of neutral atoms corresponding to p_{min}. The maximum efficiency for a certain d and E_h is therefore, according to eq. (24),

$$\eta_{max} = c_1 \cdot l \cdot \nu' \cdot \sigma_{ie}, \tag{28}$$

where c_1 is a constant.

Thus the efficiency depends on both the geometry and the working conditions of the discharge chamber. It is difficult to change

[13]) W. Fischer und W. Walcher, Z. Naturforschg. 10a (1955) 857.

† In the "effective" ionization cross section we include all processes of ionization.

the diameter of the discharge chamber but it is easy to vary its length. The working conditions of the ion source can be varied during operation with respect to the anode potential, E_a, and the magnetic field, B.

6.1. INFLUENCE OF GEOMETRY ON THE EFFICIENCY

If we keep the working conditions of the ion source constant (E_a and B are constant) σ_{ie} is a constant. From eq. (28) we find the maximum efficiency to be

$$\eta_{max} = c_2 \cdot l \cdot \nu', \tag{29}$$

where c_2 is a constant.

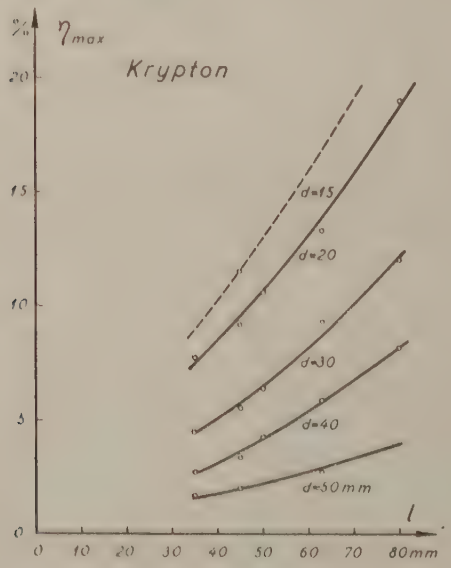

17a

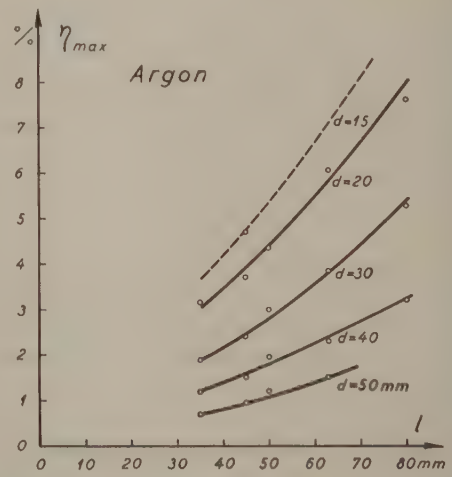

17b

Fig. 17. Maximum efficiency for krypton and argon vs. length of the discharge chamber. $E_a = 100$ volts and $B = 350$ gauss. ($E_h = 50$ kV, $d = 15$–50 mm and $A_0 = 7.0$ mm^2.) For $d = 15$ mm, see § 3.2.

In order to determine the dependence of η_{max} on l and d, a series of measurements were made with krypton and argon. I_i and Q corresponding to p_{min} were measured and η_{max} was calculated. Figs. 17a and 17b show η_{max} as a function of l with d as a parameter.

It was found that η_{max} is approximately inversely proportional to d^2, in accordance with eq. (24).

If, near $p = p_{min}$, ν' is independent of l, η_{max} is proportional to l, according to eq. (29). Fig. 17 shows that η_{max} increases faster than proportionally to l at a constant d-value, and from eq. (29) we infer that ν' increases slightly with l. For still longer discharge chambers, η_{max} is expected to reach an upper limit.

If the only mechanism transporting electrons to the anode were diffusion by collisions, $l \cdot \nu'$ would be a constant, and η_{max} independent of l. The increase with l indicates the existence of other mechanisms at low pressures.

In this connection it should be remembered that some scattering in the main vacuum system takes place. The maximum efficiency of the ion source is therefore slightly higher than η_{max} given in figs. 19a and 19b.

6.2. INFLUENCE OF WORKING CONDITIONS ON THE EFFICIENCY

For a constant l the maximum efficiency is found from eq. (28) to be

$$\eta_{max} = c_3 \cdot \nu' \cdot \sigma_{ie}, \tag{30}$$

where c_3 is a constant.

Figs. 18a and 18b show the variation of η_{max} with E_a for four noble gases. The relative variation of the cross section for ionization σ_{ie}† is also indicated in fig. 18. The constant of proportionality is chosen such that the experimental and relative curves coincide for $E_a = 100$ volts.

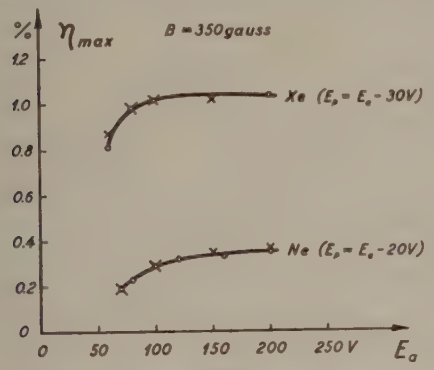

18a

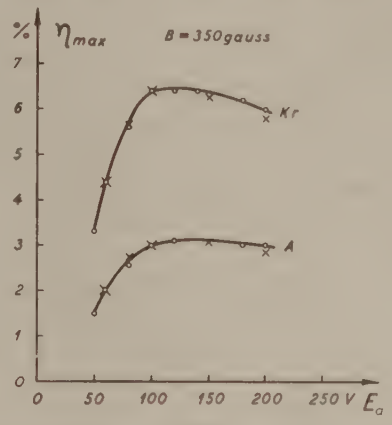

18b

Fig. 18. Maximum efficiency for neon, argon, krypton, and xenon vs. anode potential in the ion source. B = 350 gauss and $l = 50$ mm. ($E_h = 50$ kV, $d = 30$ mm and $A_o = 7.0$ mm².) o experimental, x from eq. (30) with $\nu' =$ constant.

For argon, krypton, and xenon σ_i is taken for an electron energy equal to E_a — 30 eV. E_a — 20 eV is used for neon. It is seen that proportionality between η_{max} and σ_i is in good agreement with our experiments. This indicates that, at $p = p_{min}$, ν' is nearly independent of E_a, and σ_{ie} is proportional to σ_i, which was to be expected since, at $p = p_{min}$, the number of ionizations per electron is less than 1 (fig. 14).

The variation of η_{max} with B is shown in fig. 19.

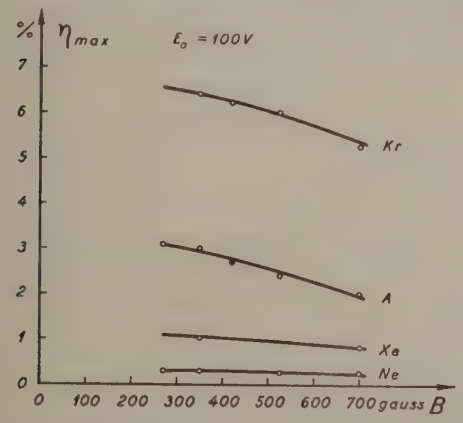

Fig. 19. Maximum efficiency for neon, argon, krypton, and xenon vs. magnetic field in the ion source. $E_a = 100$ volts and $l_2 = 50$ mm. ($E_h = 50$ kV, $d = 30$ mm and $A_o = 7.0$ mm².)

† For the cross section of ionization for neon and argon, see Landolt-Börnstein (ref. [14])); for krypton and xenon, see Tate and Smith (ref. [15])).

η_{max} decreases with increasing magnetic field; however, at lower B, η_{max} decreases with decreasing magnetic field and therefore a maximum of η_{max} for B in the region of 100 to 200 gauss is expected.

The variation of p_{min} with E_h has also been studied. The result of this investigation, illustrated in fig. 20, shows that a higher E_h requires a higher pressure. The necessary increase in gas

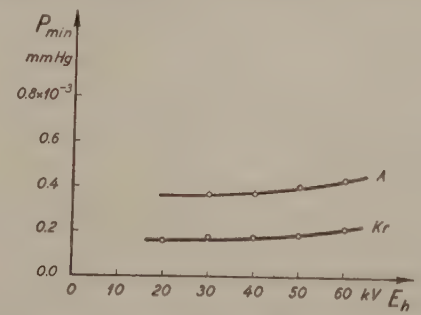

Fig. 20. Minimum pressure in the discharge chamber for argon and krypton vs. acceleration voltage. $E_a = 100$ volts, $B = 350$ gauss, and $l = 50$ mm. ($E_h = 20$–60 kV, $d = 30$ mm, and $A_o = 7.0$ mm².)

[14]) Landolt-Börnstein, 6. Aufl., I. Band, 1. Teil, Atome und Ionen (1950).

[15]) J. T. Tate and Ph. T. Smith, Phys. Rev. **46** (1934) 773.

consumption is approximately equivalent to the rise in ion current. p_{min} can thus be considered to be the sum of a constant pressure (p_{min} at $E_h = 0$) and an additional pressure corresponding to the extracted ion current.

6.3. EFFICIENCY FOR DIFFERENT GASES

In the following table the values of η_{max} are given for neon, argon, krypton, and xenon, determined under equal experimental conditions, viz. $E_h = 50$ kV, $A_o = 7.0$ mm², $d = 30$ mm, and $l = 50$ mm. (Conditions for radon, see below).

Gas	η_{max}	σ_i (relative)
Neon	0.3	1
Argon	3.0	6
Krypton	6.4	
Xenon	1.0	
(Radon	29)	

For the relative values of σ_i at 80 eV, (cf. ref. [14]). $\sigma_i = 1$ for neon has been chosen arbitrarily. Since both p_{min} and the conductance of the outlet opening for neutral atoms depend on the mass, we should not expect proportionality between η_{max} and σ_i.

Since in general σ_i, and consequently η_{max}, increase with the mass number, the low efficiency found for xenon is surprising.

The results obtained from our measurements on noble gases allow us to conclude that highest efficiency is obtained under the following conditions:

(a) Long discharge chamber.
(b) Small distance between ion source and acceleration electrode.
(c) High acceleration voltage.
(d) Anode potential 100–140 volts for argon and krypton, 150–200 volts for neon and xenon.
(e) Magnetic field 100–200 gauss.

In a few cases it has been possible to measure η by means of another method. The isotope separator was used for preparing sources of Em^{222} for beta- and gamma spectroscopy by direct deposition on thin Al-foils (K. O. Nielsen *et al.*, ref. [16]). From measurements of the activity of the starting material and the activity of the collected radon the overall efficiency can easily be evaluated. The value of η includes the efficiency of the direct deposition method. In this case, when the ions are much heavier than the atoms of the target material—here aluminum—the collection efficiency is supposed to be high[17]). The highest efficiency obtained is about 22% with $l = 66$ mm and $d = 40$ mm. Supposing η to be proportional to l and inversely proportional to d^2, we get $\eta = 29\%$ for $d = 30$ mm and $l = 50$ mm. This is about four times the efficiency found for krypton at the same l and d. However, these measurements cannot be directly compared, since, during separation of Em^{222}, bismuth was evaporated simultaneously from the oven for mass marking and for stabilizing the position of the beam.

6.4. EFFICIENCY FOR SOLID CHARGING MATERIAL

For materials with a considerable vapour pressure at the temperature of the discharge chamber, there will be no loss by condensation in the ion source. In this case, the operating mechanism of the source is expected to be the same as for gases. For tin, lead, and bismuth the efficiencies correspond to those found for noble gases under the same experimental conditions.

The situation is different for elements evaporating at higher temperatures than usually obtained in the discharge chamber. Instead of a pure element, it is necessary to use chemical compounds—such as chlorides and oxides—which have a suitable vapour pressure. By decomposition and ionization in the plasma, atomic ions are formed and many of these are drawn to the top and bottom plates; if the temperature here is too low these atoms are lost from the discharge due to condensation.

In section 5.2 we have shown that the density of ion current through the plasma boundary to the ion beam is approximately the same as the current to the top and bottom plates of area

[16]) K. O. Nielsen, O. B. Nielsen, and M. A. Waggoner, Nuclear Physics 2 (1956) 476.

[17]) K. O. Nielsen, Proc. Harwell Isotope Conf. (1955) Ch. 9.

A_t and A_b, respectively. The efficiency will thus be decreased by about a factor $A_p/(A_t + A_b)$. For $A_p = 0.1$ cm² and $A_t = A_b = 4.5$ cm² this factor is approximately 0.01, and the efficiency will be reduced from e.g. 10 to 0.1 %.

For radioactive rhenium, which was used in the form of Re_2O_7, we have found an efficiency of the order of 0.1 %[18]).

6.5. EFFICIENCY AT OPERATING CONDITIONS

Under usual operating conditions the pressure in the discharge chamber is slightly higher than p_{min}. If the pressure is too close to p_{min}, oscillations in the discharge can occur (hash). In addition, p_{min} varies with E_a and B, i.e. a small change in either E_a or B might cause the disappearance of the discharge, if the excess of admitted gas is too low. Therefore the efficiency at operating conditions, ηt, is 80 to 90 % of the efficiency determined at p_{min}.

To our experience the longer the discharge chamber, the lower is the excess of gas required for the maintenance of stable operating conditions.

7. Abnormal Ion Currents

In general, the ion source is operated under conditions where the resolving power has its highest value. If the power input to the filament is increased and at the same time E_l is adjusted to maximum RP, we get an increase in I_i and a decrease in RP, as shown in fig. 21. RP decreases quickly and a region with very strong oscillations in the ion current is reached. In this region RP is about zero and, instead of adjusting E_l to maximum RP, we adjust to maximum ion current to the collector. At still higher power input RP increases again until it reaches a maximum. Here again we adjust to maximum RP. This "higher state" is often disturbed by oscillations, but not as strongly as between the two stable states.

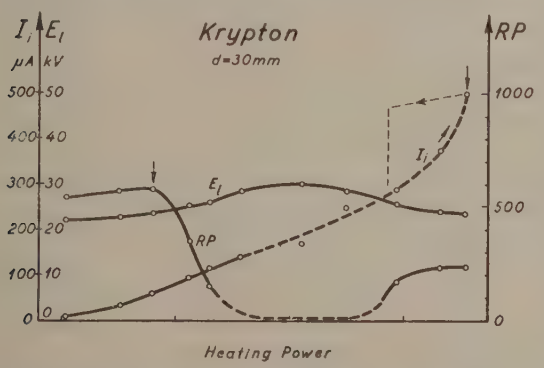

Fig. 21. Ion current, lens potential, and resolving power for krypton as functions of the heating power to the filament. ($E_h = 50$ kV, $d = 30$ mm and $A_o = 7.0$ mm².)

[18]) K. O. Nielsen and O. B. Nielsen, to be published (1957).

When decreasing the power input again, a hysteresis effect is observed in I_i (cf. fig. 23).

At the point where RP becomes zero, α is 0.53 instead of the normal value 0.47. When the higher state is approached, E_l decreases again and α is 0.47 at the stable state. It is worth noting that we get a non-zero value for RP only when α is smaller than 0.53. It thus seems that $\alpha = 0.53$ corresponds to a limit for proper operations of the lens system. In other words: $\alpha = 0.53$ corresponds to the largest angle of divergence of a beam which can be transmitted.

It is difficult to understand the behaviour of the ion source as described above. A possible explanation may be the following.

When the power input is increased, the ion production, and with it also n^+ in the plasma, is increased. This causes a decrease in A_p (cf. § 4.2). However, A_p cannot be less than the area of the opening A_o in the bottom plate. A further increase in n^+ must therefore give rise to a stable state with the plasma boundary outside the ion source, giving the ion beam in the acceleration gap such a shape that the ion current is higher than under normal operating conditions.

When A_p is near A_o it is not unlikely that the plasma boundary oscillates between the two stable states, one with the boundary inside and one with the boundary outside the ion source. This oscillation gives the region with RP ≈ 0.

The investigations described above show clearly that the strengths of the ion currents obtainable depend on the ion extracting device and on the lens system. If measurements are

made on an ion source alone, without requiring that the beam should have a divergence sufficiently small to be focused by the lens system, currents many times greater can be extracted from the source. Thus, our measurements are not characteristic of the ion source alone, but must be related to the isotope separator as a whole.

8. Further Experiments

Preliminary experiments were made with a discharge chamber in which the bottom plate was at the same potential as the anode. In such a discharge chamber the electrons from the filament are not oscillating. It is not surprising that the heating current to the filament is higher and that the anode current increases from 20 mA (cf. fig 12) to about 1 ampere. This type of discharge chamber is particularly useful when high temperatures are desired. In addition to the higher temperature we can expect a more uniform temperature distribution because the primary electrons strike the bottom plate which, in the case of oscillating electrons, is the coldest part of the discharge chamber. This advantage is achieved at the expense of the filament lifetime. It is our intention to investigate these factors in more detail.

In recent years another type of ion source has been constructed at Chalmers University of Technology in Gothenburg[19]). The discharge chamber in this ion source is very similar to that described above. However, here the ion extraction is perpendicular to the magnetic field. Preliminary investigations indicate that it has very similar characteristics to the discharge chamber in Copenhagen. Since both types are now available in Gothenburg, a comparison can be made on the same isotope separator.

Using the results of this investigation a final working model of the ion source has been constructed. The dimensions are chosen such that it is easy to place various types of discharge chambers in the magnetic field. The length of the discharge chamber can be varied from 50 mm – 120 mm. It is difficult, however, to obtain the highest temperature at the bottom plate while using the longest discharge chambers. Therefore, the diameter of the casing is chosen so that it is possible to place heating elements around the discharge chamber.

[19]) O. Almén and K. O. Nielsen, Proc. of Harwell Isotope Conf. (1955) Ch. 3.

Acknowledgements

The main part of this work has been performed at the Institute for Theoretical Physics, University of Copenhagen. We wish to thank Professor Niels Bohr for his continued interest in the experiments and for the good working facilities provided at the Institute.

We are also indebted to Professor J. Koch for placing the isotope separator at our disposal. In addition, we would like to thank Mr. K. Gudbjerg-Hansen for very valuable help during the construction of the various ion sources.

Furthermore, we express our gratitude to Professor J. Lindhard, Professor W. Walcher (Marburg), and Dr. M. Scharff for stimulating discussions.

One of us (O.A.) is indebted to Professor N. Ryde for his interest in our work, to Chalmers University of Technology for a grant (Adelskölds resestipendium), and to the Swedish Atomic Energy Comission for financial support during his stay in Copenhagen.

NUCLEAR INSTRUMENTS 1 (1957) 323; NORTH-HOLLAND PUBLISHING CO. – AMSTERDAM

NOTE ON THE PREPARATION OF ANHYDROUS RARE-EARTH CHLORIDES FOR THE ELECTROMAGNETIC ISOTOPE SEPARATOR

BROR SKYTTE JENSEN †

Institute for Theoretical Physics, University of Copenhagen, Denmark

Received 10 July 1957

A quick and simple procedure for preparing anhydrous rare-earth chlorides in amounts ranging from 50 to 300 mg is desirable for use in charging the isotope separator.

The method chosen is an adaptation of the well-known ammonium chloride method.

The procedure to be described has been used successfully for the preparation of the anhydrous chlorides of Gd, Dy, Er, Yb, and Lu. We estimate the yield of the transformation of the oxides into the chlorides to be 70-90% depending on circumstances.

Procedure

The weighed amount of the rare-earth oxide (50–200 mg) is placed in a small porcelain crucible (1–2 ml) and dissolved in strong hydrochloric acid under an infra-red lamp. The process of solution can be speeded up, if necessary, by pipetting a small amount of hydrogen peroxide (30%) into the mixture. If crystals of the hydrated rare-earth chlorides precipitate, water is added and evaporation allowed to proceed until the crucible is about half filled with a clear solution. Ammonium chloride powder is then added so that the crucible becomes filled with a paste which is formed when the solution is absorbed into the crystalline powder. Heating is continued under the infra-red lamp until the paste is sufficiently dry to allow easy manipulation of the crucible in subsequent steps of the procedure.

A Pyrex test tube ¼ filled with dry NH_4Cl is held in a horizontal position. The crucible is then slid into the test tube in an upright position and a certain amount of ammonium chloride is added to serve as support for it.

By carefully heating the layer of NH_4Cl, which is at the closed end of the test tube, with a Bunsen burner, it is possible to evaporate the last traces of water from the mixture in the crucible in an ammonia-hydrogen chloride atmosphere without serious boiling the contents of the crucible. When all the water is driven off, the temperature is increased, whereupon the NH_4Cl sublimes out of the test tube. Care must be taken to ensure that no water drops stay inside the test tube by flaming the upper part of the glass occasionally.

When all the ammonium chloride outside the crucible has been driven to the cold half of the test tube or out of it, the contents of the crucible begin to melt. This first melt shows signs of boiling as the last traces of NH_4Cl are driven off and may or may not solidify again, depending on the melting point of the anhydrous chloride involved. A rubber stopper is placed in the opening of the tube, the flame removed, and the whole assembly is allowed to cool.

When cold it is often necessary to break the test tube to remove the crucible because the glass and the porcelain usually sinter together.

If melted, the chlorides show a crystalline structure and can adhere strongly to the crucible. If not melted, they are less dense and can easily be scraped off.

The anhydrous chlorides can be tested by dissolving a small sample in water. Even an insignificant amount of oxychloride will give the water a milky appearance. (This was normally seen, but no precipitation in appreciable amounts has ever been observed.)

† On leave from "Atomenergikommissionens Forsøgsanlæg Risø", Denmark.

NUCLEAR INSTRUMENTS 1 (1957) 324–328; NORTH-HOLLAND PUBLISHING CO. – AMSTERDAM

ENERGY CONTROL OF A 31 MeV BETATRON

D. JAMNIK

Institute "J. Stefan", Ljubljana, Yugoslavia

Received 19 June 1957

The article describes circuitry for the energy control of the 31 MeV Brown-Boveri type betatron and gives the results of the energy calibration. Except supplementary circuits required for the above type betatrons, the common technique is used: the electron orbit is expanded at a given value of the magnetic flux, defining the electron energy. A better measuring of the flux is achieved by the use of an electronic voltage integrator. The arrangement enables a stabilization of about ± 5 keV at 17 MeV for rather wide fluctuations of the magnet supply frequency and voltage.

The energy calibration performed with thresholds and breaks in the excitation curves for (γ,n) reactions in copper, oxygen and carbon shows excellent linearity of the relationship between the measured flux and the maximum energy of the X-ray spectrum. The positions of the breaks in the excitation curves found in this work agree very well with the published results.

1. Introduction

The experiments in measuring the fine structure of photonuclear reaction yield curves require a precisely defined maximum energy of the bremsstrahlspectrum of bombarding photons. For reliable results the stability of this energy should sometimes be better than ± 10 keV. This problem has been successfully solved for Allis-Chalmers betatrons in several places[1,2,3,4]). In our institute we tried to develop a corresponding energy control for the Brown-Boveri betatron which is connected directly to a rather unstable mains. Therefore the energy control has to be effective over a wide interval of magnet amplitude fluctuations. The description of our work may be of interest since there are several betatrons of the same type running in Europe now.

In general, we applied the usual method for betatron energy control. This method consists in expanding the electron orbit at a given value of the magnetic flux which is a measure of the electron energy. The flux is measured by integration of a corresponding voltage which is taken from the excitation coil or from a coil placed at the stable electron orbit. The latter method is preferable since the integrated voltage in this case corresponds much closer to the energy defining flux. The moment of expansion is determined by the setting of a discriminator to which the output of the integrator is fed. The discriminator in connection with a pulse generator produces at the chosen value of the flux a pulse for triggering the expansion circuit.

The flux-representing voltage should be about 100 V_{eff} or more so that the discrimination can be precise enough. On the other hand, for effective stabilization over a wide interval of magnet amplitude fluctuations, the integration should be almost perfect. Otherwise, an error is introduced in the measuring of the flux depending on these fluctuations. For this reason the often used simple RC integration can only be applied when the fluctuations of the mains are small[3,5]). In our case we have to use an electronic integrator which enables very good integration without reducing the voltage.

The X-ray pulse appears with some delay after the triggering of the expansion. The energy gain during this delay depends both upon the length of the delay and the magnet amplitude. This is especially serious for Brown—Boveri betatrons

[1]) Sherr *et al.*, Phys. Rev. **84** (1951) 387.

[2]) Katz *et al.*, Can J. Res. A **28** (1950) 113.

[3]) B. M. Spicer and A. S. Penfold, Rev. Sci. Instr. **26** (1955) 952.

[4]) E. C. B. Pederson and L. Katz, Bull. Am. Phys. Soc. Vol. **30** No. 4 (1955) 8.

[5]) M. Birnbaum, Phys. Rev. **93** (1954) 146.

where the delay amounts to more than 50 μs. Here also the X-ray pulse is relatively long, about 10 μs, the shape and duration being very dependent on the injection conditions.

To avoid these difficulties one has to use a much faster expansion. However with a Brown-Boveri betatron it would be difficult to make a fast enough expansion in a single step since the electron orbit has to be expanded for 15–20 mm. We made therefore the expansion in two steps†: the original slow expansion expands the electron orbit as before but when it nearly reaches the target, an additional fast expansion is fired, destroying the electron beam on the target practically without delay. The energy gain after the firing of the fast expansion is therefore negligible; the X-ray pulse duration is also short, about 1–2 μs.

Neglecting oscillations, the radial velocity of the electrons is very small compared to the axial velocity during the slow expansion. The slow expansion can be considered as a quasistationary process where the total (kinetic + rest) electron energy in the relativistic region is equal to

$$\frac{ec}{2\pi R}\,\Phi\,(R,t),$$

R is the radius of the electron orbit at the time t and $\Phi(R,t)$ the corresponding magnetic flux. The exact expression includes still terms of the order of the ratio of the radial to the axial velocity. These terms can be neglected in our case.

Considering the above formula one should destroy the electron beam on the target at a given value of Φ and R. However, since the flux-condition is practically satisfied, it is sufficient to trigger the fast expansion at a given value of the magnetic flux measured with a fixed coil at the radius of the target. The relative error in the energy is in this case of the order of $\pm\ 10^{-4}$ if the error in R is $\pm$ 2 mm (10% of the distance from the stable orbit to the target).

The oscillations, which we neglected, are quite appreciable still at the end of acceleration: the X-ray pulse duration is not short compared to the time of expansion. Although we did not study the effect in detail, we expect that the influence of oscillations on the energy is not significant.

The design of the stabilization circuitry is now quite straightforward and we describe it in the next section. The last section deals with the energy calibration and performance of the arrangement.

2. Circuitry

2.1. FLUX-MEASURING SYSTEM

The signal voltage of about 140 V_{eff}, 50 cps is taken from a coil with the radius of the target (two turns above and two below the doughnut). This voltage is fed to the integrator (fig. 1), which gives on the output the fluxrepresenting voltage of 120 V_{eff}. The integrator consists of a three stage amplifier and the corresponding RC feedback. The amplifier gain is about 10^4 at 50 cps and 300 at 1500 cps. The gain at the higher frequency must be still sufficient to measure the additional flux of the slow expansion which

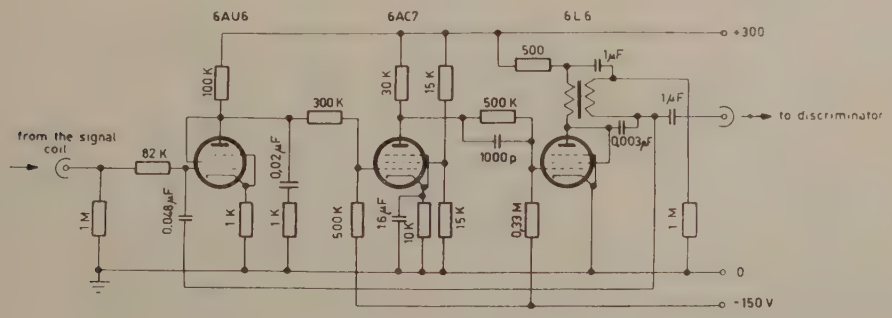

Fig. 1. Integrator. The grid resistor of the 6AC7 tube is 1.2 MΩ instead of 500 kΩ.

† This has been suggested to us by A. v. Arx, BBC.

consists of a half-sine wave pulse of 400 μs duration and an amplitude of the order of 2% of the total flux. Direct coupling between the stages in the amplifier prevents dangerous phaseshifts at low frequencies. To avoid high anode supply voltage we use a transformer output stage. Here the low frequency phaseshifts are reduced by connecting the transformer secondary through the 1 μF condenser to the 500 ohm series resistor. The circuit has been designed to be safe also against high frequency oscillations The RC feedback consists of a manganin wire resistor and a metalized-mica condenser. There is no dc-load on this condenser. Except for heaters, the voltage supplies are stabilized

It is expected that the circuit integrates with a precision of $1:10^4$. The rapid drifts which appear on the output amount to 10^{-2} V.

2.2. DISCRIMINATOR AND EXPANSION SYSTEM

The output of the integrator is connected through a condenser to a discriminator consisting of a biased cathode follower and a multiar-type circuit. The time of the expansion is determined by the bias voltage of the cathode follower. We use two discriminators, one for the slow and the other for the fast expansion. In the discriminator for the slow expansion an additional separately adjustable positive bias is applied, since this discriminator must open about 80 μs before the other one. This time interval must be adjusted properly so that the fast expansion fires at the right moment when the electron beam is already very near to the target. The adjustment is done in connection with the observation of the X-ray pulse on an oscilloscope. However readjustments are only necessary when the energy is changed by large amounts. It is important that the cathode followers have a sufficiently low grid current during the operation.

Both cathode followers have a common bias voltage which is taken from a precision-potentiometer connected to a stabilized —230 V voltage supply. The stability of this supply is of the order of $\pm$ 0.01% per hour and is controlled by a standard cell.

The multiar-type circuits[6]) respond to positive signals. The zero point is very stable, sharp ($\pm$ 10^{-2} V) and easily controlable since the circuits at zero diode bias begin to exhibit self-oscillations. For diodes, both types EA50 as 12AL5 have been used successfully. To suppress the afterpulses from the multiar, in the anode of the following 6SN7 tube which triggers the 2050 thyratron, a proper RC time constant is used. The other half of 6SN7 with the neon lamp indicates the running of the multiar (zero-point control).

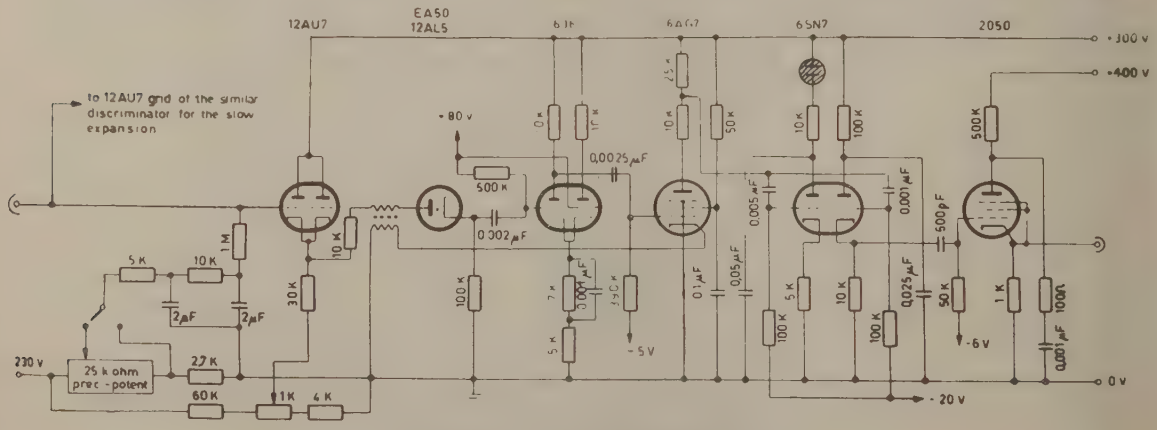

Fig. 2. Discriminator with the trigger stage.

2050 thyrathrons trigger the expansion circuits. The slow one is commercial from Brown-

[6]) Waveforms, RLS 19 (Mc Graw Hill) 343.

Boveri, the fast one consists of a 5C22 hydrogen thyratron and a 0.1 μF condenser which is discharged through a 4:1 pulse transformer with the fast expansion coil on the secondary. Since there is not much place in the gap between the doughnut and the magnet poles for the insulation of the fast expansion coil the use of this transformer is necessary in our case. In this coil a halfsine wave pulse of 15 μs duration is produced. For a 1.5 μs long X-ray pulse at 20 MeV about 350 A peak are needed. The charging of the 0.1 μf condenser is resonant over a 100 H choke.

All the dc-voltages for the discriminators are stabilized. Stabilized heater voltage is necessary both for the cathode follower tube and for the diode in the discriminator for the fast expansion.

3. Energy Calibration and Performance

We calibrated our energy scale with known thresholds and breaks in the excitation curves of $Cu^{63}(\gamma,n)Cu^{62}$, $O^{16}(\gamma,n)O^{15}$ and $C^{12}(\gamma,n)C^{11}$ reactions. Following the usual procedure we irradiated cylindrical samples with the monitored X-ray beam at 20 cm from the target and counted the activity induced in the samples. The results are given on figs. 3, 4, 5.

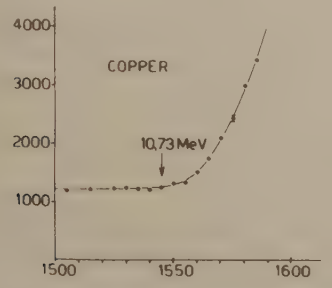

Fig. 3. Number of counts *vs.* potentiometer-setting for the $Cu^{63}(\gamma,n)$ reaction.

For the copper threshold, the value of 10.73 MeV[7]) has been used. In oxygen (B_2O_3 samples) we took for the energy calibration the pronounced break at 16.03 MeV, measured carefully by Spicer and Penfold[7]). We did not follow the excitation curve to lower energies. Upwards,

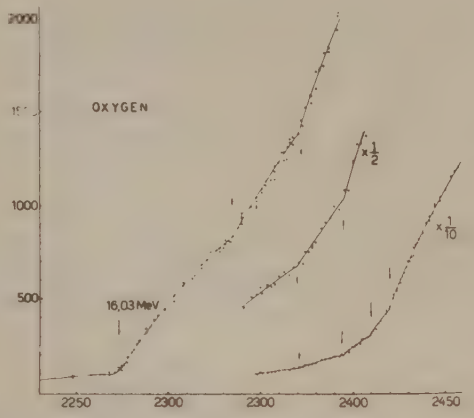

Fig. 4. Number of counts *vs.* potentiometer-setting for the $O^{16}(\gamma,n)$ reaction. The three curves represent three independent measurements

where we measured up to 17.3 MeV the positions of the breaks agree very well with those of Spicer and Penfold. This is seen on the table 1.

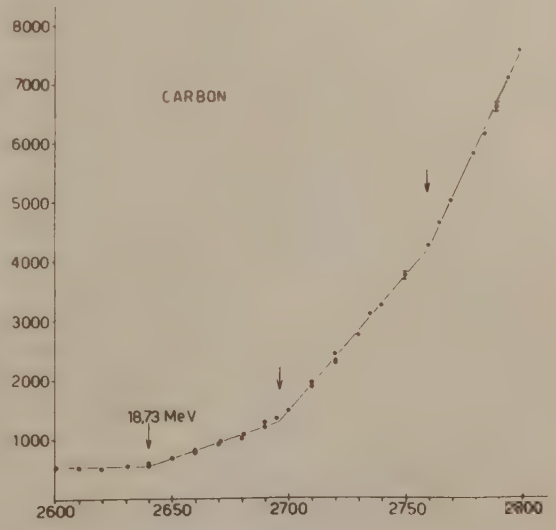

Fig. 5. Number of counts *vs.* potentiometer-setting for the $C^{12}(\gamma,n)$ reaction.

The carbon threshold was measured with graphite cylinders irradiated for 20 minutes. Since we had appreciable background from the

[7]) B. M. Spicer and A. S. Penfold, Phys. Rev. **100** (1955) 1377.

TABLE 1

oxygen	
pres. results	Spicer and Penfold
16.03 MeV	16.03 MeV
16.48	16.47
16.75	16.75
16.92	16.95
17.03	17.02
17.11	17.15
carbon	
18.73	18.73
19.14	19.10
19.60	19.55

Positions of breaks in $O^{16}(\gamma,n)$ and $C^{12}(\gamma,n)$ yield curve found in the present work compared with those observed by Spicer and Penfold. In the present determination the error in the relative position of the breaks may be 20 keV for oxygen and 40 keV for carbon. Spicer and Penfold give a corresponding error of 15 keV for oxygen and 50 keV for carbon.

nitrogen activity we began with counting 10 minutes after irradiation. The investigated region included the first two breaks and the results are again in good agreement with those of Spicer and Penfold[8]), (table 1).

We believe that the determination of the thresholds and breaks is accurate to $\pm$ 40 keV or better. To this accuracy the results, plotted on the energy *vs.* potentiometer-setting diagram show excellent linearity as expected from the dependence of the total electron energy in the relativistic range on the magnetic flux. At potentiometer-setting zero the disagreement is of the order of 100 keV when the correction of about 100 keV arising from the phaseshift in the RC coupling between the integrator and discriminator is taken into account. An error of 280 keV in the determination of the carbon threshold as should be done before[8]), would result in a pronounced deflection from the linearity.

It may be worthwhile to note that the breaks are found at the same energies with the Brown-Boveri type betatron as with the Allis-Chalmers types. This may be considered as an additional argument in favour of the reality of the breaks.

The stabilization of the arrangement against mains fluctuations is very good. We measured the stability with oxygen activity at 17.2 MeV under usual conditions of our mains, where frequency varies from 48 to 50.5 cps and voltage for $\pm$ 3%. The stability observed was about 5 keV or better. In the interval of some hours of operation a fluctuating drift of about $\pm$ 8 keV has been observed. The source of this drift could not be found in the electronics.

The arrangement has been very reliable in operation since summer 1956, when the above energy calibration was performed. In the beginning we had some difficulties to find a good enough integrating condenser. Since that time, we often controlled the 16.03 MeV break in oxygen activation and could always reproduce the previous determination.

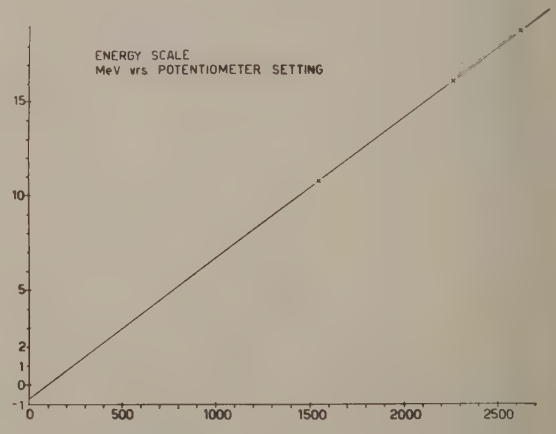

Fig. 6. Betatron energy scale with the measured calibration points at 10.73 MeV, 16.03 MeV and 18.73 MeV. One potentiometer-setting unit corresponds to 7.32 keV.

Acknowledgement

We thank professor Peterlin for encouragements as well as Mr. A. v. Arx from the Brown-Boveri Co. Baden and Dr. Č. Zupančič for helpful suggestions and discussions. Thanks are due to Mr. M. Vakselj and Z. Milavc for the aid in performing the measurements.

[8]) B. M. Spicer and A. S. Penfold, Phys. Rev. **100** (1955) 1375.

NUCLEAR INSTRUMENTS 1 (1957) 329–330; NORTH-HOLLAND PUBLISHING CO. – AMSTERDAM

RADIATION INSTABILITY IN NUCLEAR MAGNETIC RESONANCE EXPERIMENTS

K. V. VLADIMIRSKY

P. N. Lebedev Institute of Physics of the Academy of Sciences of USSR, Moscow

Received 31 May 1957

In nuclear magnetic resonance experiments the substance to be investigated is being placed in the coil of a radiofrequency tuned resonant circuit. An analysis of the oscillatory system formed by the sample with precessing nuclear magnetization and the resonant circuit shows that the changes in the radiofrequency field of the coil due to the reaction of the sample on the resonant circuit must not be neglected in definite cases.

It was shown[1, 2, 3]), that this leads to an enhancement of the damping of the nuclear magnetization free precession and to the broadening of the signals observed in stationary conditions.

In the present note the stability of the sample-resonant circuit system is considered. The properties of the sample are specified by Bloch macroscopic equations[4]). It is assumed that the r-f field acting on the specimen is created by the e.m.f. induced by the specimen only. i.e., that the circuit is not connected with an external generator. The resonant circuit is tuned to a frequency near to that of the nuclear magnetization free precession, the band width of the resonant circuit is large as compared with the n.m.r. line width.

Under these assumptions we have the following system of differential equations:

$$\begin{aligned}
&\dot{M}_x - \gamma H_0 M_y + \frac{1}{T_2} M_x = 0,\\
&\dot{M}_y + \gamma H_0 M_x - \gamma H_x M_z + \frac{1}{T_2} M_y = 0,\\
&\dot{M}_z + \gamma H_x M_y + \frac{1}{T_1} M_z = \frac{1}{T_1} M_0,\\
&H_x = -(4\pi\eta Q/|\gamma| H_0)\dot{M}_x,
\end{aligned} \tag{1}$$

where η is a filling factor, near to unity if the coil is completely filled with the working substance, Q is a figure of merit of the resonant circuit.

Let be

$$M_x = M_y = H_x = 0, \quad M_z \neq M_0$$

at some initial moment. The system (1) possesses an obvious solution

$$M_x = M_y = H_x = 0, \quad M_{z0} = M_0 + A\exp(-t/T_1), \tag{2}$$

where A is a constant. For the investigation of the stability let us consider the system of the equations determining the development of small deviations from the solution (2):

$$\begin{aligned}
&\dot{M}_x - \gamma H_0 M_y + \frac{1}{T_2} M_x = 0,\\
&\dot{M}_y + \gamma H_0 M_x - \gamma H_x M_{z0} + \frac{1}{T_2} M_y = 0,\\
&\dot{M}'_z + \frac{1}{T_1} M'_z = 0,\\
&H_x = -(4\pi\eta Q/|\gamma| H_0)\dot{M}_x,
\end{aligned} \tag{3}$$

where

$$M'_z = M_z - M_{z0} \ .$$

In this system the terms of the highest order of smallness are omitted.

For the time dependence of M_x we obtain the equation

$$\ddot{M}_x + \left(4\pi M_{z0}|\gamma|\eta Q + \frac{2}{T_2}\right)\dot{M}_x + \left(\gamma^2 H_0^2 + \frac{1}{T_2^2}\right)M_x = 0. \tag{4}$$

By separating the oscillatory multiplicand in the solution of the equation (4), it may be shown that M_x, M_y, H_x grow up exponentially if the condition

$$-2\pi M_{z0}|\gamma|\eta Q \gtrsim \frac{1}{T_2} \tag{5}$$

is satisfied.

Contrary to a suggestion in the literature[2]), the state with nuclear magnetization oriented against the field is not radiationless, if the condition (5) is satisfied. Instead of pure relaxation self-exitation will be observed accompanied by an accelerated approach of the nuclear magnetization to the equilibrium state and by the conversion of a part of the magnetic energy into the energy of the r-f oscillations. Numerical estimations analogous to that given in[2]) show, that self-exitation condition (5) may be satisfied, for example, in experiments with water at accessible field strength H_0.

The developed self-exitation process at

$$2\pi \mid M \mid \mid \gamma \mid \eta Q \gg 1/T_2$$

is described by the equation

$$\frac{\mathrm{d}\theta}{\mathrm{d}t} = -2\pi \mid M \mid \mid \lambda \mid \eta Q \sin \delta,$$

where

$$\theta = \arccos (M_z/\mid M \mid).$$

The solution

$$\mathrm{tg}\,\theta/2 = \exp (-2\pi \mid M \mid \mid \gamma \mid \eta Q t)$$

was used in[2]) for the description of the radiation damping. This same solution at $t < 0$ permits to follow the self-exitation process, accompanied by the appearance of the induction signal in the resonant circuit with the amplitude proportional to sech $(2\pi \mid M \mid \mid \gamma \mid \eta Q t)$.

The sample-resonant circuit system under condition of self-exitation or near to it may be used as a nuclear magnetic oscillator and amplifier. The nuclear magnetization fluctuations being small, one can expect to obtain in this way a noise figure near to unity.

The development of continuously acting apparatus of this type is possible by means of the continuous change of the working substance.

[1]) G. Suryan, Current Sci. (India) **18** (1949) 203.
[2]) N. Bloembergen and R. V. Pound, Phys. Rev. **95** (1954) 8.
[3]) C. R. Bruce, R. E. Norberg and G. E. Pake, Phys. Rev. **104** (1956) 419.
[4]) F. Bloch, Phys. Rev. **70** (1946) 460.

NUCLEAR INSTRUMENTS 1 (1957) 331–334; NORTH-HOLLAND PUBLISHING CO. – AMSTERDAM

A FAST COINCIDENCE CIRCUIT

D. H. WHITE and G. W. HUTCHINSON

Department of Physics, University of Birmingham

Received 18 July 1957

A coincidence circuit is described with an improved rejection ratio to non coincident pulses. In the coincident condition, information is gathered during a large part of the time of overlap of the applied signals, not merely from the coincidence of the leading edges. The resolving time is comparable with that obtained using conventional circuits.

1. Introduction

The requirements for a coincidence circuit have been summarised by Strauch[1]) and by Lewis and Wells[2]). The characteristics that are generally used to specify the performance of a coincidence circuit are the resolving time and the rejection ratio. The resolving time may be defined conveniently as the maximum delay that may exist between the signals at the various inputs when the event is still counted. The rejection ratio is the ratio of the pulse height at the output of the circuit for an exact coincidence, that is when the input signals arrive simultaneously, to the pulse height in the non coincident situation where the delay between signals is long compared with the resolving time.

Normally the method of obtaining a discrimination for the coincidence condition involves shaping the input signals (clipping) so that only a small portion of this signal is used in the coincidence action when a short resolving time is required. In the circuit described in this paper, the pulses are mixed and shaped so that information may be gathered during a large proportion of the overlap in time of the whole input signals. By using this method, the pulse height corresponding to the coincidence state is enhanced over the non coincident condition. The system is useful in the case where the resolving time is considerably less than the total duration of the input signals, this being the usual condition in circuits used with nuclear detectors. With the present circuit, R.C.A. 6810 photomultipliers and "Pamelon" phosphors, a resolving time of 5×10^{-9} sec is obtained with a duration of 50×10^{-9} sec in the detector signal.

Series diodes in each input channel are connected to form the terminating impedance of a shorted line S (fig. 1). These diodes are normally conducting and are cut off by the incoming signals. When they are all cut off, the impedance at the junction is high so that a series of reflections is possible. Since current is present in the line in the quiescent state, the arrival of the overlapping signals produces a ringing waveform on the line. The amplitude of this waveform is dependent on the relative delays of the incoming signals. The resolving time thus depends upon the fundamental frequency of the ringing waveform, while information is taken during the whole duration of the ring.

2. Circuit Design

A circuit diagram is shown in fig. 1. Each input channel consists of a silicon series diode (CV 253), with its current i_0 stabilised by the resistor R to the positive 250 volt supply. The negative ends of the diodes and a shorted line meet at J, referred to as the junction. Suppose the characteristic impedance of the line be Z_0, and the forward impedance of the diode in the quiescent state be Z_f. A signal in any channel is applied from a line of characteristic impedance Z_0. The

[1]) K. Strauch, Rev. Sci. Inst. **24** (1953) 283.

[2]) I. A. D. Lewis and F. H. Wells, Millimicrosecond Pulse Techniques (Pergamon Press, 1954).

diode current is cut off and a signal passes along the shorted line S returning with opposite polarity to the junction.

If n_t is the total number of channels, and of these n_p receive a signal at time t_0, then the magnitude of the signal passing along the line S is approximately

$$\frac{i_0\, n_p\, (Z_t + Z_0)}{Z_t + Z_0\, (1 + n_t - n_p)}$$

when the resistance of the diodes in the non conducting state is high compared to Z_0.

current is 5 mA. In the case of an exact coincidence $n_p = n_t$. Then $i_N = n_t\, i_0\, (-1)^N$. This corresponds to the generation of a symmetrical square waveform at the point J. This waveform is in fact damped to about six oscillations because of the attenuation of the line S and the finite resistance of the diodes when cut off. (fig. 3a). In the situation where $n_t - n_p = 1$, $R = Z_f/(Z_f + 2Z_0) = 0.29$. In this case the waveform is heavily damped, (fig. 3b) with a small positive overshoot. The ratio of the first

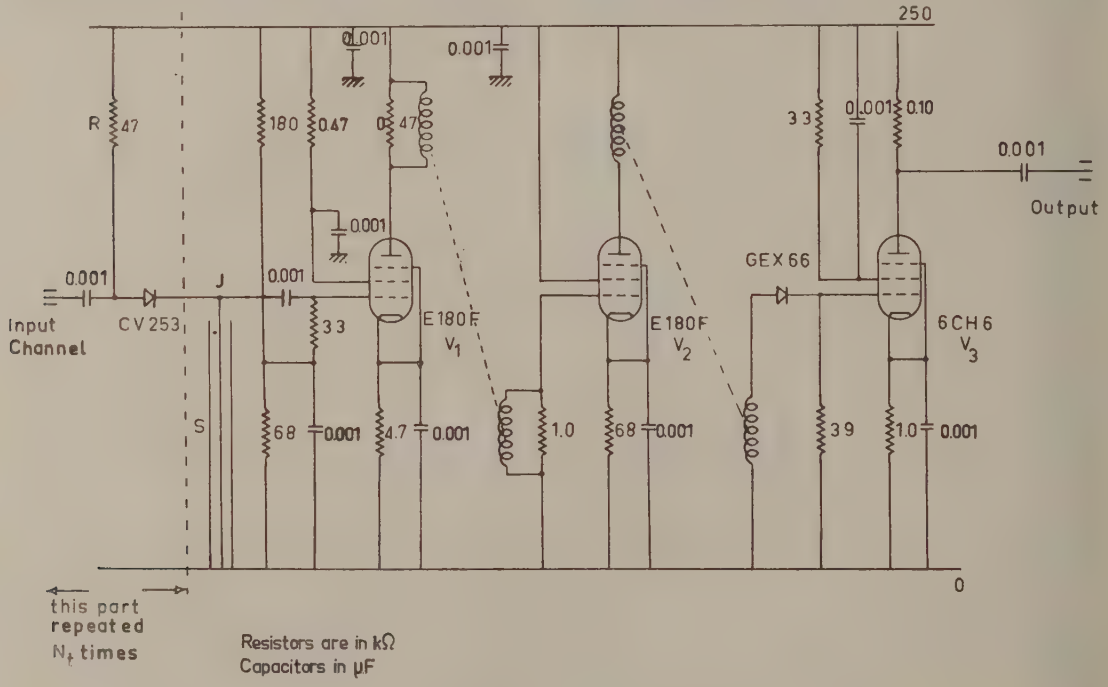

Fig. 1. Circuit diagram.

The signal is reflected at the shorted end of the delay line without loss of magnitude and at the junction J with a reflection coefficient R given by

$$R = \frac{Z_t + Z_0\, (1 - n_t + n_p)}{Z_t + Z_0\, (1 + n_t - n_p)} .$$

After N reflections the magnitude of the signal on the line is

$$i_N = (-1)^N\, R^N\, \frac{n_p\, i_0\, (Z_t + Z_0)}{Z_t + Z_0\, (1 + n_t - n_p)} .$$

With the diodes that were used in the circuit, Z_f is approximately 80 ohm when the forward

positive excursion in the two cases is

$$\frac{n_t - 1}{n_t}\, \frac{Z_t\, (Z_t + Z_0)}{(Z_t + 2Z_0)}$$

for a three channel circuit ($n_t = 3$). For the values $Z_f = 80$ ohm, $Z_0 = 100$ ohm when $n_t - n_p \geqslant 2$, R is negative and no positive excursion occurs. In fig. 2c this condition is shown ($n_t = 3$, $n_p = 1$), followed by a double coincident signal ($n_p = 2$). In this case the situation for continuous reflection is present, but only two signals can contribute to linear addition at the junction. The waveform is thus two thirds

of the normal amplitude. The photographs have been taken with pulses 1 microsecond long and of 7×10^{-9} sec rise time. With a shorter length of pulse, the ringing action in the partially coincident case is restricted in time to the remaining length of the first pulse. The length of the clipping line $\tau = 2.5 \times 10^{-9}$ sec.

In designing a discriminator for this coincidence network, three of the properties of the coincidence waveform were used. (i) In the non coincident waveform, the signal is almost entirely negative. (ii) The amplitude of the coincident waveform is greater, owing to linear addition at the junction. (iii) The relative frequency spectra of the coincident and non coincident waveforms are different, there being a large component of frequency $f = 1/2\tau$ in the coincident waveform.

The discriminator consists of a tuned amplifier and driver stage. The first valve V_1 (Mullard type E180F) is used linearly and aperiodically to drive a similar pentode through an inverting transformer. V_2 is run non linearly by using a low standing current in order to reject the negative excursions in the wave form. The coupling transformer between V_2 and V_3 is tuned to the fundamental frequency of the coincident waveform $f = 1/2\tau$. The bandwidth of this amplifier is arranged to make the relaxation time longer than the waveform shown in fig. 3a, and to provide an output pulse of suitable length to drive a following discriminating and scaling channel. The diode GEX66 is inserted to rectify the amplified waveform at the grid of V_3.

Performance

The circuit has been tested both with a pulse generator and with photomultiplier signals. The size of the current pulse needed for satisfactory operation of the circuit must be large enough to keep the input diodes in the conducting state during the duration of the ringing waveform. In the circuit used, in which $n_t = 220$ mA was necessary; rather more than three times the standing current in one diode.

Fig. 2 shows the waveforms obtained with the pulse generator. They would not be expected to contain any appreciable harmonics of the fundamental frequency because of the limitation of bandwidth in the oscilloscope and pulse generator.

Fig. 2. Trace
1. Waveform at the junction J.
2.
3. Waveform at the input channel.
4.

In the case of uniform input pulse size, the shape of the delay curve obtained by plotting counting rate against delay in an input channel, the others being coincident, will be almost ideally square so long as the bias level of the discriminator is set high enough to reject counts of the type illustrated in fig. 2c. The height of the output signal produced by counts of this type depends on the phase difference of the signals produced in the delay line S. When there is a phase difference of 2τ, at the fundamental frequency of the line, the output signal has a maximum amplitude. The subsidiary peaks appear in the delay curve for lower bias settings, their spacing on either side of the main peak being equivalent to four the length of the delay line S.

If pulses from photomultipliers were standardised in amplitude by passing them through limiters before presenting them to the coincidence circuit, the bias level would normally be set to reject all but completely coincident sets of pulses, so that a single-peaked delay curve would be obtained. However, the high rejection ratio between cases 2a and 2b makes it possible to use the circuit without limiters even when a considerable spread of pulse heights is presented to it from the photomultipliers. The bias level has be set lower to make full use of this rejection ratio under these circumstances. If this causes the subsidiary peaks to occur in the delay curve, the rejection of random coincidences by the circuit is impaired rather as though the resolving

time of the circuit had been increased by a factor lying between one and three.

To test the circuit under these conditions three scintillation counters were set up near the Birmingham 980 MeV proton synchrotron and aligned so that the high energy protons traversed the three counters. Coincident signals from the three counters then had sufficient height to operate the coincidence circuit. The height spectrum of the pulses from one photomultiplier is shown in fig. 3. The coincident counts were

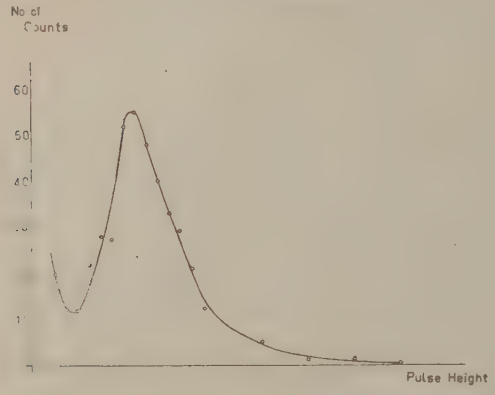

Fig. 3. Pulse height spectrum at one input channel.

expected to have a smaller amplitude than the background counts. The spectrum peak was believed to be due to protons of the maximum energy and the pulses of greater height to be due to the background of more heavily ionising radiation. The highest pulses were above the turn-over voltage of the CV 253 diodes but the frequency selection mechanism of the coincidence discriminator evidently rejected these.

After the optimum delay in each channel had been found for coincident counting, delay curves, shown in fig. 4, were taken for two settings of the discriminator bias in the scaling circuit following the output of the circuit. They show that, under these conditions bias settings can be found either to give a high efficiency for counting coincident pulses together with an almost complete rejection of events separated in time by more than 6τ, or to reject events separated by a time of the order of 2τ but with reduced efficiency for coincident events.

The advantages of the circuit are marginal when double coincidences only are needed, but become much more important as the multiplicity of the inputs increases.

The initial design of the pulse shaping circuit was due to Dr. E. C. Park. We acknowledge with thanks his contributions and encouragements in the early stages of the work.

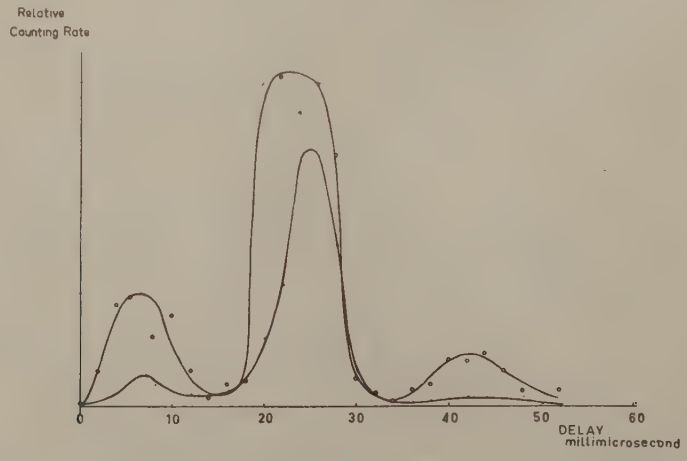

Fig. 4. Delay curve. Relative delay of one counter.

NUCLEAR INSTRUMENTS 1 (1957) 335–339; NORTH-HOLLAND PUBLISHING CO. – AMSTERDAM

GRAPHITE SPHERE NEUTRON DETECTOR

R. L. MACKLIN

Oak Ridge National Laboratory, Oak Ridge, Tennessee

Received 10 August 1957

A five foot graphite sphere has been constructed for neutron source intensity measurements, particularly for use in the kilovolt energy region. The measured efficiency using eight $B^{10}F_3$ detectors near the surface is about 0.03 at 25 keV. The change in efficiency from 1 keV to 2 MeV is calculated to lie within $\pm$ 1%. An absolute calibration of a (NBS) standardized Sb Be neutron source was performed by measuring the exit current of thermal neutrons with a thin wafer of Li^6I(Eu) scintillator. The half life of Sb^{124} was also remeasured as 60.4 $\pm$ 0.2 days.

1. Introduction

The need for a constant efficiency neutron detector has been met for many years by the well known paraffin jacketed, BF_3, "long counter" of Hanson and McKibben[1]. Its response as a function of energy, distance from a source etc. has been re-investigated recently at Harwell[2].

The use of neutron scattering by hydrogen has provided a more accurate standard counter (above 100 keV or so), but as the intercomparisons show, with proper attention to the energy dependence of the effective center and the efficiency, a long counter may be relied upon to perhaps a few percent. At lower energies than a few tens of kilovolts, however, the characteristics of the long counter have not been investigated in detail. The prescriptions for boring extra holes in the paraffin to improve the low energy response empirically (by testing with 24 keV Sb–Be neutrons) point up the need for further testing in this energy region. The energy dependence of the in-scattering by nitrogen is another factor that may often become important in this region, as long counters are often used at appreciable distances (1–2 metres) from a neutron source, in air.

A fundamentally similar, but more exhaustive approach to flat response neutron counting is typified by the manganese bath technique. In this method, ideally, the neutrons are introduced at the center and the detector is made so large that there is negligible neutron escape. Nearly all the neutrons are captured after thermalization in a nucleus producing convenient radioactivity, which last then provides an energy insensitive measure of the neutron source strength. An intermediate approach has been used occasionally. Walker[3] has used a large graphite block with BF_3 counters as a flat response neutron detector in cross section measurements, calculating the energy dependence from reactor theories. More recently, several Russian investigations[4] with graphite-BF_3 detectors based on similar principles have been reported. The graphite-BF_3 counter described in this paper was designed particularly for use with neutrons with energies from a few keV to a few MeV, originating in charged particle reactions.

2. Design and Construction

The neutron detection system to be described was designed by age-diffusion theory calculations. Accordingly the material (reactor grade

[1]) A. O. Hanson and J. L. McKibben, Phys. Rev. **72** (1947) 673.

[2]) W. D. Allen, Report A.E.R.E. NP/R 1667 (Harwell, June 8, 1955).

[3]) R. L. Walker, Phys. Rev. **76** (1949) 244.

[4]) Proceedings of the International Conference on Peaceful Uses of Atomic Energy—Geneva (1955).

graphite[5])) and shape (sphere) were chosen for maximum applicability of that theory. In principle, high energy neutrons may be introduced either at the center or the surface of the sphere and the thermal flux produced by collisions measured at the surface or center respectively. The energy dependence is the same in either case. However, to avoid energy dependent corrections for air scattered neutrons, we have chosen to operate the system with the fast neutron source always at the center of the sphere. The applicable formula[6]) for the thermal neutron leakage J across the surface is then

$$J(a) = 2S \sum_{m=1}^{\infty} \frac{(-1)^{m+1} m^2\pi^2}{m^2\pi^2 + (a^2/L^2)} \cdot \exp\left(-m^2\pi^2\theta_0/a^2\right) \quad (1)$$

where S is the rate of fast neutron emission from the source, a is the radius of the sphere with the usual extrapolated boundary addition, L is the thermal neutron diffusion length and θ_0 is the Fermi age from the initial neutron energy to thermal energies.

Qualitatively, one has a competition for the neutrons among fast leakage, thermal leakage and thermal capture. For energies from several kilovolts to a few MeV and for high purity graphite optimum radii (60 to 80 cm) can be found which maximize the thermal leakage at 70 to 80 %. In this range, a fixed radius leads to compensatory energy dependence of the fast leakage and thermal capture, so that the ratio of thermal leakage to source strength is only a very slowly varying function of initial energy.

Only for an absolute source strength determination is a careful measurement of the thermal leakage made. As a neutron detector, a higher efficiency is obtained by sampling the thermal neutron density near the surface. In this case, the applicable formula[6]) for the thermal neutron density is

$$\rho = \frac{S\tau}{2r} \sum_{m=1}^{\infty} \frac{m}{a^2 + m^2\pi^2L^2} \cdot \exp\left(-m^2\pi^2\theta_0/a^2\right) \cdot \sin\left(m\pi r/a\right) \quad (2)$$

[5]) The graphite came from a stack used by several annual classes of the ORNL Reactor School. One of their laboratory problems is the determination of L from measurements of foil activation as a function of distance. The value quoted is an average of many such determinations, kindly supplied by H. S. Pomerance.

where S, a, L, θ_0 are as defined above, τ is the mean lifetime of a thermal neutron in an infinite medium and r ($\leqslant a$) is the radial coordinate of a point within the sphere.

Fig. 1 is a plot of the thermal neutron density at a radial distance of 69.7 cm in the 78.2 cm sphere actually constructed, normalized

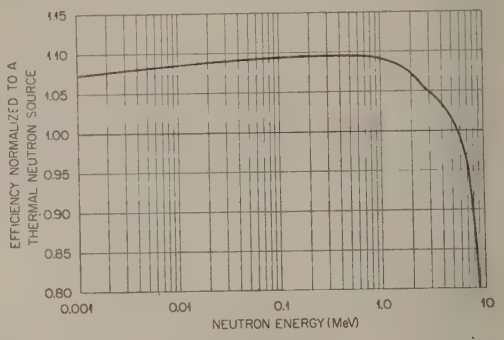

Relative Efficiency of Graphite Sphere with Central Neutron Source. $a = 80.0$ cm; $r = 69.7$ cm; $L = 48.8$ cm; $\rho = 1.652$ g/cm^3

Fig. 1. Calculated efficiency curve for the graphite sphere with $B^{10}F_3$ proportional counters in tangential holes near the surface.

to unity for a thermal neutron source at the center. For the thermal source, the pertinent equation is

$$\rho = \frac{S\tau \sinh\left(\frac{a-r}{L}\right)}{4\pi r L^2 \sinh\left(a/L\right)} \cdot \quad (3)$$

The value taken for L is 48.8 cm[5]) and values of θ_0 have been computed from the carbon total cross section and an average graphite density reported as 1.652, using the conventional formulas[7]). The usual correction of one third the squares of the mean free paths of the first and last collisions has been added, to correct for the effect of the neutron's unimpeded (undiffused) flight just after leaving the source and just before absorption in a detector. The indicated efficiency is constant within $\pm$ 1 % from about 1 keV to 2 MeV. Above 2 MeV the efficiency drops slowly with some irregularities

[6]) Given for example in "Elementary Approximations in the Theory of Neutron Diffusion," P. R. Wallace and J. LeCaine — National Research Council of Canada — Document 1480.

[7]) H. Soodak and E. C. Campbell, Elementary Pile Theory (J. Wiley and Sons, New York, 1950).

caused by carbon resonance structure. Above 5 MeV a predominance of forward elastic scattering and some inelastic scattering were also taken into account in determining the neutron age. The small fraction of the counting rate due to epithermal neutrons, calculated for a $1/v$ detector, rises with initial neutron energy to 0.2% at 10 MeV.

For use with reactions such as $Li^7(p,n)$ near threshold where the neutrons are concentrated in a forward cone, it was important to minimize any angular dependence of the detection efficiency. Eight $B_{10}F_3$[8]) counters were distributed as uniformly as possible over the graphite sphere as indicated in fig. 2. Since the neutrons become

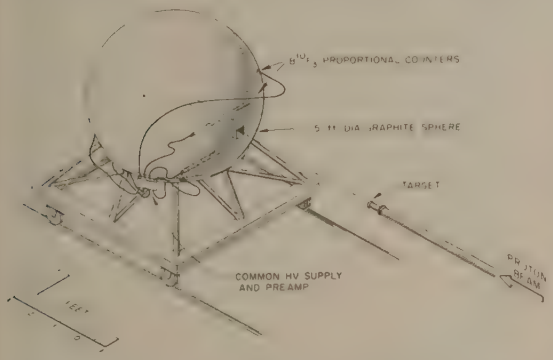

Fig. 2. Sketch of the counter showing method of introducing the proton beam and target at the center and indicating $B^{10}F_3$ counter placement.

essentially isotropic after their first scattering, the change in efficiency for a PoBe source was measured as a function of radial displacement. The result (0.14 ± 0.04% change per cm) indicates that maximum anisotropy (i.e. a undirectional beam) will change the efficiency less than 1.4% for energies up to 8 MeV and about 0.36% for the 29 keV and 64 keV threshold neutrons from the $Li^7(p,n)$ and $T^3(p,n)$ reactions[9]). The $4'' \times 4''$ channel left open to the center of the detector for the introduction of a Van de Graaff target increased the efficiency by 0.55 ± 0.034% at 25 keV as indciated by a plugging test with an Sb–Be source. With increasing energy this effect should decrease toward –0.17%, the subtended fractional solid angle. The total solid angle through gaps between the $4'' \times 4''$ graphite logs is this small or smaller, depending on surface irregularities.

After assembly, the fundamental decay period of thermalized neutrons in the graphite sphere was measured by the pulsed source technique of Campbell and Stelson[10]), who generously provided their equipment and personal assistance. The measured decay rate (reciprocal mean life) is simply related to the other parameters and D, the diffusion coefficient (6), as

$$\lambda = D/L^2 + \pi^2 D/a^2 = 361 \pm 9 \text{ sec}^{-1}. \quad (4)$$

The experimental decay was a simple exponential over a factor of at least 10^4, measuring from one or two milliseconds after the neutron burst (during which the higher modes decayed) until the counting rate became indistinguishable from background. $Li^7(p,n)$ and $T^3(p,n)$ both near threshold (neutrons in a forward cone) and well above threshold were used as pulsed neutron sources. Bare $B^{10}F_3$ counters and a $Li^6I(Eu)$ scintillator were tried as detectors. Source and detector positions inside, at the surface, and well outside the graphite were investigated in case any room scattered neutrons were being detected. The decay rates under all these conditions were statistically indistinguishable except when a $4'' \times 4'' \times 0.032''$ cadmium sheet or the eight $B^{10}F_3$ counters were inserted in the graphite.

The derived value of D is $(1.84 \pm 0.05) \times 10^5$ cm$^2 \cdot$sec^{-1}. This is rather lower than other results[11]) (2.13 and and 2.07, for graphite of density 1.6) and the difference is not well understood. The change in decay constant with the eight $B^{10}F_3$ counters in place was used to evaluate the mean flux at the counters and their mean radial position (69.7 cm) This mean radial

[8]) 1″ diameter × 20″ length aluminum counters filled to 120 cm pressure from Radiation Counter Laboratories, Skokie, Illinois.

[9]) R. L. Macklin and J. H. Gibbons, submitted for publication in Phys. Rev.

[10]) E. C. Campbell and P. H. Stelson, Bull. Am. Phys. Soc. 1 (1956) 183.

[11]) K. Beckurts, Nichtstationäre Neutronenfelder (Gottingen, 1956) and Antonov *et al.*, Geneva Conference on Peaceful Uses of Atomic Energy (1955) Paper No. 661.

distance compares well with the 67.0 cm minimum distance to the nearest part of each counter, as they are about 2.5 cm in diameter and tangential. In any case, the calculated efficiency curve is insensitive to a few centimeters displacement of the counter positions.

3. Calibration

Antimony-beryllium sources standardized at the National Bureau of Standard[12]) were used to determine the counter efficiency. This changed no more than from 0.0308 to 0.0304 over a period of six months during which some deterioration of the $B^{10}F_3$ counters was noticed. The expected uncertainty in the Sb–Be source was about 3%. To avoid additional uncertainties from the Sb^{124} decay, its half-life was redetermined, first by the intercomparison of two standard sources activated nine months apart, and second by comparison of the stronger with a half gram Ra-γ-Be secondary standard. The first method gave 60.3 ± 0.5 days and the second during the period from the sixth to the ninth month after source activation gave 60.4 ± 0.2 days.

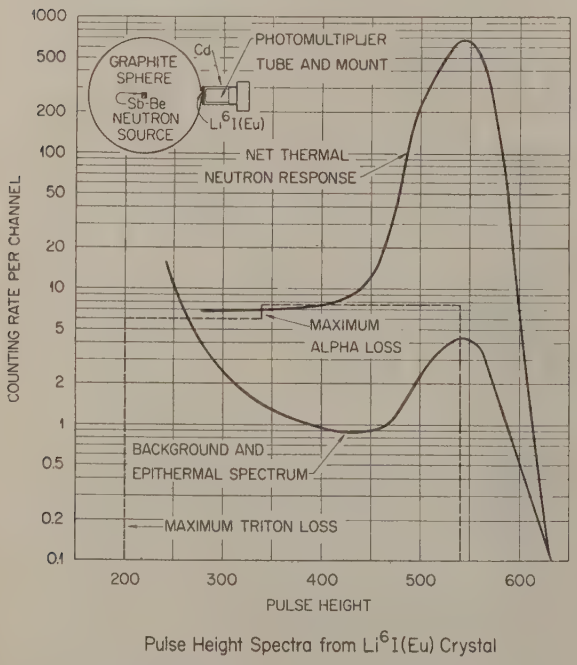

Fig. 3. Differential pulse height distributions for the $Li^6I(Eu)$ scintillation detector used for the thermal leakage measurements.

An independent calibration was accomplished by measuring the thermal leakage flux with the standard Sb–Be source at the center of the sphere and the $B^{10}F_3$ counters removed. A thin disc (0.2 cm × 3.2 cm dia) of $Li^6I(Eu)$† was used as a scintillation neutron detector and carefully shielded with cadmium to sharply define the accessible surface region. Response curves for this detector are shown in fig. 3. The lower curve shows the differential pulse height distribution with a 1.2 g/cm² boron filter between the detector and the graphite. A 0.032″ Cd filter gives a slightly higher curve at low pulse heights due to capture gamma rays. The upper curve in fig. 3 shows the net thermal neutron response. The peak response is attributed to complete absorption of the alpha particle and triton from $Li^6 + n \longrightarrow \alpha + T^3 + 4.78$ MeV. Since the crystal used is 99.0% opaque to an isotropic thermal neutron source (82% at 0.4 eV), most of the neutrons are captured very near the surface of the crystal. Thus an appreciable fraction ($3\frac{1}{2}$%) of the charged particles escape from the crystal with part of their energy. This effect has been estimated, assuming linear light output with range but that the triton has 30% greater light efficiency than the alpha particle. The calculated pulse height distribution, uncorrected for instrumental resolution, is shown as the dotted curve in fig. 3.

The response of the $Li^6I(Eu)$ thermal neutron detector was studied as a function of surface position on the graphite sphere. Wall and floor reflection was estimated to contribute a small fraction of one percent to the neutron population, but cadmium floor and wall shielding was added at the points of closest approach as a further precaution. No effects attributable to wall or floor reflection were found, but zones of average dimension of a foot or so were found where the thermal leakage departed by as

[12]) J. De Juren and J. Chin, Journal of Research, National Bureau of Standards 55 (1955) 311.

† Kindly loaned by R. B. Murray and J. J. Manning of Oak Ridge National Laboratory.

much as 8% from the average. These effects may be due to (1) inhomogeneous distribution of neutron absorbing impurities or (2) local differences in adsorbed water dependent upon non-uniform graphite porosity and density.

Combining the measurements of thermal exit current with the age-diffusion calculations, one arrives at a source strength 8½% below the NBS manganese bath[12]) value, corresponding to a counter efficiency, with the eight $B^{10}F_3$ counters in place, of 0.0338 to 0.0332. Several minor effects also included in the calculation were (1) neutron absorption by I and Eu in the Li^6I(Eu) scintillation counter (0.83%) (2) slight displacement of the detector from the graphite surface (0.25%) (3) neutron absorption by the Sb–Be source (calculated as 0.10% and undetected when investigated with an unactivated source during the pulsed neutron decay period tests) (4) enhanced leakage from the graphite sphere due to the source cavity (0.21%) and (5) recording of unthermalized neutrons below the 0.4 eV cadmium filter cutoff (0.11%). Counting statistics were 0.55%.

In view of the slight discrepancy with the NBS calibration of our Sb–Be source (3 times the NBS standard error) a more direct inter- comparison of standards would be desirable. A direct redetermination of the density and thermal diffusion length of the graphite sphere is anticipated.

4. Operation

The eight $B^{10}F_3$ proportional counters were operated in parallel with a common stabilized high voltage supply and linear pulse amplification system. The resolving time (9.6 μsec as determined by the paired source method) was primarily associated with the pulse height selection stage in the electronic equipment. With a Po–Be neutron source, the differential pulse height distribution showed an asymmetric peak (0.8 mV) at eight times the comparable noise level (0.1 mV) with a peak to valley ratio of 2.4. The net neutron counting rate showed 200–300 volt plateaux with about 1% slope per 100 V at applied potentials near 3400 V. The spurious background rose quite rapidly with potential, however, so that the gross counting rate plateau was steeper. The gamma sensitivity was determined with a Sb^{124} source of 2.4 times the gamma activity of the stronger standard Sb–Be source. The net pulse height bias curve showed mostly smaller pulses than were accepted in neutron counting but gave a small "tail" of large pulses with a distribution very similar to the neutron pulses. Traces of beryllium in the graphite do not seem sufficient to account for this effect. Considering the yield of neutrons from the Sb–Be source, the ratio of efficiencies of the counters for gamma rays and neutrons was about 10^{-7}. The overall daily stability of the counting system for neutrons was better than 0.2% with small changes in amplifier gain the most noticeable contributor on this time scale. Backgrounds ranged from 2 to 3 c/s in the absence of local sources and without shielding (altitude 800 ft).

5. Conclusions

The counter described provides unique advantages in precise neutron measurements at energies up to several MeV. Particular applications include the investigation of (p,n) and (d,n) cross sections, emission rates of radioactive neutron sources, and absolute values of η, the average number of fission neutrons per neutron absorbed for thermal neutrons.

NUCLEAR INSTRUMENTS 1 (1957) 340–342; NORTH-HOLLAND PUBLISHING CO. – AMSTERDAM

DIE BLASENDICHTE IN EINER BLASENKAMMER UNTER VERSCHIEDENEN BETRIEBSBEDINGUNGEN

GERHARD HORLITZ und WOLFGANG PAUL

Physikalisches Institut der Universität, Bonn

Received 7 May 1957

The bubble density b in a bubble chamber depends on the difference between the pressure of the saturated vapour $P_\infty(T)$ and the hydrostatic pressure P, i.e. $b = F(P_\infty(T) - P)$. Therefore b increases very rapidly with temperature, if P is kept constant. In a dirty bubble chamber P depends on the expansion ratio and on the temperature. We found, that for certain expansion ratio b does not depend on temperature for an interval of several degrees.

In letzter Zeit sind einige Untersuchungen über das Verhalten einer Blasenkammer unter verschiedenen Betriebsbedingungen veröffentlicht worden[1,2,3]). Insbesondere wurde die Abhängigkeit der Blasendichte b (Zahl der Blasen pro cm Spurenlänge) von der Energie der zu registrierenden Teilchen einerseits und von der Temperatur der Kammerflüssigkeit andererseits untersucht mit dem Ziel, eine der Korndichte in Kernemulsionen, beziehungsweise der Tröpfchendichte in Wilsonkammern analoge Messgrösse zur Identifizierung von Teilchen zu gewinnen.

Die bisher veröffentlichten Ergebnisse lassen eine lineare Abhängigkeit der Blasendichte von $1/\beta^2$ (β ist das Verhältnis der Geschwindigkeit des Teilchens zur Lichtgeschwindigkeit) erkennen in der Form

$$b = \frac{A}{\beta^2} + B(T) \qquad (1)$$

beziehungsweise

$$b = \frac{C(T)}{\beta^2} \,. \qquad (2)$$

Sie zeigen übereinstimmend ein ausserordentlich starkes Anwachsen der Blasendichte mit der Temperatur, wobei einer Temperaturänderung von 1 °C eine Änderung der Blasendichte bis zu 50 % entsprechen kann. Das bedeutet, dass für einigermassen genaue Messungen die Temperatur auf einige Zehntelgrad konstant gehalten werden muss. Die Erfüllung dieser Forderung ist zwar technisch möglich, aber doch, insbesondere bei grösseren Kammern, recht unbequem.

Einige der veröffentlichten Kurven[1,3]) lassen in einem kleinen Temperaturintervall eine geringere Neigung erkennen. Es erhebt sich die Frage, ob dieses Plateau reell ist, ob es sich beeinflussen und eventuell auf einen grösseren Temperaturbereich erweitern lässt.

Aus den verschiedenen Ansätzen zur Theorie der Blasenbildung[4,5,6,7,8]) geht hervor, dass die Blasendichte im wesentlichen von der Differenz $P_\infty(T) - P$ zwischen Sättigungsdampfdruck $P_\infty(T)$ und hydrostatischem Druck P zur Zeit der Blasenbildung abhängt und mit dieser Differenz zunimmt. Vorausgesetzt, dass P nicht von der Temperatur abhängt, steigt b also mit dem Sättigungsdampfdruck $P_\infty(T)$.

Nun trifft die Voraussetzung $P = \text{const.}$ nur in einer absolut sauberen Kammer aus Glas zu, keinesfalls jedoch in einer Metallkammer. Sowie nämlich in dieser bei einer Expansion der Druck unter den Sättigungsdampfdruck gesunken ist, beginnt die Flüssigkeit an den Wänden und

[1]) D. A. Glaser, D. C. Rahm and C. Dodd, Phys. Rev. **102** (1956) 1653.

[2]) G. A. Blinov, Y. u. S. Krestnikov and M. F. Lomanov, CERN Symposium (1956) 26.

[3]) P. Bassi, A. Loria, J. A. Meyer, P. Mittner and I. Scotoni, Nuovo Cimento **4** (1956) 491.

[4]) D. A. Glaser, Nuovo Cimento **11** Suppl. (1954) 361.

[5]) G. Martelli, Nuovo Cimento **12** (1954) 250.

[6]) L. Bertanza and G. Martelli, Nuovo Cimento **1** (1955) 324.

[7]) L. Bertanza, G. Martelli and A. Zacutti, Nuovo Cimento **2** (1955) 487.

[8]) I. A. Pless and R. J. Plano, Rev. Sci. Inst. **27** (1956) 935.

Dichtungen zu verdampfen und der Druck steigt wieder an. Die Anstiegsgeschwindigkeit hängt vom zur Verfügung stehenden Volumen und damit vom Expansionsverhältnis ab. Dadurch wird nun der wirklich in der Kammer herrschende effektive hydrostatische Druck P_{eff} und damit auch die Blasendichte b eine Funktion des Expansionsverhältnisses.

Stellt man in einer mit einer Membran abgeschlossenen Metallkammer (Abb. 1) bei einer bestimmten Temperatur das Expansionsverhältnis ein, so ist auch dieses bei einer Temperaturänderung nicht konstant. Die Bewegung der

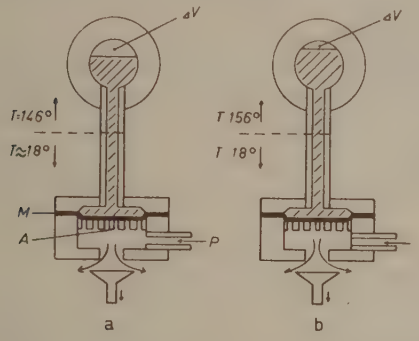

Abb. 1. Versuchsanordnung (schematisch). Der obere Teil der Kammer wird elektrisch beheizt, alle übrigen Teile befinden sich auf Zimmertemperatur. Durch Einlassen von Pressluft in den Raum unterhalb der Membran bei geschlossenem Ventil wird der Dampf komprimiert. Expansion erfolgt durch plötzliches Öffnen des Ventils. Die Abbildung zeigt die Kammer in expandiertem Zustand, und zwar a) bei niedriger Temperatur, b) bei höherer Temperatur. Durch thermische Ausdehnung der Flüssigkeit wird das dem Dampf zur Verfügung stehende Volumen ΔV verkleinert.
M Gummimembran
A Anschlag für Membran (durchbrochen)
P Presslufteinlass (30 atü).

Membran muss ja durch einen Anschlag begrenzt werden, da sie sonst zerstört würde. Dieser Anschlag bestimmt das Gesamtvolumen, das Flüssigkeit und Dampf zusammen im expandierten Zustand einnehmen. Nur dieses ist konstant. Das Expansionsverhältnis, definiert durch das Verhältnis,

$$\frac{\Delta V}{V} = \frac{\text{Gesamtvolumen} - \text{Flüssigkeitsvolumen}}{\text{Gesamtvolumen}},$$

nimmt, wenn man die Kammer sonst unverändert lässt (also unter normalen Betriebsbedingungen), wegen der thermischen Ausdehnung der Flüssigkeit mit steigender Temperatur ab. Das bedeutet, dass P_{eff} mit der Temperatur zunimmt.

Eine Erhöhung der Temperatur wirkt also in zweifacher Weise auf die Blasendichte ein: Einmal über den Sättigungsdampfdruck $P_\infty(T)$, wodurch b vergrössert wird, zum andern über P_{eff}, was eine Verringerung von b zur Folge hat. Welcher der beiden Effekte überwiegt, hängt vom Temperaturbereich und vom Expansionsverhältnis ab. Damit kann man also den Verlauf der Blasendichte in Abhängigkeit von der Temperatur in ziemlich weiten Grenzen varieren.

Es wurde nun untersucht, ob es einen Temperaturbereich gibt, in dem die Blasendichte weitgehend unabhängig von der Temperatur ist. Die Kammer, mit der die Untersuchungen durchgeführt wurden, ähnelt im wesentlichen dem zuerst von Glaser veröffentlichten Modell[9]). Kompression und Expansion werden über eine Membran mittels Pressluft vorgenommen. Als empfindliche Flüssigkeit diente Diäthyläther. Bei einer Anfangstemperatur von 146.5 °C wurde ein bestimmtes Expansionsverhältnis $\Delta V/V$ eingestellt und dann die Blasendichte an Spuren von Comptonelektronen im Minimum der Ionisation in Abhängigkeit von der Temperatur gemessen. Die Elektronen wurden durch γ-Quanten einer Co^{60}-Quelle innerhalb der Flüssigkeit erzeugt. Anstelle der wirklichen Blasendichte wurde die auf eine Ebene senkrecht zur Beobachtungsrichtung projizierte Blasendichte $\bar{n}$ gemessen, die im Mittel die gleiche Abhängigkeit aufweisen muss. Zur Auszählung gelangten nur Spuren von mindestens 5 mm Länge, wobei das Ende jeder Spur auf eine Länge von 2 mm wegen des starken Anstiegs der Ionisationsdichte ausgelassen wurde. Im Durchschnitt wurden pro Messpunkt etwa 130 Spuren ausgemessen.

Das vorläufige Ergebnis dieser Untersuchungen zeigt Abb. 2: Kurve I wurde mit einem Anfangsexpansionsverhältnis von 2.3% aufgenommen. Die Blasendichte sinkt sofort mit steigender Temperatur. P_{eff} steigt hier also so

[9]) D. A. Glaser and D. C. Rahm, Phys. Rev. **97** (1955) 474.

stark an, dass der Verlauf der Kurve in überwiegendem Masse dadurch bestimmt wird. Unterhalb 146° nimmt die Blasendichte so rasch ab, dass eine sichere Auswertung wegen der Kürze der zur Verfügung stehenden Spuren nicht mehr möglich ist.

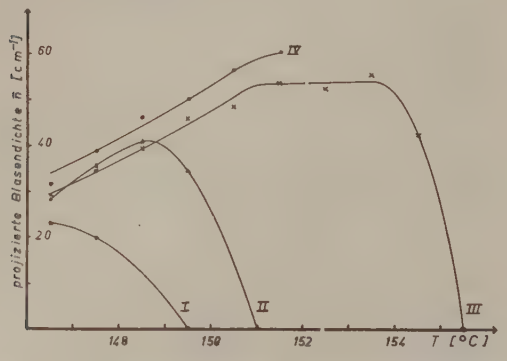

Abb. 2. Projizierte Blasendichte n in Abhängigkeit von der Temperatur (Anfangsexpansionsverhältnis als Parameter).

I $(\Delta V/V)_{146.5°} = 2.3\%$
II $(\Delta V/V)_{146.5°} = 2.9\%$
III $(\Delta V/V)_{146.5°} = 4.1\%$
IV $(\Delta V/V)_{146.5°} = 4.8\%$.

Kurve II mit einem Anfangsexpansionsverhältnis von 2.9% steigt zunächst an, durchläuft ein Maximum und nimmt dann ebenfalls wieder ab.

Bei einem Anfangsexpansionsverhältnis von 4.1% erhält man die Kurve III. Sie zeigt ein ausgeprägtes Plateau im Temperaturbereich zwischen 151° und 154°. In diesem Bereich ändert sich die Blasendichte nicht innerhalb der Fehlergrenzen, die dort etwa 5% betragen.

Die letzte Kurve wurde mit einem Anfangsexpansionsverhältnis von 4.8% gemessen. Die Blasendichte steigt kontinuierlich an; oberhalb 152° setzte die spontane Blasenbildung in so starkem Masse ein, dass der Verlauf nicht weiter zu verfolgen war. Diese Kurve dürfte den bisher veröffentlichten Messungen entsprechen.

Bereits diese noch unvollständigen Versuchsergebnisse lassen erkennen, dass es möglich ist, eine Blasenkammer unter Bedingungen zu betreiben, unter denen die Blasendichte praktisch nicht von der Temperatur abhängt.

Herrn cand. phys. G. Kesseler danken wir für seine Hilfe bei den Messungen.

Die Untersuchungen wurden mit Hilfe der Deutschen Forschungsgemeinschaft durchgeführt.

NUCLEAR INSTRUMENTS 1 (1957) 343–344; NORTH-HOLLAND PUBLISHING CO. – AMSTERDAM

THE VERTICAL MOTION OF PARTICLES THROUGH THE REGENERATIVE BEAM EXTRACTOR OF A SYNCHROCYCLOTRON

K. J. LE COUTEUR

Research School of Physical Sciences, Australian National University, Canberra A. C. T.

Received 2 September 1957

In a regenerative beam extractor, the vertical motion of particles approaching the regenerator is shown to be correlated about the line $\dot{Z} = -\frac{1}{2}TZ$; this correlation permits efficient design of the magnetic channel.

The general theory of regenerative extraction of synchrocyclotron beams[1,2,3,4]) establishes conditions for exponential growth of radial oscillations and for stability of the vertical motion. The exponential growth of the radial oscillations leads the particles into orbits with a fixed radial node, which acts as a virtual source for the particles entering the magnetic channel. Conversely at first sight the stability of the vertical motion suggests that it has a random phase, but a closer examination of the theory shows that, as stated in ref.[2]), the regenerative deflector induces strong correlation into the vertical motion. This can readily be seen from the orbits tabulated by Le Couteur and Lipton[4]) in an appendix, which show that at azimuth 32° before the regenerator, roughly the position of the mouth of the magnetic channel, Z and $\mathrm{d}Z/\mathrm{d}\theta$ have opposite sign. Thus, as they approach the channel the particles are converging towards the median plane and this information can be used to design the vertical aperture and radial and vertical focussing properties of the magnetic channel for optimum beam transmission. This possibility has now been realised by Wilson *et al.*[5]) on the Harvard synchrocyclotron; as their paper relies on reference to the unpublished proposals of the author it is desirable to give a short account of the physical reason for the phase correlation of the vertical motion.

For simplicity, consider a deflector with no peeler but only a regenerator which, in the notation of ref.[3]), gives a vertical impulse

$$\dot{Z}_{\mathrm{out}} = \dot{Z}_{\mathrm{in}} + T_{\mathrm{v}}Z : Z_{\mathrm{out}} = Z_{\mathrm{in}} = Z \qquad (1)$$

to particles passing through it. Hence

$$(Z\dot{Z}_{\mathrm{out}}) = (Z\dot{Z}_{\mathrm{in}}) + T_{\mathrm{v}}(Z^2) \qquad (2)$$

and

$$(\dot{Z}_{\mathrm{out}}{}^2) - (\dot{Z}_{\mathrm{in}}{}^2) = T_{\mathrm{v}}(Z(\dot{Z}_{\mathrm{out}} + \dot{Z}_{\mathrm{in}})) \qquad (3)$$

where the ( ) denotes a statistical average over the beam.

But

$$(\dot{Z}_{\mathrm{out}}{}^2) = (\dot{Z}_{\mathrm{in}}{}^2)$$

since there is no steady growth or decay of the vertical motion and so (2) gives

$$(Z\dot{Z}_{\mathrm{in}}) = -(Z\dot{Z}_{\mathrm{out}}) = -\tfrac{1}{2}T_{\mathrm{v}}(Z^2). \qquad (4)$$

Thus for vertical motion of particles approaching the regenerator the line of regression of $\dot{Z}$ on Z is

$$\dot{Z} \frac{(Z\dot{Z})}{(Z^2)} Z = -\tfrac{1}{2}T_{\mathrm{v}}Z \qquad (5)$$

and this may easily be checked by plotting the numerical values of Z and $\dot{Z}$ from the appendix of ref.[4]).

This simple argument demonstrates the existence but not the magnitude of the correlation, which is however easily derivable in the linear

[1]) K. J. Le Couteur, Proc. Phys. Soc. B **64** (1951) 1053.
[2]) K. J. Le Couteur, Proc. Phys. Soc. B **66** (1953) 25.
[3]) K. J. Le Couteur, Proc. Roy. Soc. A **232** (1955) 236.
[4]) K. J. Le Couteur and S. Lipton, Phil. Mag. **46** (1955) 1265.
[5]) G. Calame, P. Cooper, S. Engelsberg, G. Gerstein, A. Koehler, A. Krukes, J. Meadows, K. Straunch and R. Wilson, Nuclear Instruments **1** (1957) 169.

case from the results of appendix A of ref.[1]). Eq. A(7) gives

$$\frac{(Z\dot{Z})}{(\dot{Z}^2)} = a \cos b = -\tfrac{1}{2} \frac{T}{\omega^2 - \frac{T}{\omega} \cot 2\pi\omega}, \qquad (6)$$

in the special case $S = d = 0$ of no peeler, and also lead to (4). So the line of regression of Z on $\dot{Z}$ is

$$Z = -\tfrac{1}{2} \frac{T}{\omega^2} \dot{Z}, \qquad (7)$$

in the typical case $\omega = \frac{1}{4}$, and the coefficient of correlation of Z and $\dot{Z}$ is

$$r = \frac{T}{2\omega}, \qquad (8)$$

which is always less than 1 since the magnitude of T is limited by the requirements of vertical stability.

The simple derivation of eq. (5) shows that it remains valid in the important practical case of a non linear system, whereas (6), (7), (8) require elaboration.

NUCLEAR INSTRUMENTS 1 (1957) 345–350; NORTH-HOLLAND PUBLISHING CO. – AMSTERDAM

EFFICIENT DETECTOR FOR HIGH ENERGY NEUTRONS†

N. E. BOOTH AND B. LEDLEY

Department of Physics, University of Birmingham

Received 30 September 1957

A detector of neutrons in the energy range 400–900 MeV has been constructed and studied. At 800 MeV its efficiency is 1–2%. It consists of a rod of perspex 10 cm in diameter and 50 cm long, one end of which is viewed by a photomultiplier. High energy incident neutrons are detected by observing the Cherenkov light emitted by charged secondary particles produced in the perspex. Since the average pulse height increases with incident neutron energy, the effective energy threshold may be raised by pulse height selection. Experimental results are presented for the dependence of the efficiency upon the energy and direction of secondary protons. The neutron detection efficiency has been calculated as a function of energy.

1. Introduction

Effects which have been used to detect neutrons of energies > 100 MeV include the C^{11} activity produced by the reaction C^{12} (n, 2n) C^{11} [1]), the fission of Bi [2]), the production of knock-on protons from light elements[3,4]) and the production in scintillators of charged reaction products[5]). Methods based on time-of-flight[6]) have been used to obtain good energy resolution but with a considerable sacrifice of overall efficiency.

At these energies neutrons are produced by bombarding an element with accelerated charged particles. The resultant neutron energy spectrum is very broad and one must sacrifice counting efficiency in order to select neutrons with a small energy spread. A neutron detector has been designed having a higher efficiency than other detectors which have been used in this energy range[4,7]), and enabling a reasonable compromise to be made between efficiency and energy selection.

2. The Detector

The detector, shown in fig. 1, consists of a polished rod of perspex 50 cm long and 10 cm in diameter. High energy incident neutrons produce energetic charged secondary particles in the perspex and some of the Cherenkov light produced is detected by the photomultiplier, which is a 5 in. diameter Du Mont type 6364 optically sealed to the perspex with silicone oil. The end of the perspex facing the incident beam is roughened and blackened to reduce the light collection efficiency for background particles.

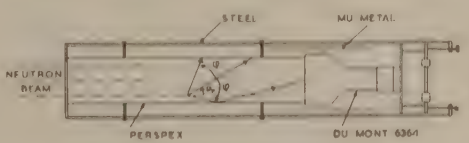

Fig. 1. Cherenkov neutron detector.

The threshold energy in perspex for Cherenkov radiation from protons is about 325 MeV but, by setting a bias level so as to accept only those pulses above a given height, the effective energy threshold may be made considerably higher.

† A preliminary report on this work was presented at the Nuclear Physics Meeting of the Physical Society, January 1957.

[1]) L. J. Cook, E. M. McMillan, J. M. Peterson and D. C. Sewell, Phys. Rev. **75** (1949) 7.

[2]) C. Wiegand, Rev. Sci. Inst. **19** (1948) 790.

[3]) V. A. Nedzel, Phys. Rev. **94** (1954) 174.

[4]) T. Coor, D. A. Hill, W. F. Hornyak, L. W. Smith and G. Snow, Phys. Rev. **98** (1955) 1369.

[5]) E. R. Christie, B. T. Feld, A. C. Odian, P. C. Stein and A. Wattenberg, Rev. Sci. Inst. **27** (1956) 127.

[6]) W. I. Linlor and B. Ragent, Phys. Rev. **91** (1953) 440A.

[7]) V. P. Dzhelepov, V. I. Satarov, and B. M. Golovin, Doklady Akad. Nauk S.S.S.R. **104** (1955) 717.

This is possible because, firstly, the Cherenkov light output increases with increasing charged particle (and therefore neutron) velocity and, secondly, as the velocity increases, the charged secondaries are emitted at smaller angles to the forward direction in the laboratory system and give larger pulses.

3. Efficiency of the Detector

The efficiency of the detector for neutrons of a given energy may be calculated from knowledge of the production cross sections and of the energy and angular distributions of the charged secondaries. In addition, one needs to know the light collection efficiency as a function of the velocities and trajectories of the secondaries. Although the amount of Cherenkov light produced may be calculated from the Frank and Tamm equation[8]), the light collection efficiency is difficult to estimate, even when idealized assumptions are made.

In considering the light collection efficiency we shall, for the sake of simplicity, consider only (n, p) elastic events in the hydrogen of the perspex, estimating the effect of the inelastic processes as a correction in section 6. In practice one would like to know the photomultiplier output pulse height as a function of the incident neutron kinetic energy, T_n, and the angle of the recoil proton, θq (see fig. 1). For this purpose we have made a study of the relative pulse heights produced by protons of various energies passing through the detector at various angles to its axis

4. Experiments with Protons

A beam of fairly monoenergetic protons was obtained by scattering the circulating beam of the Birmingham proton synchroton from a polythene target inside the synchrotron vacuum chamber. The energy of the scattered beam can be altered by changing the instant during the accelerating cycle at which the circulating protons are driven on to the target[9]). The experimental arrangement is shown in fig. 2.

[8]) I. Frank and I. Tamm, Compt. Rend. Acad. Sci. U.S.S.R. **14** (1937) 109.

The detector was orientated in the beam and the output of the photomultiplier was fed to a 60 channel kicksorter[10]).

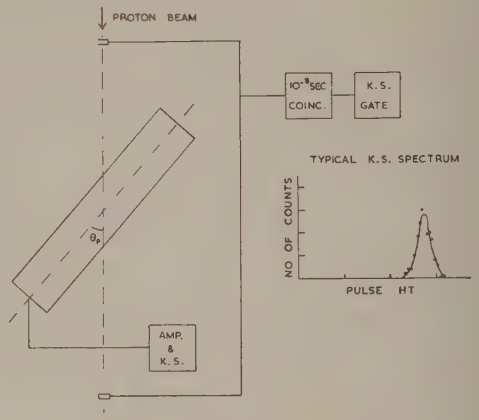

Fig. 2. Arrangement for measurements with protons. The detector is placed in a beam of protons defined by two scintillators in coincidence. A typical gated kicksorter spectrum is included.

The coincident output from the two plastic scintillators was used to gate the kicksorter so that only those pulses were displayed which were due to protons passing completely through the detector. The detector was mounted on a table which could be rotated and shifted horizontally to alter the angle θ_p and the point of incidence of the beam on the detector. A typical pulse height spectrum from the kicksorter is included in fig. 2. A series of such spectra were obtained for various proton energies and angles. The proton energies were corrected for energy loss in the first scintillator, in the steel and brass of the detector container and in the perspex[11]). From these results one can determine the pulse heights for recoil protons produced by neutrons of a given energy, T_n, incident on the detector as a function of T_n and θ_p. The results for recoil protons originating at the centre of the detector are shown in fig. 3. The curves of fig. 3 take into

[9]) D. E. Caro and L. U. Hibbard, Phil. Mag. Ser. 7 **44** (1953) 964; N. E. Booth and G. W. Hutchinson, Nuclear Instruments **1** (1957) 80.

[10]) G. W. Hutchinson and G. G. Scarrott, Phil. Mag. Ser. 7, **42** (1951) 792.

[11]) W. A. Aron, B. G. Hoffman and F. C. Williams, U.S. Atomic Energy Commission Report AECU-663 (1951).

account the kinematic change in proton energy with recoil angle and the change in the path length through the perspex with angle due to the geometry of the detector.

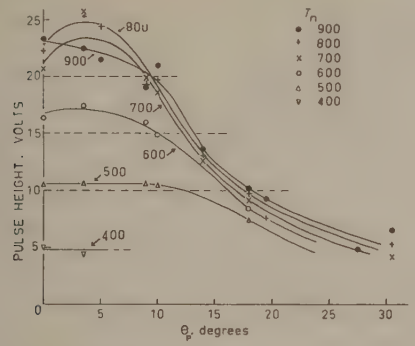

Fig. 3. Pulse heights of recoil protons as a function of proton recoil angle. T_n is the incident neutron energy in MeV.

We shall now proceed to show how the energy dependence of the efficiency of the detector may be calculated assuming for the moment only (n,p) elastic events.

5. Detection of (n,p) Elastic Events

The efficiency for detection of (n,p) elastic events is obviously a function of the bias level or minimum pulse height considered. We shall take the bias levels 10, 15 and 20 volts as representative (see fig. 3). Except for the change in Cherenkov angle and the variation of the (n,p) elastic cross section with energy, increasing the bias level gives a similar effect to that which would be obtained by using a Cherenkov radiator of a lower refraction index.

We now wish to calculate the number of (n,p) elastic events which give pulses above the chosen bias level as a function of energy. For a given neutron energy we integrate the differential cross section from $0°$ to $\theta°$, where θ is the angle at which the recoil proton pulse height drops to the chosen bias level. The angular distribution of (n,p) elastic scattering has been measured at 580 MeV[12]). We shall assume that the same angular distribution exists in the centre-of-mass system over the whole range of interest (400–900 MeV). The angular distribution in the laboratory system was then calculated at 100 MeV intervals from 500 to 900 MeV and normalized to the approrpiate integrated elastic cross section. The elastic cross section is 33 ± 2 mbn at 380 MeV[12]), 26 ± 3 mbn at 580 MeV[12]) and 19 ± 4 mbn at 950 MeV[13]). Fig. 4 shows the cross sections obtained by integrating from $0°$ to $\theta°$ plotted as a function of neutron energy. We have evaluated θ by considering only recoils produced at the centre of the detector. This is a good approximation: an exact value of θ would be obtained by averaging its value over the volume of the detector through which the neutron beam passes.

To calculate the absolute efficiency of the detector one must know its effective length. This may be estimated by considering the various path lengths of the recoils produced along the axis of the detector and by using the curves of fig. 3. The effective length will of course depend upon the neutron energy.

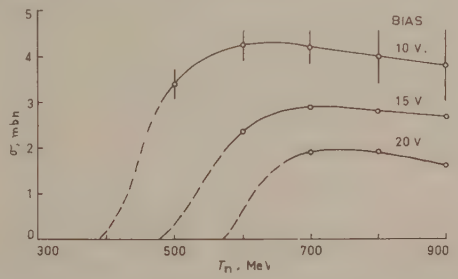

Fig. 4. Cross section for the detection of (n,p) elastic events. The errors shown are representative.

6. Detection of Inelastic Events

We now go on to consider the effect of charged secondaries produced by inelastic events in the hydrogen, carbon and oxygen nuclei of the perspex. The processes of interest are charged and neutral pion production, and, in the C and O, direct interactions leading to energetic protons in the forward direction.

6.1. NEUTRAL PION PRODUCTION

Neutral pion production accounts for a considerable fraction of the inelastic cross sections

[12]) Iu. M. Kazarinov and Iu. N. Simonov, J. Exptl. Theoret Phys. (U.S.S.R.) **31** (1956) 169.

[13]) A. P. Batson, B. Culwick and L. Riddiford (private communication).

at 900 MeV (about 50 % for hydrogen). However, perspex has a low conversion efficiency for gamma-rays and only a small fraction of the decay gamma-rays are detected. Neutral pion production cross sections for H and C have been measured up to 660 MeV[14]) and at 950 MeV[13]) for H. Above 660 MeV the C cross section was assumed to have the same energy dependence as the H cross section. Cross sections were assumed to vary as $A^{2/3}$ [14]) so that the O cross sections are just 1.2 times those for C. The angular distributions in the laboratory system were estimated from the kinematics of the process and the limited data on measured angular distributions[14]). The efficiency for gamma-ray conversion was estimated from the results of Kantz and Hofstadter[15]). In order to estimate the pulse height produced by the conversion electrons, it was assumed that the light collection efficiency had the same angular dependence as the 900-MeV curve of fig. 3, but that the relative light output depended upon velocity in accordance with the Frank and Tamm equation.

6.2. CHARGED PION PRODUCTION

The production of charged mesons in (n,p) interactions has been investigated up to 660 MeV, where the cross section is 7.0 ± 2.6 mbn[16]), and at 950 MeV where the cross section is 8.4 ± 1.6 mbn[13]). The cross sections for C and O can be estimated up to 660 MeV and were assumed to have a similar energy dependence to the H cross sections at higher energies. The cross sections for detection at the various bias levels were calculated from measured[17]) and assumed energy and angular distributions. We have also taken account of the fraction of protons from both the reactions

$$\left.\begin{aligned} &\text{and} \quad n + p \rightarrow n + p + \pi^{\circ} \\ &\qquad n + p \rightarrow p + p + \pi^{-} \end{aligned}\right\} \qquad (1)$$

which move in the forward direction with sufficient velocity to be detected. These make a small contribution to the efficiency at the higher neutron energies.

6.3. INELASTIC PROTONS FROM C AND O

Unfortunately the production of protons through quasi-elastic or inelastic charge exchange scattering has not been so extensively investigated as meson production. A limited amount of information is available from radiochemical investigation of the (p,pn) and similar reactions[18]). We have assumed a cross section of 30 ± 15 mbn for proton production in C and O and assumed that the protons have the same energy and angular distribution as in free (n,p) scattering.

7. Energy Dependence of the Efficiency

The cross sections for detecting the various processes were added up to determine σ_H, σ_C and σ_O, the cross sections for the detection of charged secondaries from H, C and O respectively. We define

$$\bar{\sigma} = \frac{N_H \sigma_H + N_C \sigma_C + N_O \sigma_O}{N_H + N_C + N_O} \qquad (2),$$

where N_H, N_C and N_O are the relative numbers of H, C and O atoms respectively in perspex.

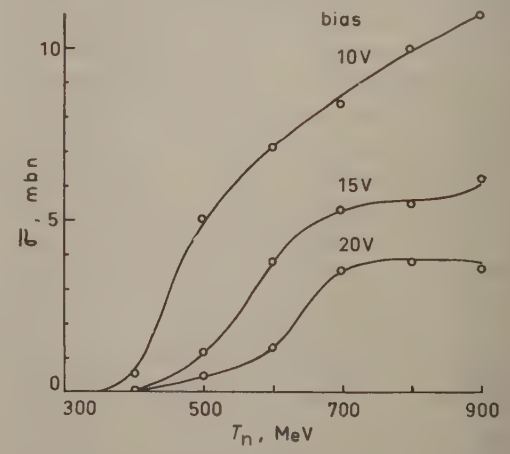

Fig. 5. Cross section in perspex for detection of incident neutrons of kinetic energy T_n.

Fig. 5 shows $\bar{\sigma}$ plotted as a function of neutron energy for the three bias levels.

[14]) Iu. D. Prokoshkin, Proc. CERN Symposium 2 (1956) 385.

[15]) A. Kantz and R. Hofstadter, Nucleonics 12 No. 3 (1954) 36.

[16]) Iu. D. Prokoshkin (private communication).

[17]) V. M. Sidorov, Proc. CERN Symposium 2 (1956) 366; M. M. Block *et al.*, *ibid.*, 374.

[18]) S. S. Markowitz, Thesis (Princeton University, 1957).

8. Absolute Value of the Efficiency

The efficiency of the detector for incident neutrons of energy T_n for a bias level V_b volts is

$$\eta(T_n, V_b) \quad \frac{\bar{\sigma}(T_n, V_b)[1 - e^{-\Sigma_t NL(T_n, V_b)}]}{\Sigma_t} \qquad (3),$$

where $L(T_n, V_b)$ is the effective length of the detector, N is Avogadro's number and

$$\Sigma_t = \frac{\sigma_t(H)\, N_H + \sigma_t(C)\, N_C + \sigma_t(O)\, N_O}{N_H + N_C + N_O} \qquad (4),$$

where σ_t (H), σ_t (C) and σ_t (O) are the neutron total cross sections of H, C and O respectively. We shall evaluate the efficiency for neutrons of an average energy of 760 MeV for $V_b = 15$V. Then we have $\bar{\sigma} = 5.4$ mbn and $\Sigma_t = 194$ mbn from the total cross sections measured in this laboratory at 765 MeV[19]).

The effective length L may be evaluated graphically to a sufficient accuracy by considering the decrease in path length for the secondaries originating close to the photomultiplier. Clearly, very few secondaries will be counted which originate at less than 15 cm from the photomultiplier, for they give pulses of height less than the bias level of 15V. Thus $L \approx 30$ cm and we have $\Sigma_t N = 0.021$ cm^{-1}. Therefore

$$\eta = \frac{5.4}{194}[1 - \exp(-0.021 \times 30)] = 1.3\,\% . \qquad (5)$$

9. Experiments with Neutrons

Neutrons were produced by bombarding an internal Be target with 920 MeV protons in the Birmingham synchrotron[19]). To reject charged particles a large scintillation counter was placed in the neutron beam directly in front of the Cherenkov detector and connected in anti-coincidence with it. A lead radiator was included in front of the two counters so that gamma-rays would be accompanied by electrons and also rejected. The pulse height spectrum from the detector is given in fig. 6. Work at lower energies[20,21]) suggests that the neutron spectrum at forward angles is of the form shown in fig. 7a.

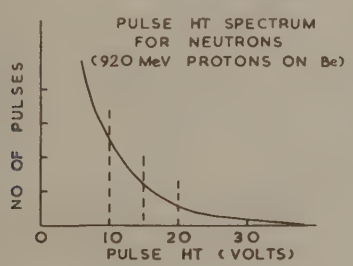

Fig. 6. Pulse height spectrum from the detector for neutrons produced by bombardment of Be with 920 MeV protons.

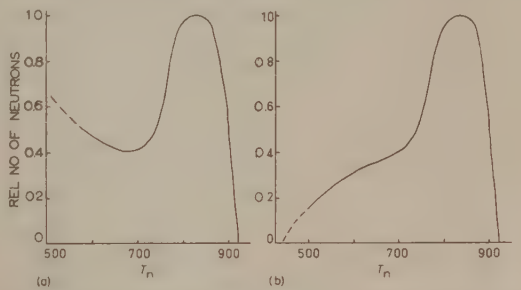

Fig. 7. (a) Assumed neutron spectrum from bombardment of Be with 920 MeV protons. (b) Spectrum weighted by detector efficiency at bias $V_b = 15$V.

Weighting this spectrum by the detector efficiency as a function of energy will give the effective energy spectrum of the neutrons

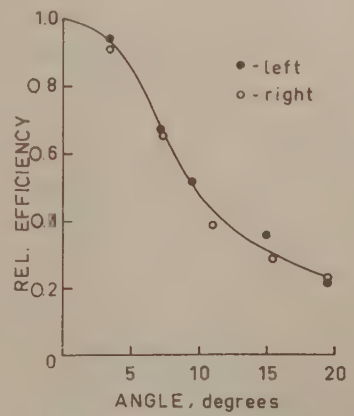

Fig. 8. Angular dependence of the efficiency of the detector for neutrons of an average energy of 765 MeV. The neutron beam was 5.1 cm diameter.

[19]) N. E. Booth, G. W. Hutchinson and B. Ledley, Proc. Phys. Soc. (to be published).

[20]) V. B. Flyagin, Report Inst. Nuc. Problems, Acad. Sci. U.S.S.R. (1954).

[21]) W. F. Goodell Jr., H. H. Loar, R. P. Durbin and W. W. Havens Jr., Phys. Rev. **89** (1953) 724.

detected. Fig. 7b shows the effective spectrum for $V_b = 15V$. The average neutron energy is then about 765 MeV.

The effective area of the detector was determined by performing a horizontal plot across a finely collimated beam. This indicated an effective diameter of 8.8 cm or 88% of the geometrical diameter. The angular dependence of the efficiency was measured by centring the detector in a beam of neutrons 5.1 cm in diameter and rotating it about the centre of its front face. The results are plotted in fig. 8.

Acknowledgements

We wish to express our thanks to Dr. G. W. Hutchinson for many helpful discussions and criticisms. One of us (N.E.B.) wishes to thank Imperial Oil Limited for the award of a Graduate Research Fellowship.

NUCLEAR INSTRUMENTS 1 (1957) 351–353; NORTH-HOLLAND PUBLISHING CO. – AMSTERDAM

FOCUSSING OF THE SYNCHROTON SCATTERED-OUT BEAM

H. B. VAN DER RAAY

Department of Physics, Birmingham University

Received 23 August 1957

A means of focussing the scattered-out beam of the Birmingham Proton Synchrotron by modifying the magnetic fringing field is outlined. The beam is brought to a spot focus of about 20 sq. cm at a distance of 5 meters from the exit port and has a mean intensity of 5×10^3 particles per sq. cm per pulse.

1. Introduction

At the present time no means of extracting the circulating beam of the Birmingham proton synchroton[1]) is available. Hence all experiments requiring an external proton beam rely on the scattering produced by a suitably positioned target. Some of those particles scattered in the forward direction pass through a step in the vacuum box, which is fitted with a thin hemispherical stainless steel window (see fig. 1). The area of this window defines the "external beam" available for experimental work. By altering the azimuthal or radial position of the target, the mean angle of scatter of the external beam may be varied over a limited range.

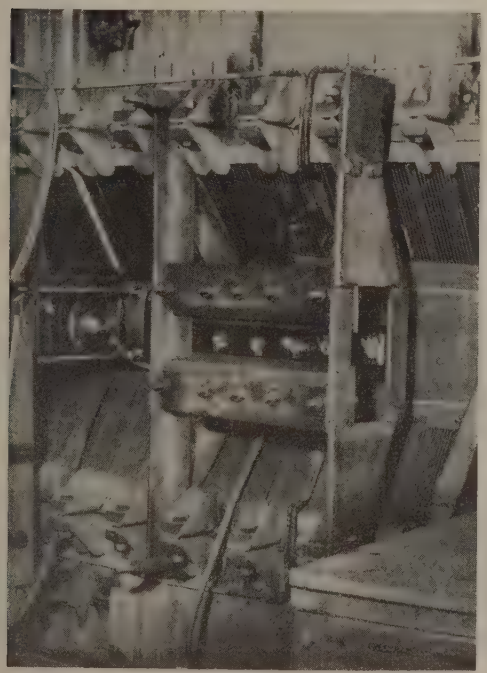

Fig. 1. Quadrupole in position showing hemispherical exit port.

Since many experimental techniques require the placing of apparatus at some distance from the machine, focussing of the scattered-out beam will enable experiments to be performed for which the necessary intensity would otherwise be lacking.

2. Vertical Focussing

The scattered beam passing through the thin window has a considerable path length in the fringing field of the synchrotron magnet. Due to the radial decrease of magnetic field intensity, the scattered particles experience a force directed toward the magnetic median plane. Also those particles which are moving at greater radii will be in a region of lower magnetic field and consequently their radius of curvature is greater than those protons in orbits closer to the machine. The result of these two factors is a net focussing of the beam in a vertical plane and a rapid defocussing in a horizontal plane. Consequently a horizontal line focus is formed in the median plane of the machine at a distance of approximately 150 cm from the exit port for a particular target position corresponding to a mean angle of scatter of 4°.

[1]) Moon Riddiford and Symonds, Proc. Roy. Soc. **230** (1955) 204.

Past this point the beam diverges in both directions. Thus if experimental equipment could be placed at or before this point, a fairly well defined beam of reasonable intensity could be obtained. Due to the limited space and the intense magnetic field in this region, only experiments using nuclear emulsions are practicable.

3. Quadrupoles

The action of the fringing field is similar to that of the first section of a magnetic quadrupole lens system[2,3]) with a superimposed constant magnetic field. As with such a system it is necessary to add a second lens of opposite polarity i.e. one producing horizontal focussing and vertical defocussing.

Thus a magnetic field region in which the gradient is of opposite sign to that already existing is required. The existing gradient is effective from the point of scatter of the protons to some metres beyond the exit port where the field has fallen to a negligible value. For practical reasons the second lens will have to be made much shorter than this and to achieve the desired result the gradient will have to be far greater than the mean value of the first lens.

As the beam rapidly diverges, the second lens must be placed as close as possible to the exit port, thus ensuring that all the protons passing through the port will be collected by a lens of reasonable aperture. This necessitates placing the lens in a region where the fringing field of the synchrotron magnet is intense and the possibility exists of redistributing a part of this fringing flux so as to produce a region of opposite gradient.

This system has been found very successful, as is described in the next section. As no external power is required to establish the desired field, the system has come to be known as a "Self Excited Quadrupole".

4. Experimental Arrangement

To obtain the desired field gradient, mild steel plates are placed as shown in figure 1. These plates are supported on a rigid stainless steel framework clamped to the body of the magnet, because, during a pulse, a force of several tons is exerted on the plates.

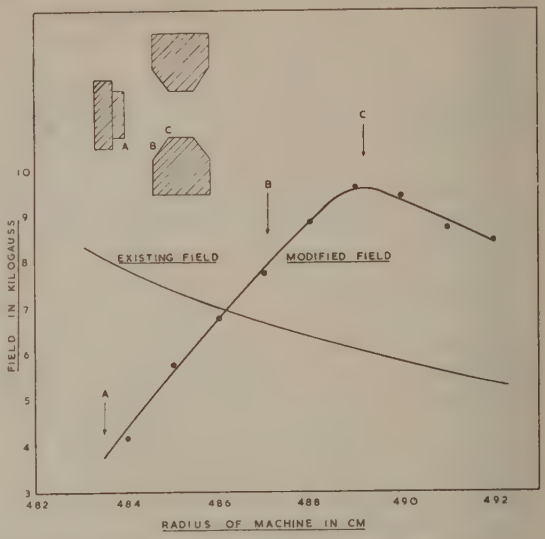

Fig. 2. Radial field dependence before and after modification.

By constructing the quadrupoles of $\frac{3}{8}''$ steel plates 20″ long, a very flexible arrangement is obtained and field gradients of various intensities may be had by simply transposing the plates. Hence various degrees of focussing are easily secured for the various beams to be used.

The field existing with and without the quadrupole in position is shown in fig. 2. The

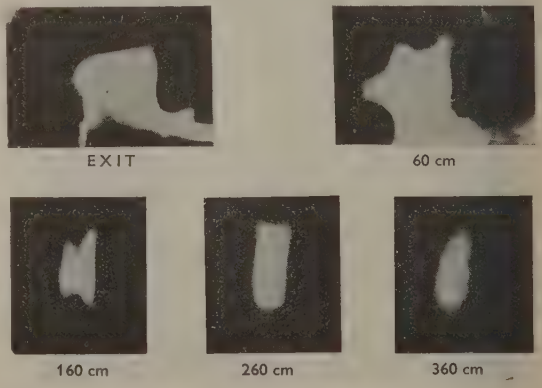

Fig. 3. Beam profile at various distances from the exit of quadrupole.

[2]) Courant, Livingston and Snyder, Phys. Rev. 88 (1952) 1190.

[3]) Sternheimer, Rev. Sci. Inst. 24 (1953) 573.

inset shows the relative positioning of the steel. It is evident that a linear of 1 100 gauss/cm is established over the region of interest. The correct steel arrangement to produce an almost parallel beam was determined by using X-ray film as a beam monitor. The beam profile found in this way at various distances from the exit port is shown in fig. 3.

In fig. 4 the horizontal and vertical extents of the beam are plotted as functions of distance

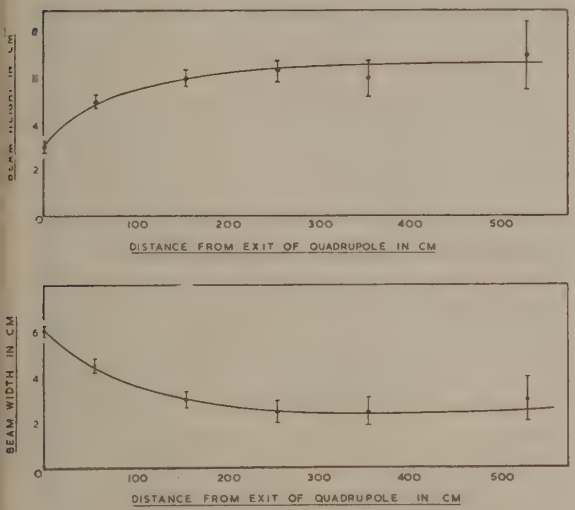

Fig. 4. Vertical and horizontal extent of beam as a function of distance from quadrupole.

from the exit of the quadrupole. From these curves it is evident that an almost parallel beam is obtainable. The intensity of the beam, determined with nuclear emulsions, is approximately 5×10^3 particles per sq. cm per pulse, over an area of about 20 sq. cm.

The energy spread in the beam may be determined from the size of the image and a knowledge of the mean trajectory. Calculation shows that an energy spread of $\pm$ 20 MeV is consistent with the observed results when considering a beam of mean energy 950 MeV.

In many experiments it is desired to undertake measurements over a range of energies. In a sychrotron this is simply effected by stopping the accelerating cycle at the desired instant. As the quadrupole is excited by the fringing field of the synchrotron magnet, its strength is automatically adjusted to the momentum of the scattered-out particles. Well focussed beams have been obtained at as low an energy as 350 MeV without altering the steel arrangement used to focus 950 MeV protons. However, to obtain optimum conditions, slight alterations may be necessary to allow for the saturation effects prevalent at peak field.

The initiation of this work followed discussions with Dr. J. L. Symonds and Professor R. R. Wilson of Harvard University. The co-operation of members of the synchrotron staff is gratefully acknowledged. The assistance of Mr. D. Hoare is also greatly appreciated.

NUCLEAR INSTRUMENTS 1 (1957) 354–358; NORTH-HOLLAND PUBLISHING CO. – AMSTERDAM

A PRINTED DISTRIBUTED AMPLIFIER

P. R. ORMAN, B. Sc., Ph. D.

Atomic Energy Research Establishment, Harwell, Berks

Received 10 August 1957

A distributed amplifier is described which has been designed for applications in the field of nuclear physics research. The gain of the amplifier is 20 db and its rise-time less than 2.5 mμs. Printed wiring techniques have been applied and the theoretical and practical advantages of this method of construction are considered.

1. Introduction

For nuclear physics experiments in which the timing of nuclear events is to be studied with the greatest possible resolution the scintillation counter has shown itself to be the most useful form of detector. This is because of the small variation in delay between the absorption of radiation in the scintillator and the appearance of an output signal. Nevertheless it is often found that the amplitude of the output signal is too small for the direct operation of the following electronic circuitry. In such circumstances the gain of the photomultiplier has to be augmented by the use of a wide-band amplifier and for a number of years distributed amplifiers have been used for this purpose.

The recent improvements in photomultipliers, particularly the reduction in transit-time variations, have however led to requirements for amplifiers with bandwidths in the region of 300 Mc/s, whose manufacture by conventional methods is both difficult and expensive. In the construction of the amplifier to be described here, the techniques of printed wiring have been applied, and whilst the basic reasons for this were mainly theoretical, the method has led to a very considerable simplification of construction and repeatability of results.

The principle of the distributed amplifier was first conceived by Percival[1]) in 1936 and since then the basic theory has been well developed and reported, notably by Ginzton *et al.*[2]) and by Basset and Kelly[3]). Ginzton *et al.* showed that the use of grid and anode lines consisting of m-derived sections with an m-value in the region of 1.3 gave a gain more nearly constant and a phase-frequency relation more nearly linear over the pass-band than was the case with the simpler constant-k section. Basset and Kelly studied designs for moderate bandwidths and showed how the characteristics could be further improved by the use of dissipative sections. Later workers, Sarma[4]) and Fidecaro and Wetherell[5]), have considered the use of grid and anode lines with different propagation speeds and have taken into account the effect of the self-capacitance of the inductances. In reference [5]) the presence of stray inductance in the shunt-arm is mentioned but its importance not enlarged upon. The effect of this inductance will be considered here, whilst the effects of grid conductance and self-capacitance of inductances will be ignored for the sake of clarity.

2. The Effect of Stray Inductance

In fig. 1 is shown the filter section (a) suggested by Ginzton *et al.* together with its equivalent (b). Component values are referred to those of the equivalent constant-k section in fig. 1c. As

[1]) W. S. Percival, British Patent Spec. No. 460, 562 (1936).

[2]) E. L. Ginzton, W. R. Hewlett, J. H. Jasberg and J. D. Noe, Proc. I.R.E. **36** (1948) 956–69.

[3]) H. G. Basset and L. C. Kelly, Proc. I.E.E. **101** Part III (1954) 5–14.

[4]) G. D. Sarma, Proc. I.E.E. **102** Part B (1955) 689–697.

[5]) G. Fidecaro and A. M. Wetherell, Nuovo Cimento **10** (1956) 359–370.

the cut-off frequency of the system is increased the inductance values required decrease and the effect of the stray shunt-arm inductance becomes more and more important. This inductance is denoted by L_s in fig. 2. In order to compensate for this it is necessary to increase the coupling between the two halves of the wound inductances. Referring to fig. 1b and fig. 2, we require that

$$M = \frac{m^2 - 1}{2m} L_0 + L_s \tag{1}$$

and

$$L = \frac{m^2 - 1}{2m} L_0 - L_s . \tag{2}$$

The coupling factor, K, is given by

$$K = \frac{M}{L} = \frac{(m^2 - 1)L_0 + 2mL_s}{(m^2 + 1)L_0 - 2mL_s} . \tag{3}$$

This may also be expressed as

$$K = \frac{m^2 - 1 + 8\pi^2 L_s C f_0^2}{m^2 + 1 - 8\pi^2 L_s C f_0^2} \tag{4}$$

where f_0 is the cut-off frequency, or

$$K = \frac{(m^2 - 1)R_0^2 C + 2m^2 L_s}{(m^2 + 1)R_0^2 C - 2m^2 L_s} \tag{5}$$

where $R_0^2 = L_0/C_0$, whence

$$f_0^2 = \frac{1}{8\pi^2 L_s C}\left[1 - m^2\left(\frac{1 - K}{1 + K}\right)\right] \tag{6}$$

and

$$R_0^2 = \frac{2m^2 L_s}{C\left\{1 - m^2\left(\frac{1 - K}{1 + K}\right)\right\}} . \tag{7}$$

Let us consider a practical case. Suppose that the valve selected is the E180F (CV3998) then the value of $2C$ in the grid line should be taken as 12 pF. If great care is taken to minimise lead lengths outside the valve then the stray positive inductance in the shunt-arm will be in the region of 0.01 μH. Using this value for L_s in expression (4) together with design values of 1.2 for m and 300 Mc/s for f_0 then we find that the value of K required is 0.44. A coupling factor of this magnitude is very difficult to achieve when the inductance is wound in the conventional way as a solenoid, but may be realised fairly readily if the inductance is made up of a few turns in the same plane. Herein lies the basic reason for adopting the technique of printed wiring, for this is the easiest method of forming the required inductances.

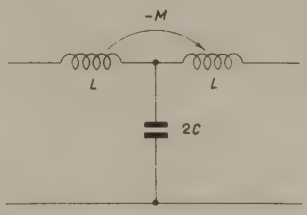

Fig. 1a

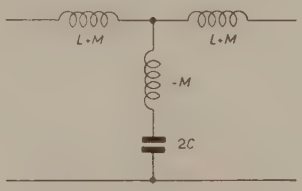

Fig. 1b

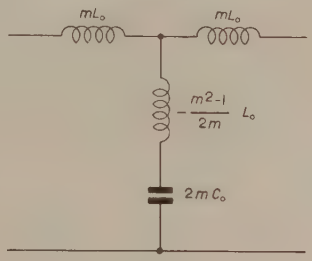

Fig. 1c

It is perhaps worth pointing out that as there is a practical limit to the amount of coupling

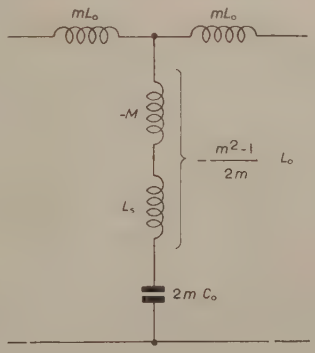

Fig. 2

that can be obtained, it follows from expression (6) that in a distributed amplifier designed with this type of section there is also a limit to the

bandwidth which depends on the lead inductances inside the valves. This is quite distinct from limits set by input conductance (itself due in part to cathode lead inductance) and electrode capacitances.

3. The Printed Amplifier

It will be seen from fig. 3 that the circuit of the amplifier is quite conventional. The valves are Mullard E180F pentodes (CV3998) having a mutual conductance of 16.5 mA/V at an anode current of 13 mA. These valves have rather a high input conductance, but appeared to be the most suitable type available.

In spite of the economy to be gained by making the output anode line impedance higher than that of the grid line, it was decided that the line impedances should be kept the same throughout. This facilitates the connection of two or more amplifiers in cascade when necessary, and the impedance of 100 ohm chosen as appropriate to the required bandwidth coincides happily with that of a convenient connecting cable (Telcon AS50M).

The arrangement of the valves into two groups of three and six was chosen in order to meet the output pulse requirements. The specification of a negative output pulse with a maximum amplitude of about 10 volts requires six valves in the output stage when the impedance is 100 ohm. The addition of a preceding stage containing three valves brings the total gain up to approximately 20 db. The maximum output pulse of 2 volts amplitude from the three valve stage when driven with a large negative input pulse does not produce a serious overload of the output stage.

It will be seen from fig. 3 that two forms of negative feedback are applied at low frequencies. In each stage there is feedback from the anodes

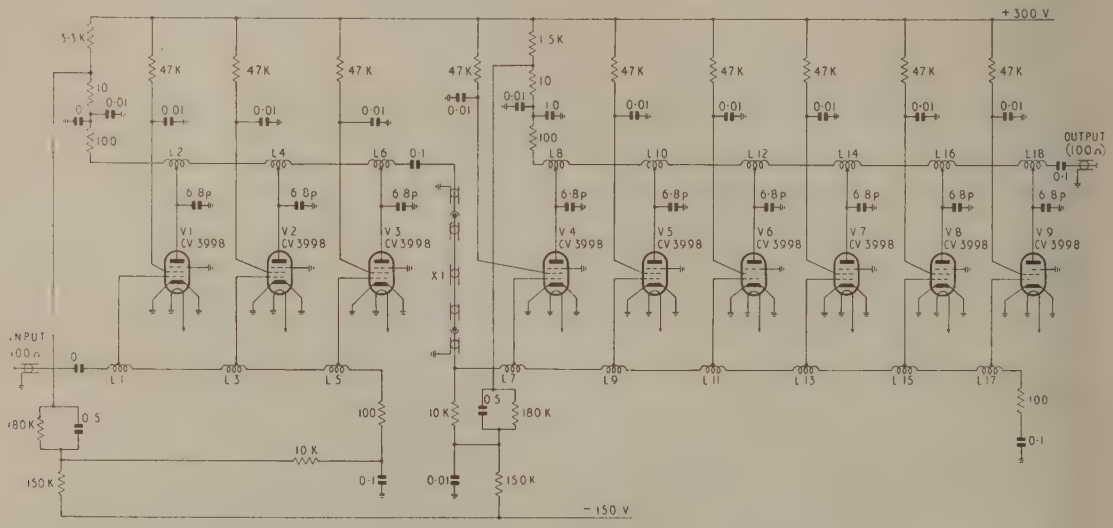

Fig. 3

The "printing" of the amplifier was done by the etched foil method described by Manfield[6, 7]). The inductances are formed out of copper foil of 0.0014 inch thickness bonded to a resin-bonded paper-based laminate. Whilst this insulating material is usually considered "lossy" at high frequencies, the impedance level in the amplifier is so low that the effect is of no importance. The inductances may be seen in the

to the grids. This stabilises the total mean anode current drawn by each stage. There is also feedback due to the large screen grid resistors. This equalises the current between valves and obviates the need for valve selection.

[6]) H. G. Manfield, Wireless World (Sept. 1955).

[7]) H. G. Manfield, R.R.E. Tech. Note No. 603 (Nov. 1956).

photograph fig. 4. They take the form of square "spirals" consisting of two turns. There is no theoretical significance in this shape, it merely simplifies the drawing work involved.

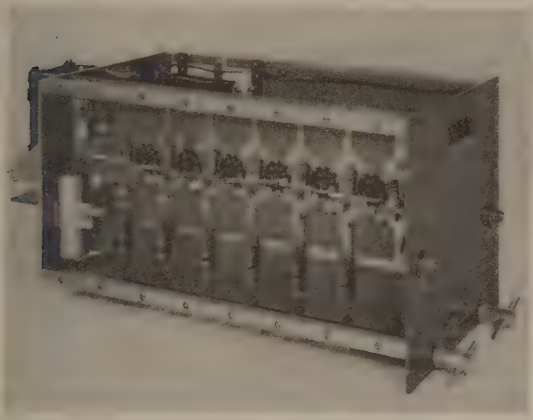

Fig. 4

4. Performance

The performance of a pulse amplifier is most usefully described in terms of its pulse response. This has been determined using input pulses of one millimicrosecond rise-time derived from the generator described by Orman and Wells[8]) and

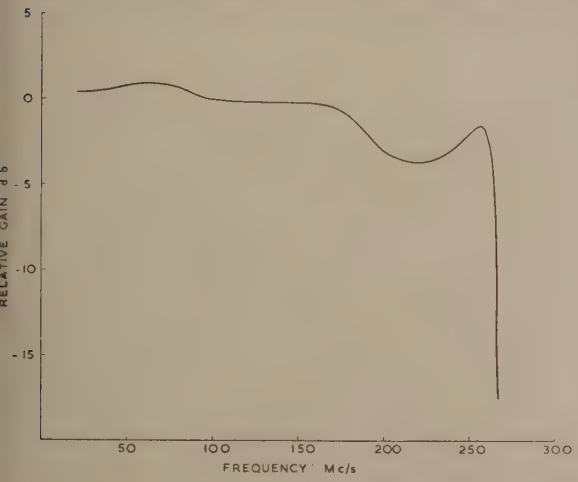

Fig. 5

a wide-band travelling-wave oscilloscope. The rise-time of the amplifier is determined in this way to be slightly less than 2.5 mμsec. There is an overshoot of 10% or less which is difficult to measure accurately owing to the low sensitivity of the oscilloscope. Whilst the basic coupling time-constants in the amplifier are 10 μsec, the response to pulses of long duration has been improved by making the time constant of the grid line decoupling nominally the same value. When the load for the output anode line consists of a resistance of 100 ohm in series with a capacitance of 0.1 μF there is no appreciable differentiation of a pulse of 10 μsec duration.

The gain-frequency characteristic of the amplifier at high frequencies is shown in fig. 5. The phase-frequency characteristics of the grid and anode lines separately has been determined by the method described in ref.[5]) and the results appear in fig. 6.

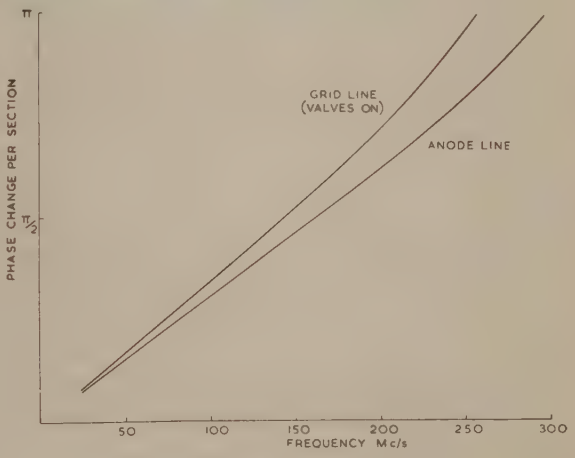

Fig. 6

The gain at mains hum frequencies is very small, and the total hum at the output of the amplifier is in the region of 10 mV.

5. Lay-out and Components

As is to be expected, the lay-out of the circuit is quite critical and lead lengths have to be reduced to a minimum in the high frequency part of the circuit. Considerations of lead-length influenced even the choice of valveholders. The type used is of rather old design, but has the

[8]) P. R. Orman and F. H. Wells, Nuclear Instruments **1** (1957) 183–185.

useful feature of making contact with the pins of the valve quite close to the glass bulb, and by this means the lead-lengths are significantly reduced.

The coupling and decoupling capacitors of 0.1 μF capacitance employ high permittivity ceramic dielectric and are of recent design. They are used on account of their very low self-inductance. The screen grid decoupling capacitors were also chosen for their low self-inductance. This is particularly important since the presence of an inductive load in the screen grid circuit reflects a negative resistance at the valve input, and may lead to parasitic oscillation.

6. Conclusion

Printed wiring techniques have been successfully applied in the construction of the amplifier described and show great promise for the whole field of millimicrosecond electronics, where performance depends quite critically on wiring "strays". This method of construction ensures that the strays present in the designer's prototype are faithfully reproduced in later models.

Although the method of etched-foil printed wiring has its greatest value in the mass production of equipment, experience has shown that by the use of quite simple home-made apparatus the production of laboratory quantities of equipment is neither difficult nor exhorbitantly expensive.

Acknowledgement

The author's thanks are due to the Director of the Atomic Energy Research Establishment, Harwell, for permission to publish this paper, to Mr. H. G. Manfield of the Royal Radar Establishment, Malvern, for advice on printing methods, to Mr. F. H. Wells for his valuable advice and encouragement, and to Mr. J. R. Brooks for his practical assistance.

AUTHOR INDEX

Adams, J. B., The CERN symposium 1956 (I) . . . 2
Akpinar, S., The output distorsion of a differential interval analyzer of universal design 200
Almén, O. and K. O. Nielsen, Systematic investigation of a magnetic ion source for an electromagnetic isotope separator 302
Åström, B., Scintillation spectrometer with constant relative channel width 143
Atkinson, J. R., W. McFarlane, J. M. Reid and P. Swinbank, A γ-ray collimator and expansion chamber for use with the 340 MeV electron synchrotron 152

Bäckström, G., A device for the precision measurement of an inhomogenous magnetic field . . 253
Ball, W. P., R. Booth and M. MacGregor, Temperature coefficients of scintillating systems . . 71
Batty, C. J., The loading of nuclear emulsions with water 138
Bergkvist, K. E., *see* Stockendal
Berglund, S., R. Nilsson, P. Ohlin, K. Siegbahn, T. Sundström and S. Svennerstedt, Fusion experiments in deuterium plasma 233
Bludman, S. A., *see* Judd
Bolzinger, T., *see* Bronca
Booth, N. E. and G. W. Hutchinson, Fine time-structure of beams from the Birmingham proton synchrotron 80
Booth, N. E. and B. Ledley, Efficient detector for high energy neutrons 345
Booth, R., *see* Ball
Bowkett, N. F., *see* Treacy
Breitenberger, E., Diverging electrostatic lenses in accelerators 55
Bronca, G., H. Bruck, J. Hamelin, G. Neyret et T. Bolzinger, Le test des blocs de l'électro-aimant du synchrotron de Saclay 123
Brown, D. C. and B. P. Faraday, A transistorized radiation monitor 133
Bruck, H., *see* Bronca

Calame, G., P. F. Cooper, Jr., S. Engelsberg, G. L. Gerstein, A. M. Koehler, A. Kuckes, J. W. Meadows, K. Strauch and R. Wilson, Some features of regenerative deflection and their application to the Harvard synchrocyclotron 169
Cohen, S. and A. V. Crewe, Regenerative action in high energy accelerators 31
Cooper, P. F., *see* Calame
Cornides, I., J. Roósz and A. Siegler, Two lithium ion sources for accelerators 94
Crewe, A. V., *see* Cohen
Curran, S. C., *see* Drever

Drever, R. W. P., A. Moljk and S. C. Curran, A proportional counter system with small wall effect 41

Egelstaff, P. A., Glass scintillators for prompt detection of intermediate energy neutrons . . . 197
Engelsberg, S., *see* Calame

Faraday, B. P., *see* Brown
Favre, R. L., Démultiplicateurs électroniques d'impulsions (1ère Partie) 113
Favre, R. L., Démultiplicateurs électroniques d'impulsions (2ème Partie) 201
Firk, F. W. K., *see* Rae

Gåsström, R. V., A very fast pulse-height analyser with independent uptake, sorting and storage of information 75
Gerholm, T. R., T. Lindqvist and H. de Waard, Multi coincidence goniometer for angular correlation measurements 107
Gerstein, G. L., *see* Calame
Ghigo, G. and I. F. Quercia, Field stabilization in a D.C.–A.C. excited magnet of a synchrotron . . . 57
Goldsack, S. J., Two target operation of a proton-synchrotron 90

Hamelin, J., *see* Bronca
Horlitz, G. und W. Paul, Die Blasendichte in einer Blasenkammer unter verschiedenen Betriebsbedingungen 340
Hughes, D. J., *see* Seidl
Hutchinson, G. W., *see* Booth, N. E.
Hutchinson, G. W., *see* White

Jamnik, D., Energy control of a 31 MeV betatron 324
Jensen, B. S., Note on the preparation of anhydrous rare-earth chlorides for the electromagnetic isotope separator 323
Johansson, B., Coincidence arrangement with high time resolution used together with a 100-channel pulse-height analyzer 274
Judd, D. L. and S. A. Bludman, Aberrations and fringing effects in a 180° double focussing magnetic spectrometer 46

Kjellman, J., *see* Malmfors
Koehler, A. M., *see* Calame
Kritzinger, C. A. J., An apparatus for measuring the speed of pneumatically transported grains by means of radioactivity 66
Kuckes, A., *see* Calame

Le Couteur, K. J., The vertical motion of particles through the regenerative beam extractor of a synchrocyclotron 343

Ledley, B., *see* Booth, N. E.
Lindqvist, T., *see* Gerholm
Lundby, A., The CERN symposium 1956 (III) . . 17

MacGregor, M., *see* Ball
Macklin, R. L., Graphite sphere neutron detector . 335
Macq, P. C. , *see* Vervier
Malmfors, K. G., J. Kjellman and A. Nilsson, The time-of-flight technique applied to fast neutrons 186
Malmfors, K. G., On the possibility of applying trochoidal orbits in beta-spectroscopy 251
McFarlane, W., *see* Atkinson
Meadows, J. W., *see* Calame
Meyer, M. A., Pulse-lengthener circuits 62
Moljk, A., *see* Drever

Neyret, G., *see* Bronca
Nielsen, K. O. and O. Skilbreid, Continuous scanning in two directions of the ion beam in an electromagnetic isotope separator 159
Nielsen, K. O., The development of magnetic ion sources for an electromagnetic isotope separator 289
Nielsen, K. O., *see* Almén
Nilsson, A., *see* Malmfors
Nilsson, R., *see* Berglund

Ohlin, P., *see* Berglund
Orman, P. R. and F. H. Wells, A millimicrosecond pulse-shaping circuit 183
Orman, P. R., A printed distributed amplifier . . . 354

Palevsky, H., *see* Seidl
Paul, W., *see* Horlitz

Quercia, I. F., *see* Ghigo

Rae, E. R. and F. W. K. Firk, An application of magnetic tape recording to neutron time-of-flight spectroscopy 227
Reid, J. M., *see* Atkinson
Roósz, J., *see* Cornides

Schneider, H., An A.G. channel with four quadrupole magnets 268
Seidl, F. G. R., H. Palevsky, D. J. Hughes and R. L. Zimmerman, Modification of the Brookhaven fast chopper 92
Siegbahn, K., Editor's notice 1
Siegbahn, K., Editor's note 233
Siegbahn, K., *see* Berglund
Siegler, A, *see* Cornides
Sikkema, C. P., Elimination of end effects in proportional counters 148
Skilbreid, O., *see* Nielsen
Slätis, H., On diffusion cloud chambers (survey article) 213
Spaa, J. H., *see* Van Dorsten
Stockendal, R. and K. E. Bergkvist, Evaporation device for beta-spectrometer samples 53
Strauch, K., *see* Calame
Sundström, T., *see* Berglund
Svennerstedt, S., *see* Berglund
Swinbank, P., *see* Atkinson

Tove, Per-Arne, Electronic time analyzer applied to the measurement of the half-lives of metastable nuclear states. 95
Treacy, P. B. and N. F. Bowkett, A target box for bombardment of CF_4 in gaseous or solid form 86

Van Dorsten, A. C. and J. H. Spaa, A high output D–D neutron generator for biological research 259
Van der Raay, H. B., Focussing of the synchroton scattered-out beam 351
Varshni, Y. P., A new particle accelerator 280
Vervier, J. F. et P. C. Macq, Réduction des dispersions dans les détecteurs à scintillation 282
Vladimirsky, K. V., Radiation instability in nuclear magnetic resonance experiments 329
Von Dardel, G. F., The CERN symposium 1956 (II) 10

Waard, H. de, *see* Gerholm 107
Walen, R. J., Transformation d'une focalisation de premier ordre en focalisation de deuxème ordre en spectrographie magnétique à champ homogène 242
Wells, F. H., *see* Orman
White, D. H. and G. W. Hutchinson, A fast coincidence circuit 331
Wilson, R. R., Precision quantameter for high energy X-rays 101
Wilson, R., *see* Calame

Zimmerman, R. L., *see* Seidl

BOOK REVIEWS

Compton, A. H., Atomic Quest (G. Ekspong) . . . 56
Gorter, C. J., editor, Progress in Low Temperature Physics vol. II (J. O. Linde) 168
Reports on Progress in Physics, volume XIX. (T. R. Gerholm) 56
The Physics of Nuclear Reactors (I. Carlvik) 112

SUBJECT INDEX

Accelerators

Regenerative action in high energy accelerators, S. Cohen and A. V. Crewe . . . 31
Diverging electrostatic lenses in accelerators, E. Breitenberger . . . 55
Field stabilization in a D.C. A.C. excited magnet of a synchrotron, G. Ghigo and L. F. Quercia . . . 57
Fine time-structure of beams from the Birmingham proton synchrotron, N. E. Booth and G. W. Hutchinson . . . 80
Two target operation of a proton-synchrotron, S. J. Goldsack . . . 90
Two lithium ion sources for accelerators, I. Cornides, J. Roósz and A. Siegler . . . 94
Le test des blocs de l'électro-aimant du synchrotron de Saclay, G. Bronca, H. Bruck, J. Hamelin, G. Neyret et T. Bolzinger . . . 123
Some features of regenerative deflection and their application to the Harvard synchrocyclotron, G. Calame, P. F. Cooper, Jr., S. Engelsberg, G. L. Gerstein, A. M. Koehler, A. Kuckes, J. W. Meadows, K. Strauch and R. Wilson . . . 169
An A.G. channel with four quadrupole magnets, H. Schneider . . . 268
A new particle accelerator, Y. P. Varshni . . . 280
Energy control of a 31 MeV betatron, D. Jamnik . . . 324
The vertical motion of particles through the regenerative beam extractor of a synchrocyclotron, K. J. Le Couteur 343
Focussing of the synchroton scattered-out beam, H. B. van der Raay . . . 351

Automation

An apparatus for measuring the speed of pneumatically transported grains by means of radioactivity, C. A. J. Kritzinger . . . 66

Counters, Chambers and Detectors

A. proportional counter system with small wall effect, R. W. P. Drever, A. Moljk and S. C. Curran . . . 41
Temperature coefficients of scintillating systems, W. P. Ball, R. Booth and M. MacGregor . . . 71
A transistorized radiation monitor, D. C. Brown and B. P. Faraday . . . 133
The loading of nuclear emulsions with water, C. J. Batty . . . 138
Elimination of end effects in proportional counters, C. P. Sikkema . . . 148
A γ-ray collimator and expansion chamber for use with the 340 MeV electron synchrotron, J. R. Atkinson, W. McFarlane, J. M. Reid and P. Swinbank . . . 152
Glass scintillators for prompt detection of intermediate energy neutrons, P. A. Egelstaff . . . 197
On diffusion cloud chambers (survey article), H. Slätis . . . 213
Réduction des dispersions dans les détecteurs à scintillation, J. F. Vervier et P. C. Macq . . . 282
Graphite sphere neutron detector, R. L. Macklin . . . 335
Die Blasendichte in einer Blasenkammer unter verschiedenen Betriebsbedingungen, G. Horlitz und W. Paul . . . 340
Efficient detector for high energy neutrons, N. E. Booth and B. Ledley . . . 345

Electronic Equipment

Pulse-lengthener circuits, M. A. Meyer . . . 62
A very fast pulse-height analyser with independent uptake, sorting and storage of information, R. V. Gåsström 75
Electronic time analyzer applied to the measurement of the half-lives of metastable nuclear states, Per-Arne Tove 95
Démultiplicateurs électroniques d'impulsions (1ère partie), R. L. Favre . . . 113
A millimicrosecond pulse-shaping circuit, P. R. Orman and F. H. Wells . . . 183
The output distorsion of a differential interval analyzer of universal design, S. Akpinar . . . 200

Démultiplicateurs électroniques d'impulsions (2ème partie), R. L. Favre 201
Coincidence arrangement with high time resolution used together with a 100-channel pulse-height analyzer, B. Johansson 274
A fast coincidence circuit, D. H. White and G. W. Hutchinson 331
A printed distributed amplifier, P. R. Orman 354

Fusion

Fusion experiments in deuterium plasma, S. Berglund, R. Nilsson, P. Ohlin, K. Siegbahn, T. Sundström and S. Svennerstedt 233

Instruments for Nuclear Spectroscopy

Evaporation device for beta-spectrometer samples, R. Stockendal and K. E. Bergkvist 53
A target box for bombardment of CF_4 in gaseous or solid form, P. B. Treacy and N. F. Bowkett 86
Modification of the Brookhaven fast chopper, F. G. P. Seidl, H. Palevsky, D. J. Hughes and R. L. Zimmerman . 92
Precision quantameter for high energy X-rays, R. R. Wilson 101
Multi coincidence goniometer for angular correlation measurements, T. R. Gerholm, T. Lindqvist and H. de Waard 107
The time-of-flight technique applied to fast neutrons, K. G. Malmfors, J. Kjellman and A. Nilsson 186
An application of magnetic tape recording to neutron time-of-flight spectroscopy, E. R. Rae and F. W. K. Firk . 227
Radiation instability in nuclear magnetic resonance experiments, K. V. Vladimirsky 329

Isotope Separators

Continuous scanning in two directions of the ion beam in an electromagnetic isotope separator, K. O. Nielsen and O. Skilbreid 159
The development of magnetic ion sources for an electromagnetic isotope separator, K. O. Nielsen 289
Systematic investigation of a magnetic ion source for an electromagnetic isotope separator, O. Almén and K. O. Nielsen 302
Note on the preparation of anhydrous rare-earth chlorides for the electromagnetic isotope separator, B. S. Jensen 323

Miscellaneous

A high output D–D neutron generator for biological research, A. C. van Dorsten and J. H. Spaa 259

News Items

Editor's notice 1
The CERN symposium (I) J. B. Adams 2
The CERN symposium 1956 (II), G. F. von Dardel 10
The CERN symposium 1956 (III), A. Lundby 17
Proceedings of the CERN symposium 1956 21
International conference on nuclear structure (Rehovoth, 1957) 166
Conference on nuclear structure (Pittsburgh, 1957) 167
Extra-atmospheric cosmic radiation research (Baltimore, 1957) 232
Mesons and recently discovered particles (Padova, 1957) 232
Editor's note 233

Spectrometers (*see also* Instruments for Nuclear Spectroscopy)

Aberrations and fringing effects in a 180° double focussing magnetic spectrometer, D. L. Judd and S. A. Bludman 46
Scintillation spectrometer with constant relative channel width, B. Åström 143
Transformation d'une focalisation de premier ordre en focalisation de deuxième ordre en spectrographie magnétique à champ homogène, R. J. Walen 242
On the possibility of applying trochoidal orbits in beta-spectroscopy, K. G. Malmfors 251
A device for the precision measurement of an inhomogenous magnetic field, G. Bäckström 253